Electronic Properties of Doped Mott Insulators and High Temperature Superconductors

by

Tiago Castro Ribeiro

Licenciado in Technological Physics Engineering
Technical University of Lisbon, 1999

Submitted to the Department of Physics
in partial fulfillment of the requirements for the degree of

Doctor of Philosophy

at the

MASSACHUSETTS INSTITUTE OF TECHNOLOGY
[September 2005]
August 2005

Author .....
Department of Physics
August 24, 2005

Certified by .....
Xiao-Gang Wen
Cecil and Ida Green Professor of Physics
Thesis Supervisor

Accepted by .....
Thomas J. Greytak
Professor, Associate Department Head for Education

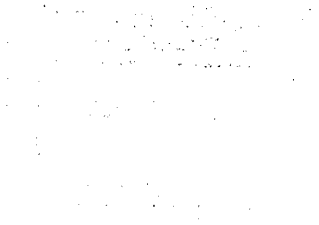

Electronic Properties of Doped Mott Insulators and High Temperature Superconductors

by

Tiago Castro Ribeiro

Submitted to the Department of Physics
on August 24, 2005, in partial fulfillment of the
requirements for the degree of
Doctor of Philosophy

Abstract

High-temperature superconducting cuprates, which are the quintessential example of a strongly correlated system and the most extensively studied materials after semiconductors, spurred the development in the fields of material science and experimental and theoretical physics. As first noted by Anderson, these materials are doped Mott insulators and the novel phenomenology emerges in the regime intermediate to the Néel state and the Fermi liquid metal where electrons evolve from being local moments to itinerant entities. This thesis attempts to describe the evolution of the electronic properties between the above two limits as of interest to high-temperature superconductors. We use the $tt't''J$ model to describe doped Mott insulators and resort to numerical methods and to both well known and new approximate analytical techniques to deal with the absence of on-site double electron occupancy.

We first address the problem of a single hole in the $tt't''J$ model in terms of the exact diagonalization and the self-consistent Born approximation methods. We show spins dress the doped hole in two distinct ways, namely with a staggered moment and a liquid spin configurations. The resulting two-band picture captures the momentum space anisotropy consistent with experimental observations in underdoped cuprates.

Next we use the $SU(2)$ slave boson mean-field theory of the $tt'J$ model. The role of next-nearest-neighbor hopping t' on the phase diagram is studied. We find that when $t' > 0.5J$ a Z_2 state with true spin-charge separation exists, which can be a candidate for an eventual pseudogap phase in electron doped materials.

We then derive a new formulation of the $tt't''J$ model in terms of holes instead of electrons and introduce a mean-field description of doped Mott insulators that provides an effective two-fluid model of vacancies which captures the effect of staggered moment and d-wave singlet bond short-range spin correlations on the hole dynamics. It leads to a mean field phase diagram consistent with that of hole and electron doped cuprates. Moreover, it provides a framework to describe the observed evolution of the electron spectral function from the undoped insulator to the overdoped Fermi metal, as we conclude from extensively comparing the mean-field results to non-trivial angle-resolved photoemission spectroscopy and tunneling conductance data.

Thesis Supervisor: Xiao-Gang Wen
Title: Cecil and Ida Green Professor of Physics

Acknowledgments

Enthusiasm is the inspiration of everything great. Without it no man is to be feared, and with it none despised.

Christian Nestell Bovee

Recently, at a conference in Tobago, I engaged in a conversation with a fellow who, once I mentioned my provenience, told me that at his Institute in Argentina every incoming student is instructed to read the introduction of Xiao-Gang Wen's book. His words were: "He is so enthusiastic about physics and nature". My experience with Xiao-Gang far surpasses the mere reading of his book – I was privileged enough to be his student for the past five years. A smile drew in my face and I replied: "He is *contagiously* enthusiastic". Needless to mention then, it is was always refreshing and engaging to meet with Xiao-Gang, whose kindness and unmatched humility assured I was always welcome to his office. Xiao-Gang's genius and physical intuition all too often struck me as insightful comments surely originating from his very unique big picture of "things". Mostly appreciated were his constant respect for my personal learning/discovery process, his continuous support that encouraged me to explore my ideas and his timely advice that kept me on the right track.

I was also fortunate to receive the teachings from many excellent faculty not only at MIT, but also at Harvard University and Boston University: I will always remember the solid education on the physics of solids provided by John Joannopoulos; Mehran Kardar's clear exposition of statistical physics will always be a reference; Sidney Coleman's lectures on field theory and Daniel Fisher's course on scaling and dynamics will always remain inspiring. In addition, I believe I shall stand out as one of the few condensed matter physicists (probably alongside other CMT students) whose main reference to many-body physics is not one of the classics, namely AGD, Fetter & Walecka or Mahan, but rather Xiao-Gang's 8.513 and Patrick Lee's 8.514 lecture notes, which convey profound insights that have shaped my thinking on the physics of condensed matter systems. I also enormously benefited from cohabiting the CMT corridor with Patrick, whose wisdom is shared not only in private discussions but also during lunch time conversations (which I occasionally join) and in his observations at various seminars. I should equally mention Senthil Todadri's good spirited laughs and several conversations we had on various physics and non-physics related topics, which make me look forward to meeting him at conferences in India and elsewhere. Moreover, I would like to express my gratefulness to Patrick Lee and Frank Wilczek for agreeing to serve on my thesis committee and to kindly acknowledge the financial support from *Fundação para a Ciência e Tecnologia* (grant PRAXIS XXI BD-19612/99) and from *Fundação Calouste Gulbenkian* (grant No 58119).

There exist a few great people, who I feel honored to join as a Wen's disciple, that I have met to a bigger or lesser extent. These include Joel Moore who I hope to get the chance to interact further with once I move to sunny California, more precisely to Berkeley. Interestingly enough, I crossed Anna Lopatnikova's path outside of physics as we were colleagues in an introductory finance course at Sloan. During the last three years Bas Overbosch, Michael Levin and Ying Ran have been part of my day-

to-day life as we meet around the offices and share our life experiences along with some physical expertise. Michael and Ying were also my trip mates in last year's visit to China, whose Xiao-Gang's and the Center for Advanced Studies at Tsingua University's support I sincerely acknowledge. The stay in China was a uniquely enriching experience at many levels, scientific and non-scientific, which I shall never forget. The chance to stay in Beijing in a non-touristy setting favored the cultural exchange and I will remember both the dining experiences Michael and I shared with no ability to communicate with the locals as well as all the fantastic meals Ying chose for us. In fact, the experience in China greatly benefited from Ying's skill and will to guide us through various places and locations and I am extremely thankful for that. Ying, whom I have been lucky to share the office with, sits at the desk of yet another Wen's disciple, namely Walter Rantner whose mentorship in my early days in the high-T_c field was most valuable. Walter's presence in my life went far beyond the sphere of our office though. He is a friend whose insights in various matters led to vivid discussions and a lot of learning, not to mention how much I miss our daily trip for lunch at Whitehead in the good company of our other office mate, Alexander Seidel. I am just so glad that once at Berkeley I will enjoy Alex's daily company again.

The many students, post-docs and visitors at CMT further provide the right ambiance to conduct stimulating research. I will certainly remember the breaks where I had the chance to exchange views with other students, such as Adam Durst, Dima Novikov, Kevin Beach, Daniel Greenbaum, Michael Hinczewski, Casey Huang, Roman Barankov, Dima Abanin, Pouyan Ghaemi, Saeed Saremi, David Chan, Peter Bermel, Daniel Bozi and Cody Nave, to whom I also acknowledge some of his unpublished variational Monte Carlo data presented in this thesis. I am equally grateful for the interaction with numerous post-docs and visitors like Misha Fogler, Ilya Gruzberg, Yoshifumi Morita, Carsten Honerkamp, Ashvin Vishwanath, Olexei Motrunich, Vincent Liu, Bernd Braunecker, Walter Hofstetter and Su-Peng Kuo. In particular, I enjoyed the experience of organizing last year's Informal Condensed Matter Seminar Series together with Peter Virnau and Sung-Sik Lee. I am also glad to have met José Carmelo who is visiting from Portugal – the daily encounters in our offices or at lunch have led to a variety of conversations that ranged from the particulars of our research to the realm of our lives.

I would like to take this opportunity to thank all professors in Portugal who contributed to my physics education. I particularly remember João Pedro Conde who lectured my first course in solid state physics and who is to blame for my choice to embark in related research, which eventually led me to meet José Luís Martins who was the most inspiring of professors. More than just an undergraduate supervisor, he was a mentor and his advice and support instrumental on my application to MIT.

The PhD. involves a considerable personal and emotional commitment and cannot be dissociated from the other spheres of one's life. The last six years were a great experience I particularly owe to the fantastic people I have met and who made Cambridge feel like home. These include my room mates Ricardo Schiappa (whose support in the early days is most acknowledged), Rodrigo Rodrigues (who survived after sharing an apartment with me for four years), Pedro Ferreira (a good mate at

late hours), Kostas Magoutis (whose kindness will be remembered), Daniele Portolan (whose strong opinions led to many enthusiastic discussions), Courtney Stewart (a feminine touch is always welcome) and Mirko Ristivojevic (what a colorful character). I have to mention Mirko's wife, Nataša, whose great spirit and genius, strong personality and wonderful cooking I was so lucky to have come across. Wolfgang Bergmeier, Ellen O'Shaughnessy, Florian Altmann, Birgit Schoeberl and Lilla Zollei are much more than just regular companions for a beer at the Miracle (or elsewhere) and are responsible for many vivid memories which include well documented ski trips and fun parties. I am also glad to have become close friends with Sarah Krawczyk, a refreshing young soul.

I am especially grateful for the time spent with quite a few fine portuguese individuals, some of them since my very first minute in the US. I thank Francisco Veloso, an opponent in the squash courts, for making his apartment available to me when needed and for introducing me to Maria and Sr. Chico, the friendly owners of Portugalia (the portuguese restaurant of choice). Inês Sousa is another good friend, as is Maria João Tavares who initiated me in the "heated-room" Yoga practice. The interaction with Nuno Martins during our two year long incursion at Sloan was rewarding at both personal and intellectual levels. The experience as a member of the Portuguese Student Association's board of directors was also a lot of fun. In this context, I thank Marcus Dahlem for organizing the euro cup viewing last year, whose sessions invariably ended with big celebrations of Portugal's many victories and few defeats. In these events I met Rita Teodoro and Miguel Remondes whose kindness, most friendly attitude and lots of positive energy played a major role in bringing together new and old friends which I feel are my local family. These include Cátia Fonseca, Sara Maia, Xana Frias and Zé Antão. This list would not be complete without Francisca Leite. Kika has been a fellow in arms and a true friend over the past few years, with whom I sure hope to keep on sharing thoughts, interests, experiences and, whenever possible, the pleasure of a vodka martini (or alike).

I sincerely acknowledge all the members of "bacalhau" (David Duarte, Filipe Fonseca, Tiago Oleastro, Rodrigo Oliveira, Rui Prieto, Luís Afonso Ribeiro and Teresa Santos), whose casual, funny and informative emails were a valid source of distraction and a great way to stay in touch.

I owe a special word to Catarina who shared with me the emotional strain implied by embarking in such a long and so far away trip. Your endless friendship is immensely valued. Finally let me thank my sister and my parents for all the care, support, encouragement and love, always and ever. You are my greatest gift.

Para os meus Pais

Contents

1 Introduction **15**
- 1.1 Motivation . . . 15
- 1.2 Doped Mott insulators . . . 18
- 1.3 Outline of the thesis . . . 19

2 Momentum space anisotropy in doped Mott insulators **23**
- 2.1 Introduction . . . 23
- 2.2 One-hole states . . . 24
- 2.3 Properties of Q and U states . . . 28
- 2.4 Momentum space anisotropy . . . 31
- 2.5 Conclusions . . . 32

3 $SU(2)$ slave boson mean-field theory – possible Z_2 phase and spin-charge separation in electron doped cuprates **35**
- 3.1 Introduction . . . 35
- 3.2 Slave boson mean-field theory of the $tt'J$ model . . . 37
  - 3.2.1 Slave boson mean-field theory of the Heisenberg Hamiltonian . 37
  - 3.2.2 $SU(2)$ mean-field theory of the $tt'J$ model . . . 39
- 3.3 Mean-field phase diagrams . . . 40
- 3.4 Spin-charge separation: the role of t' . . . 44
- 3.5 Application to electron doped cuprates . . . 46
- 3.6 Conclusions . . . 46

4 New formulation of the $tt't''J$ model and the "doped carrier" mean-field theory of cuprates **49**
- 4.1 Introduction . . . 49
- 4.2 Doped carrier formulation of the $tt't''J$ model . . . 51
  - 4.2.1 Enlarged Hilbert space . . . 51
  - 4.2.2 Heisenberg term . . . 52
  - 4.2.3 Hopping term . . . 52
- 4.3 Doped carrier mean-field theory of the $tt't''J$ model . . . 54
  - 4.3.1 Heisenberg term . . . 54
  - 4.3.2 Hopping term . . . 54
  - 4.3.3 Mean-field Hamiltonian . . . 57
  - 4.3.4 Renormalized hopping parameters . . . 58

4.4 Doped carrier mean-field phase diagram 60
4.5 Conclusions 65
4.6 Appendix A: Hopping term in enlarged Hilbert space 66
4.7 Appendix B: Doped carrier mean-field self-consistent equations 69
4.8 Appendix C: Antiferromagnetic mean-field self-consitent equations . . 70

5 Electron spectral function of superconducting doped Mott insulators 73
5.1 Introduction 73
5.2 ARPES and the cuprates 75
5.2.1 Undoped materials 75
5.2.2 Hole doped materials 77
5.2.3 Electron doped materials 80
5.3 Electron spectral function of superconductors 81
5.3.1 BCS mean-field spectral function 81
5.3.2 Slave boson mean-field spectral function 82
5.4 Doped carrier mean-field electron spectral function 83
5.4.1 Mean-field electron operator 84
5.4.2 Mean-field electron spectral function 85
5.4.3 Hole doped case 86
5.4.4 Electron doped case 96
5.5 Conclusions 100
5.6 Appendix: Electron operator 102
5.6.1 Hole doped case 102
5.6.2 Electron doped case 103

6 Tunneling spectra of layered strongly correlated d-wave superconductors 105
6.1 Introduction 105
6.2 Tunneling spectra of BCS d-wave superconductors 106
6.3 Dispersion renormalization 109
6.4 Tunneling spectra of strongly correlated d-wave SC 111
6.5 Conclusions 113

7 Concluding remarks 115
7.1 Role of short-range correlations 115
7.2 Two-band description of local energetics 118
7.3 Interplay between dSC and AF correlations 120
7.4 Renormalization of t' and t'' 122
7.5 Comparison to slave boson approach 123
7.6 Probing local correlations 126

List of Figures

2-1 Average value of the staggered magnetization around the vacancy for different states. 28
2-2 Momentum space distribution and energy dispersion relations of Q and U states. 30

3-1 (t', x) slave boson mean-field phase diagram. 41
3-2 (x, T) slave boson mean-field phase diagram. 43

4-1 (x, T) "doped carrier" mean-field phase diagram. 61

5-1 Experimental ARPES data *I*. 76
5-2 Experimental ARPES data *II*. 78
5-3 "Doped carrier" mean-field energy dispersion and electron spectral function along $(0,0) - (\pi,\pi) - (0,\pi) - (0,0)$ in the hole doped regime. 87
5-4 "Doped carrier" mean-field electron spectral function along the nodal direction in the hole doped regime. 88
5-5 Doping evolution of different quantities extracted from the "doped carrier" mean-field electron spectral function in the hole doped regime. . 89
5-6 "Doped electron" mean field electron spectral weight distribution in momentum space for doped hole densities $x = 0.05$, $x = 0.12$ and $x = 0.20$. 90
5-7 "Doped electron" mean field electron spectral function results for doped hole densities $x = 0.05$, $x = 0.12$ and $x = 0.20$. 91
5-8 "Doped carrier" mean-field energy dispersion and electron spectral function along $(0,0) - (\pi,\pi) - (0,\pi) - (0,0)$ in the electron doped regime. 96
5-9 "Doped electron" mean field electron spectral function results for doped electron densities $x = 0.05$ and $x = 0.15$. 98

6-1 Tunneling differential conductance for BCS superconductors. 107
6-2 Comparison between phenomenological and "doped carrier" mean-field theory energy dispersions along $(0,0) - (\pi,\pi) - (0,\pi) - (0,0)$. 110
6-3 "Doped carrier" mean-field tunneling conductance. 112

7-1 Schematic pictures for the introduction and evolution of a hole in two different spin backgrounds. 117
7-2 Schematic representation of the dopon and the holon. 118

7-3 Schematic band diagram for a hole introduced into a spin system with antiferromagnetic spin correlations. 119

List of Tables

2.1 Evidence for decomposing the $tt't''J$ model one-hole state into Q and U states as described in the main text. 26
2.2 Integrated momentum space distribution of $\tilde{\mathrm{U}}$ states. 30
2.3 ΔE^{Q}, ΔE^{U}, ΔE^{ψ} and $W^{Q}_{\boldsymbol{k}}$ with $\boldsymbol{k} = \boldsymbol{k'} \equiv (\pi, 0)$ and $\boldsymbol{k} = \boldsymbol{k''} \equiv (\frac{\pi}{2}, \frac{\pi}{2})$ for several t' and t'' and $J = 0.4$. 31

3.1 Slave boson mean-field phases. 41

Chapter 1

Introduction

Virtue lies in the middle.

Aristotle

1.1 Motivation

Following the discovery of superconductivity in $(LaBa)_2CuO_4$ below $T_c = 35K$ by Bednorz and Müller [1] the frenzy that suddenly set stage among the condensed matter community culminated with the discovery of a large family of superconducting perovskite materials whose maximum T_c is approximately 160K. All such compounds have in common the copper-oxide layers, thereby being known as the "cuprates". Superconductivity had been discovered quite some time ago, namely by Kamerlingh Onnes in 1911 [2], but by the middle of the 80's superconductivity required temperatures lower than about 20K to set in. Various factors contributed to the high-T_c hype. Clearly, materials that are perfect conductors and perfect diamagnets upon cooling with liquid nitrogen call for many technological applications. Equally remarkable is the fact that cuprates superconduct when insulating materials are subjected to a small chemical doping procedure. And they do so better than any metal or alloy ever discovered. This is a most fantastic observation under the BCS paradigm which applies with unscratched success to conventional superconductors, *i.e.* all those discovered prior to the cuprates. The theory of superconductivity by Bardeen, Cooper and Schrieffer [3, 4], a.k.a. BCS, established that metals, not insulators, face a transition into the superconducting state at low enough temperatures due to the effectively attractive interaction mediated by lattice vibrations. The short version of the BCS story goes as follows: electrons are attracted to each other, thereby forming electron pairs, also known as Cooper pairs; these pairs are bosonic-like and are allowed to condense; the resulting phase coherence, which underlies phenomena like flux quantization and the Josephson effect, defines superconductivity. These same phenomena, which are intrinsic to off-diagonal long-range order, are observed in cuprate superconductors [5, 6]. In particular, flux quantization experiments demonstrate that the building blocks of the cuprate superconducting state are charge $2e$ electron Cooper pairs [5, 7, 8]. There is also ample experimental evidence that low energy quasiparticles in cuprate

superconductors are well defined, long-lived, excitations of the Bogoliubov type, *i.e.* constitute proper coherent superpositions of electrons and holes as dictated by BCS mean-field theory [9, 10, 11, 12]. All of the above sustain that cuprates are standard superconductors, in the sense that the superconducting state in these materials is adiabatically connected to that of all other known superconductors. Yet, going back to the above allusion, superconductivity is encountered in cuprate samples that do not differ that much from insulator materials. This fact reflects itself in many ways, and the phenomenology of cuprate superconductors displays several deviations from that expected solely from the BCS pairing mechanism acting on Fermi liquid metals.

A first sign hinting that the microscopic physics of cuprates is distinct is that electrons pair up in the d-wave channel [13]. All conventional metals and alloys select s-wave pairing as a way to optimize the pairing energy. This effect by itself has dramatic consequences in the phenomenology of superconducting cuprates. The pairing symmetry implies the existence of ungapped excitations at four points in the Brillouin zone, with obvious consequences in transport properties [14]. Interestingly, these d-wave nodal quasiparticles are extremely robust and preserve their character until very close to the insulating phase [15, 12, 16]. A particular striking deviation from BCS predictions is that as samples are brought closer to the insulating chemical composition the gap that measures the pairing strength increases in magnitude [12] while, at the same time, the superfluid density and T_c are observed to vanish [17]. In BCS theory all three quantities go hand in hand. The gap increase means that it costs more energy to break a Cooper pair, which by itself is consistent with the decrease in coherence length. In the underdoped regime, the one closest to the insulating limit and where more novel phenomenology is encountered, the coherence length is so small that Cooper pairs are the size of a few lattice spacings. Such small Cooper pairs are prone to large fluctuations which, one may try to argue, kill long-range superconducting phase coherence. The validity of the resulting strong coupling BCS scenario in the context of underdoped cuprate superconductors would require that above a certain temperature scale experiments unveil the underlying parent Fermi liquid state. Nature, however, cares about physicists looking for what to do and chose otherwise. Indeed, deviations from Fermi liquid theory expectations breed above T_c. An impressive observation is that in optimally doped samples, the ones where chemical doping is adjusted to optimize for T_c, a linear in temperature resistivity is measured all the way to $\sim$ 1000K [18]. This behavior strongly contrasts with the T^2 law expected from Fermi liquid theory. Other remarkable effects probed in the underdoped regime are the unusual temperature dependence of the Knight shift [19], c-axis conductivity [20] and the Hall coefficient [21].

The Knight shift data particularly shows the reduction in the spin density of states at low energy consistent with the opening of a spin-gap. Similar evidence for a gap is presented by angle-resolved photoemission spectroscopy (ARPES) measurements, which further detect the location of the gap at $(0, \pi)$ and $(\pi, 0)$ [22]. The unusual depletion in the low energy density of states is the hallmark of what became known as the pseudogap regime of underdoped cuprates. The very existence of a gap motivates the search for the eventual order parameter responsible for destroying the large Fermi surface in the metallic normal state. Following the aforementioned reduction

of the superfluid density with x, the level of chemical hole doping in the CuO_2 layers away from the half-filling insulating composition, as well as that of the Bogoliubov quasiparticle spectral weight [23, 24] in the superconducting state, the finite Drude weight in the pseudogap normal metallic state also scales with x [22]. Evidence for charge carrier density varying with x [25] instead of $1-x$, as expected from counting the number of electrons in the conducting copper-oxide planes, further suggests the breaking of translation symmetry. However, there is no experimental evidence for any true phase transition in the normal state above the superconducting T_c and the order underlying pseudogap phenomenology, be it stripes, d-density wave (or should I say staggered flux) if any, is hidden. Whether because of fluctuations or due to impurity effects has still to be determined. The proximate Néel state always observed near half-filling offers yet another appealing way to account for the charge carrier density equal to x. The truth, though, is that ARPES presents no evidence for the required hole pockets. Additionally, long-range antiferromagnetic order is frustrated very rapidly upon doping and the phase diagram where the pseudogap regime and the large superconducting dome pop up is mostly covered by paramagnetic states. To make the last statement more precise, note that Néel ordering does not survive beyond $x \approx 0.01-0.03$ while superconductivity emerges in the $x \approx 0.05-0.25$ doping range.

An attractive alternative came from Anderson in the heyday of the high-T_c discovery [26]. Anderson's wit skipped many a calculation and proposed the minimal model to rationalize the observations (many to come!) in the cuprates. According to Anderson, theorists do not have to bother with the full and complicated chemical structure of the cuprates. To focus on the copper-oxide layers is enough. Actually, the copper-oxide layers are more complicated than needed and, instead of a three-band model describing the Cu and the two O atoms per unit cell, one can effectively consider a single-band model. Following the strong interactions in the copper $3d$ orbitals, which contribute with one spin-1/2 per unit cell, the parent compounds are Mott insulators (meaning that based solely on Fermi-Dirac statistics these materials should be metallic). The consequent superexchange mechanism provides the proper antiferromagnetic sign to the exchange interaction between the localized spins underlying the observed Néel ordering. Away from half-filled compositions, the copper-oxide layers are doped Mott insulators and, following Anderson once again, that implies the phenomenology does not fall within Landau's Fermi liquid realm. The resulting Hamiltonian to be studied is the one-band Hubbard model or, if you want to make it simpler, the tJ model (somewhat related but not equivalent to the large on-site repulsion U limit of the Hubbard model), on a 2D square lattice. In order to facilitate life to a lot of people, Anderson also proposed the "solution" to the model. The groundstate wave function is related, one way or the other, to projected BCS states. These are standard BCS wave functions where on-site double electron occupancy is forbidden (thereby projected out). The physical picture is that of vacancies moving in a liquid state of short-ranged singlet bonds that resonate throughout the lattice. Not surprisingly, such states are known as resonating valence bond states, or merely RVB states, and lay the ground to understand some of the aforementioned pseudogap phenomenology: the energy cost to break the singlet bonds reduces the low energy

spin density of states and opens a gap in the ARPES spectrum; the liquid nature of the resonating bonds is consistent with the lack of any phase transition above T_c and favors the mobility of charge carriers, namely the vacancies, whose concentration is x; superconductivity arises from the coherence of vacancies and, therefore, the superfluid density naturally scales with x.

Following Anderson's insights a whole industry was set to check and borrow from his claims, to study the tJ and the Hubbard models, to understand the nature of RVB states and the related notion of spin-charge separation above 1D. A long path has been traveled since Anderson's 18 year old paper and an awful lot has been learned. The field of condensed matter physics has in some sense been reshaped and people started talking about gauge fields and proposing theories of the universe [27, 28]. Gauge fields are a complicated matter, thus illustrating that even the simplified version of the high-T_c problem proposed by Anderson is far from resolved. Over the last 18 years both experiments and numerical methods improved dramatically and people still debate to a bigger or lesser degree the above described picture of the cuprates. As we further detail in what follows, the aim of this thesis is to contribute with new theoretical methods to address the tJ model and to verify to what extent it provides a suitable description of the cuprates.

1.2 Doped Mott insulators

The simplest model to address the physics of doped Mott insulators as of interest to the cuprates is the generalized-tJ model:

$$H_{tJ} = J \sum_{\langle ij \rangle \in NN} \left(\boldsymbol{S}_i . \boldsymbol{S}_j - \frac{1}{4} n_i n_j \right) - \sum_{\langle ij \rangle} t_{ij} \mathcal{P} \left(c_i^\dagger c_j + c_j^\dagger c_i \right) \mathcal{P} \tag{1.1}$$

The all important operator $\mathcal{P}$ in the above Hamiltonian projects out states where two electrons sit on the same site. Therefore, at half-filling there is exactly one electron per lattice site and the Hilbert space reduces to that of a pure spin Hamiltonian. In that case, only the first term in (1.1), which describes the Heisenberg exchange interaction between different spins on the 2D square lattice, contributes. For $J > 0$ spins develop antiferromagnetic correlations and the groundstate is Néel ordered. Away from half-filling the second term in (1.1) describes the hopping of electrons along otherwise empty sites.

The relevance of doped Mott insulators goes beyond the realm of high-T_c as they embody a long standing problem in condensed matter physics, namely how to reconcile local moments with itinerant electrons. The two extreme limits are well understood. To illustrate this statement, consider the generalized-tJ model (1.1). At half-filling it reduces to the Heisenberg model, which has been extensively studied. Even though the groundstate for the 2D square lattice is not known, there is ample evidence that it supports long-range Néel order [29]. In the opposite limit, that of small electron concentration, the projection operators are not relevant since double occupancy is extremely rare in the dilute case. Then we can start from Slater deter-

minant wave-functions and address the effect of the exchange interaction employing standard diagrammatic techniques, like RPA, which produce controlled approximation schemes since the kinetic and exchange energies are linear and quadratic in the electron density respectively. These considerations are obviously confirmed by the phase diagram of cuprates with the Néel phase at half-filling and the Fermi liquid metallic state at doping concentrations larger than $x \approx 0.25$. As always, the interesting regime lies in the middle, in the doping region that intervenes between the above two limits. Of course Nature is kind enough to offer us the (or at least one possible) solution. Superconductivity emerges. The problem is then to describe theoretically how superconductivity comes about, the properties of the resulting superconducting state and to understand how the above tendencies for localization and itinerancy conspire to produce the normal state phenomenology.

The intricacy of the generalized-tJ model follows from the mutual frustration of the Heisenberg and hopping terms. The former favors a staggered moment spin background. In that case, a vacancy hopping between two different sublattices leaves a ferromagnetic bond behind, which costs additional exchange energy. The hopping term thus acts in order to destroy antiferromagnetic correlations while the Heisenberg term constrains the motion of vacancies. Therefore, the physics of doped Mott insulators is that of finding the best compromise between the hole kinetic energy and the spin exchange energy. In other words, doped Mott insulators encode a duality between local and itinerant electrons. This duality is manifest in the two competing terms of the generalized-tJ model, namely the spin exchange and hole kinetic energies. The former is of order J whereas the latter scales with the vacancy density and is of order xt. This duality is unconcealed in experiments that show a large spin-gap energy scale, and for that matter a large d-wave superconducting gap energy, coexisting with a small coherence energy scale, as reflected in the superfluid density and T_c. Furthermore, such a duality is also demonstrated in the apparent separation of spin and charge degrees of freedom, insofar as it follows from the presence of a gap in the spin channel while the charge channel is gapless in the pseudogap metallic regime of cuprates.

1.3 Outline of the thesis

Of particular relevance to better comprehend the elusive phenomenology of underdoped cuprates is the limit of a spin lattice with a small density of vacancies, which thereby is the focus of this thesis.

The natural first step to address the properties of a dilute system of vacancies moving in a spin background is to focus on the interplay between a single vacancy and the encircling spins. That is precisely the starting point of this thesis. In Chapter 2 we use the exact diagonalization and the self-consistent Born approximation methods to revisit the one-hole problem in the $tt't''J$ model. This problem has been addressed over and over again throughout the last 18 years [30] but, apparently, its charm persists. Specifically, we show there exists a natural way to decompose the single hole wavefunction into two components, each one bearing features that either minimize the

exchange or the hole kinetic energy. Interestingly, to a remarkable level of accuracy, changing the relative importance of the Heisenberg and hopping sectors by modifying the ratio t/J only changes the relative weight of the aforementioned two components in the hole wave-function. The duality between exchange and hole kinetic energies then translates into an effective two-band picture where the vacancy selects to be surrounded by a superposition of two different spin backgrounds. It follows that there exist two preferred ways for the spins to screen the vacancy. One displays a staggered magnetization as favored by the Heisenberg sector of the Hamiltonian (1.1). The other appears as if the spin of the doped hole spreads away from the vacancy in order to facilitate *inter*-sublattice hopping. In Chapter 2 we additionally show that the above two spin screening configurations renormalize *intra*-sublattice hopping in distinct ways and argue that underlies the nodal-antinodal dichotomy observed in experimental data. This dichotomy corresponds to the different character of excitations in the $(\frac{\pi}{2}, \frac{\pi}{2})$ and the $(0, \pi)$ regions of momentum space as probed directly by ARPES [31]. The results in Chapter 2 support such a momentum space anisotropy reflects the intrinsic duality of doped Mott insulators referred to in Sec. 1.2. Indeed, the duality between local moments and itinerant electrons and between the exchange and hole kinetic energies emerges as a duality between a vacancy dressed by staggered moments and a vacancy dressed by a liquid spin state. Since staggered moments and liquid spin states influence the hole dynamics in distinct ways, they are preferred in some regions of momentum space over the others, thereby inducing the aforementioned anisotropy.

The calculations in Chapter 2 concern lattices as small as 4×4. Still, the corresponding results reproduce the momentum space anisotropy implied by various experimental probes and, thus, constitute evidence for the role played by local spin correlations in determining the dynamics of holes in strongly correlated systems. In the remaining chapters of the thesis we take the viewpoint that the interplay between the hole dynamics and different short-range spin correlations is crucial to produce the phenomenology of underdoped cuprates.

In Chapter 3 we use the well known slave boson approach [32] to address the generalized-tJ model analytically. This approach, which implements the RVB scheme put forward by Anderson, provides the formalism to describe vacancies encircled by the aforementioned liquid spin configuration that enhances the hole kinetic energy. At mean-field level, the slave boson approximation has been considered for the tJ model, which only includes nearest-neighbor hopping. In Chapter 3 we extend the previous slave boson mean-field studies to the $tt'J$ model. The inclusion of next-nearest-neighbor hopping breaks particle-hole symmetry and distinguishes between the hole and electron doped regimes which, experiments tell us, have their own peculiarities. In addition, the extra hopping parameter expands the range of mean-field states to consider. As a result we look for scenarios where the slave boson gauge structure is broken to Z_2, thus implying the true separation of spin and charge degrees of freedom. The main result of Chapter 3 is that a Z_2 state with spin-charge separation might appear as the metallic pseudogap regime of electron doped cuprates, but not of their hole counterparts.

At the level of the mean-field approximation the slave boson approach cannot

fully address the dynamics of doped holes since it assumes vacancies are dressed by a liquid spin background. Indeed, from Chapter 2 we know that short-range staggered moment correlations also affect the hole dynamics. In Chapter 4 we develop a new formulation of the $tt't''J$ model that explicitly captures the interplay between the hole dynamics and the correlations, whatever they are, of the spin background. In this formulation the $tt't''J$ is explicitly written in terms of hole operators, instead of electron operators as in (1.1), and we dub it the "doped carrier" formulation of the $tt't''J$ model. This result provides us with a new starting point to develop a mean-field theory of doped Mott insulators which accounts for the role of both staggered moment and spin singlet bond local correlations in the dynamics of vacancies. To motivate the relevance of the new "doped carrier" mean-field theory we use model parameters borrowed from band calculations and from fitting ARPES data to obtain a mean-field phase diagram that reproduces semi-quantitatively that of hole and electron doped cuprates.

Following the dramatic improvement in sample quality, particularly so in the deeply underdoped regime, as well as experimental resolution, many non-trivial results have recently illuminated the deviations between conventional superconductors and the cuprates, which are strongly correlated superconductors. A large body of experimental evidence for which no simple and well established explanation exists has thus been provided. In Chapters 5 and 6 we determine the hole dynamics for the new mean-field theory and extensively compare the mean-field results to experimental data concerning ARPES and tunneling conductance measurements on cuprate superconducting samples. The resulting good agreement is very suggestive, particularly so because our results originate exclusively from a mean-field description which, apparently, provides a rational not only to understand ARPES and tunneling experiments but also to connect both sets of data. These findings support that various aspects of the cuprate phenomenology can be grasped in terms of the local interplay between hole motion and the spin background and that, in particular, accounting for short-range antiferromagnetic and spin singlet d-wave pair correlations alone goes a long way in reproducing experiments.

The last chapter provides some conclusive remarks to a, hopefully, consistent story told throughout the thesis. It includes several considerations, such as the description of the simple picture that emanates from the "doped carrier" formulation of the $tt't''J$ model, the discussion of simplifications incurred during the derivation of the mean-field theory, the comparison between the (well established) slave boson and the (new) "doped carrier" approaches, as well as some general comments as to how the whole thing relates and applies to the phenomenology of cuprates.

Most of the work presented in this thesis has been published or made available one way or the other. Chapter 2 is adapted from a paper that has been submitted for publication and that is available at cond-mat/0409002. Chapter 3 is a somewhat larger version of the paper published in the Phys. Rev. B **68**, 024501 (2003). Chapters 4 and 5 are adapted from the long paper that is still in preparation and which details the results published in the Phys. Rev. Lett. **95**, 057001 (2005). Finally, Chapter 6 concerns research results to be presented in a paper that is currently in preparation.

Chapter 2

Momentum space anisotropy in doped Mott insulators

All politics is local.

Thomas P. O'Neill

2.1 Introduction

It is known, both experimentally and theoretically, that doped Mott insulators can be significantly anisotropic in momentum space. Explaining this behavior is relevant to understanding the properties of metals close to the Mott insulating state, like the pseudogap regime in high-T_c superconductors [31, 33].

The pseudogap measured by angle-resolved photoemission spectroscopy (ARPES) is the energy difference between the one-electron spectral features at the nodal $[\vec{k} = (\pm\frac{\pi}{2}, \pm\frac{\pi}{2})]$ and antinodal points $[\vec{k} = (\pi, 0), (0, \pi)]$ [22]. This difference, which increases as both the temperature and the level of doping in the CuO_2 layers are reduced, is accompanied by the anisotropic behavior in momentum space suggested by various experimental observations [22, 31, 23, 34, 35, 36, 37, 38]. Indeed, the deeply hole underdoped regime shows a nodal-antinodal dichotomy as low energy quasiparticle peaks exist around the nodes while there is no evidence of quasiparticle-like behavior near the antinodal points [31, 23, 34]. In electron underdoped cuprates, low energy spectral weight appears around $(\pi, 0)$ instead as the pseudogap is pushed toward the zone diagonal [39]. Interestingly, Raman spectroscopy [40] and the violation of the Wiedemann-Franz law [41] in electron doped materials suggests the presence of chargeless excitations around $(\frac{\pi}{2}, \frac{\pi}{2})$. Hence, the pseudogap in the one-particle dispersion appears to strongly reduce the electronic character of excitations in the pseudogap region.

Strongly correlated materials close to the Mott insulator transition are notorious for the near degeneracy of different ordered states, some of which have been argued to provide a scattering mechanism that reduces quasiparticle features in the pseudogap region [31, 36, 42, 43]. In this chapter, we propose a different scenario to understand the observed momentum space anisotropy. In particular, we argue that states close

to $(\frac{\pi}{2}, \frac{\pi}{2})$ and $(\pi, 0)$ are different because, due to the competition between the spin exchange energy and the hole kinetic energy, spins surrounding the hole in states near $(\frac{\pi}{2}, \frac{\pi}{2})$ behave differently from the spins surrounding the hole in antinodal states [44, 45]. The nodal-antinodal dichotomy then reflects the existence of two distinct ways in which the lattice spins dress the doped holes.

The 2D $tt't''J$ model, which is the simplest model to study doped Mott insulators as of relevance to the cuprate systems, reproduces the experimental pseudogap dispersion and accounts for anisotropic behavior in momentum space [44, 45, 46, 47, 48]. Below, we employ the exact diagonalization and the self-consistent Born approximation techniques to study the single hole problem in the $tt't''J$ model and to address how the hole is screened by the local spins in different regions of momentum space. We find that the single hole states can be understood as the superposition of two distinct states, namely a hole-like quasiparticle state and a state where the hole strongly distorts the surrounding spins. Due to their different properties, in the pseudogap regime these states predominate in different parts of momentum space, thus leading to the disparity between the nodal and antinodal regions. Our results are valid for both hole and electron doped materials – for our purposes, the main distinction between the two regimes is that in the former the pseudogap opens in the antinodal region while in the latter it opens in the nodal region.

2.2 One-hole states

The single hole 2D $tt't''J$ Hamiltonian is

$$H_{tt't''J} = -\sum_{\langle ij\rangle,\sigma} t_{ij}\left(\widetilde{c}^{\dagger}_{i,\sigma}\widetilde{c}_{j,\sigma} + H.c.\right) + \sum_{\langle ij\rangle} J_{ij}\boldsymbol{S}_i.\boldsymbol{S}_j \tag{2.1}$$

where t_{ij} equals t, t' and t'' for first, second and third nearest neighbor sites respectively and vanishes otherwise. The exchange interaction only involves nearest neighbor spins for which $J_{ij} = J$. $\widetilde{c}_{i,\sigma}$ is the constrained operator $\widetilde{c}_{i,\sigma} = c_{i,\sigma}(1-n_{i,-\sigma})$. Unless otherwise stated, all our results come from the exact diagonalization of $H_{tt't''J}$ on a 4×4 lattice. Since we want to analyze how the hole affects the local configuration of the surrounding spins we believe that the study of such a small lattice is relevant. We also present results from the self-consistent Born approximation approach to the tJ model [49, 50, 51] on a 16×16 lattice to further support the exact diagonalization analysis.

In this chapter we only consider $0.2 < J < 0.8$ (units are set so that $t = 1$). This range includes the physically relevant regime $J \approx 0.4$ and is large enough that it covers an interval ΔJ which is of the order of the maximum value of J. We do not extend our calculations down to $J = 0$ because for $J \approx 0$ the hole forms ferromagnetic polarons that eventually lead to the Nagaoka instability. Therefore, the physics for $J \approx 0$ is specific to that limit and is not relevant to the cuprates. Our calculations can be performed for $J > 0.8$ but we find that brings no added understanding to our results and conclusions.

In what follows, we only consider the lowest energy single hole state for each momentum $\boldsymbol{k}$, which we denote by $|\psi_{\boldsymbol{k}}, J, t't,''\rangle$. Here J, t' and t'' label the model parameters that define the Hamiltonian $H_{tt't''J}$ for which $|\psi_{\boldsymbol{k}}, J, t't,''\rangle$ is an eigenstate (as found upon the exact diagonalization of $H_{tt't''J}$). Below we discuss the sharpness of quasiparticle features at different locations in momentum space in terms of the quasiparticle spectral weight

$$Z_{\boldsymbol{k},J,t't,''} = |\langle \psi_{\boldsymbol{k}}, J, t', t''| \, \widetilde{c}_{\boldsymbol{k},\sigma} \, |\text{HF GS}\rangle|^2 \tag{2.2}$$

where the ket $|\text{HF GS}\rangle$ denotes the groundstate of the half-filled system. For all $\boldsymbol{k}$, t' and t'' there exists a certain $J_c(\boldsymbol{k}, t', t'')$ such that $|\psi_{\boldsymbol{k}}, J, t', t''\rangle$ has zero quasiparticle spectral weight for $J < J_c(\boldsymbol{k}, t', t'')$. The intuition behind this result is that for small enough J the half-filled system spin configuration is so soft that the doped hole dramatically modifies the spin background. The aforementioned Nagaoka instability perfectly illustrates this state of affairs. Introducing additional notation, we denote the ket $|\psi_{\boldsymbol{k}}, J, t't,''\rangle$ by $\left|\widetilde{U}_{\boldsymbol{k}}, J, t', t''\right\rangle$ whenever $J < J_c(\boldsymbol{k}, t', t'')$. Therefore, by definition, $\left|\widetilde{U}_{\boldsymbol{k}}, J, t', t''\right\rangle$ has vanishing quasiparticle spectral weight. A major observation in this chapter, which we motivate in the rest of the section, is that for $J > J_c(\boldsymbol{k}, t', t'')$ it is a good approximation to write the eigenstate $|\psi_{\boldsymbol{k}}, J, t't,''\rangle$ as

$$|\psi_{\boldsymbol{k}}, J, t', t''\rangle \cong q(\boldsymbol{k}, J, t', t'') \, |Q_{\boldsymbol{k}}, t', t''\rangle + u(\boldsymbol{k}, J, t', t'') \, |U_{\boldsymbol{k}}, t', t''\rangle \tag{2.3}$$

in a large range of values of J. In (2.3) $|Q_{\boldsymbol{k}}, t', t''\rangle$ and $|U_{\boldsymbol{k}}, t', t''\rangle$ are orthonormal states whose definition (see below) does not depend on J[1]. On the other hand, $q(\boldsymbol{k}, J, t', t'')$ and $u(\boldsymbol{k}, J, t', t'')$ are J-dependent coefficients that obey the normalization condition

$$|q(\boldsymbol{k}, J, t', t'')|^2 + |u(\boldsymbol{k}, J, t', t'')|^2 = 1 \tag{2.4}$$

The interpretation of expression (2.3) is that, in a certain range of J values, the eigenstates $|\psi_{\boldsymbol{k}}, J, t't,''\rangle$ determined for the various values of J in this range define a curve in the single hole $tt't''J$ model Hilbert space which approximately lies in a 2D plane. The physical content of this statement is presented below.

First, however, let us motivate the result expressed in (2.3). We start by considering the $t', t'' = 0$ case and we find $J_c(\boldsymbol{k}, t' = 0, t'' = 0) < 0.2$ for all $\boldsymbol{k}$ in Table 2.1. In this table we show that for all J in the interval $[0.2, 0.8]$ the states $|\psi_{\boldsymbol{k}}, J, t' = 0, t'' = 0\rangle$ have almost unit overlap with the 2D plane in the single hole $tt't''J$ model Hilbert space defined by the kets $|\psi_{\boldsymbol{k}}, J = 0.2, t' = 0, t'' = 0\rangle$ and $|\psi_{\boldsymbol{k}}, J = 0.6, t' = 0, t'' = 0\rangle$. This statement is true for all momenta $\boldsymbol{k}$ considered and, as shown in Table 2.1, the self-consistent Born approximation technique leads to the same conclusion, thus supporting that this result is not specific to the 4×4 lattice used in the exact diago-

[1]Note the difference between the kets $\left|\widetilde{U}_{\boldsymbol{k}}, J, t', t''\right\rangle$ and $|U_{\boldsymbol{k}}, t', t''\rangle$. The former is *J-dependent* and is defined for $J < J_c(\boldsymbol{k}, t', t'')$. The latter is *J-independent* and is defined (below) for $J > J_c(\boldsymbol{k}, t', t'')$. We use similar notation for both, since in Sec. 2.3 we argue both have similar properties in the parameter regime of interest to the cuprates.

	J	0.3	0.4	0.5	0.6	0.7	0.8
	$(\frac{\pi}{2}, \frac{\pi}{2})$	0.9994	0.9994	0.9998	1	0.9998	0.9990
$t' = 0$	$(\pi, 0)$	0.9994	0.9994	0.9998	1	0.9998	0.9990
$t'' = 0$	$(\pi, \frac{\pi}{2})$	0.9972	0.9977	0.9993	1	0.9992	0.9970
ED	$(\frac{\pi}{2}, 0)$	0.9975	0.9980	0.9994	1	0.9994	0.9977
	$(0, 0)$	0.9946	0.9923	0.9963	1	0.9938	0.9766
	$(\frac{\pi}{2}, \frac{\pi}{2})$	0.9996	0.9996	0.9998	1	0.9998	0.9990
$t' = 0$	$(\pi, 0)$	0.9994	0.9994	0.9998	1	0.9997	0.9986
$t'' = 0$	$(\pi, \frac{\pi}{2})$	0.9989	0.9988	0.9996	1	0.9995	0.9978
SCBA	$(\frac{\pi}{2}, 0)$	0.9989	0.9988	0.9996	1	0.9995	0.9978
	$(0, 0)$	0.9016	0.9005	0.9766	1	0.9842	0.9488
	$(\frac{\pi}{2}, \frac{\pi}{2})$	0.9994	0.9994	0.9998	1	0.9998	0.9990
$t' = -0.2$	$(\pi, 0)$	–	1	0.9998	0.9997	0.9999	1
$t'' = 0.1$	$(\pi, \frac{\pi}{2})$	0.9936	0.9952	0.9986	1	0.9987	0.9950
ED	$(\frac{\pi}{2}, 0)$	0.9907	0.9943	0.9986	1	0.9988	0.9957
	$(0, 0)$	0.9880	0.9856	0.9943	1	0.9940	0.9807

Table 2.1: Square of the overlap of $|\psi_{\boldsymbol{k}}, J, t', t''\rangle$ with the Hilbert space $\{|\psi_{\boldsymbol{k}}, J = 0.2, t', t''\rangle, |\psi_{\boldsymbol{k}}, J = 0.6, t', t''\rangle\}$ for different J and $\boldsymbol{k}$. Both exact diagonalization (ED) and self-consistent Born approximation (SCBA) results are shown for $t', t'' = 0$. Exact diagonalization results are also shown for $t' = -0.2$, $t'' = 0.1$. For $t' = -0.2$, $t'' = 0.1$ and $\boldsymbol{k} = (\pi, 0)$ the Hilbert space $\{|\psi_{\boldsymbol{k}}, J = 0.4, t', t''\rangle, |\psi_{\boldsymbol{k}}, J = 0.8, t', t''\rangle\}$ is used instead.

nalization calculation[2].

A similar observation holds when $t', t'' \neq 0$. This fact is illustrated in Table 2.1 for $t' = -0.2$, $t'' = 0.1$. In this case we follow the same procedure as for $t' = t'' = 0$ but for one thing. When $\boldsymbol{k} = (\pi, 0)$ and $t' = -0.2$, $t'' = 0.1$ we find that $0.3 < J_c < 0.4$ and, therefore, we do not use $J = 0.2$ in order to motivate the approximate equality in (2.3) since we only claim it applies for $J > J_c(\boldsymbol{k}, t', t'')$. Instead, for $\boldsymbol{k} = (\pi, 0)$ and $t' = -0.2$, $t'' = 0.1$ we rather use the states $\left|\psi_{\boldsymbol{k}=(\pi,0)}, J = 0.4, t' = -0.2, t'' = 0.1\right\rangle$ and $\left|\psi_{\boldsymbol{k}=(\pi,0)}, J = 0.8, t' = -0.2, t'' = 0.1\right\rangle$ to illustrate the validity of (2.3).

The results in Table 2.1 motivate the form of Expression (2.3) but we are still free to define $|Q_{\boldsymbol{k}}, t', t''\rangle$ and $|U_{\boldsymbol{k}}, t', t''\rangle$, which lie in the aforementioned 2D plane in the single hole $tt't''J$ model Hilbert space. A physically sensible choice comes from requiring $q(\boldsymbol{k}, J, t', t'')$ to increase with J while $u(\boldsymbol{k}, J, t', t'')$ decreases. Since cranking up J enhances the quasiparticle features of doped carriers [49], the above condition is automatically satisfied if the quasiparticle spectral weight of $|U_{\boldsymbol{k}}, t', t''\rangle$ vanishes. This prescription uniquely determines Q states ($|Q_{\boldsymbol{k}}, t', t''\rangle$) and U states ($|U_{\boldsymbol{k}}, t', t''\rangle$), which we remark are not eigenstates of $H_{tt't''J}$[3]. Following the above construction Q states have a large quasiparticle spectral weight: for all values of t' and t'' used in this chapter we find $0.5 < \frac{|\langle Q_{\boldsymbol{k}}|\tilde{c}_{\boldsymbol{k},\sigma}|\text{HF GS}\rangle|^2}{|\langle \text{HF GS}|\tilde{c}^{\dagger}_{\boldsymbol{k},\sigma}\tilde{c}_{\boldsymbol{k},\sigma}|\text{HF GS}\rangle|} < 0.8$ for momentum space vectors around the $(0, \pi) - (\pi, 0)$ line[4].

The previous argument points out that the eigenstates $|\psi_{\boldsymbol{k}}, J, t't,''\rangle$ have features that get enhanced by an increasing J and features that become more pronounced when J is reduced. By definition, Q and U states capture these features and, not surprisingly, below we show they display distinct physical properties: in Q states the spin antiferromagnetic correlations are robust to the presence of the hole while in U states the spins rearrange to facilitate hole hopping. On general grounds, a construction similar to the above one might be valid for models other than the 2D $tt't''J$ model. The significant fact about this model is that, for experimentally relevant parameters, the overlap of both Q and U states with $|\psi_{\boldsymbol{k}}, J, t', t''\rangle$ is large and exhibits a considerable momentum dependence. Since Q states have strong quasiparticle features while U states have vanishing quasiparticle spectral weight, this momentum dependence leads to an anisotropic in momentum space quasiparticle character of excitations[5]. In the remainder of the chapter we discuss physical properties of Q and U states, explain

[2]The above choice of $J = 0.2$ and $J = 0.6$ could have been made different. However, any reasonable set of two values of J in the range $[0.2, 0.8]$ would conduct to similar conclusions.

[3]Given the validity of (2.3) the states $|Q_{\boldsymbol{k}}, t', t''\rangle$ and $|U_{\boldsymbol{k}}, t', t''\rangle$ are relatively insensitive to variations of the two values of J used to define the above mentioned 2D plane in the single hole $tt't''J$ model Hilbert space. In the limit these two values of J become infinitesimally close to each other, $|Q_{\boldsymbol{k}}, t', t''\rangle$ and $|U_{\boldsymbol{k}}, t', t''\rangle$ are constructed from the state vectors $|\psi_{\boldsymbol{k}}, J, t', t''\rangle$ and $\partial\,|\psi_{\boldsymbol{k}}, J, t', t''\rangle\,/\partial J$. Therefore, in general, for every value of $J > J_c(\boldsymbol{k}, t', t'')$ we can find the respective Q and U states.

[4]As it becomes clear in the remainder of the chapter, we are mostly interested in discussing the properties of states along the $(0, \pi) - (\pi, 0)$ line.

[5]The above formal construction to derive Q and U states can be applied, for instance, to the 3D $tt't''J$ model. However, we expect that U states derived for this model be of less relevance than those obtained for the 2D model since antiferromagnetic correlations are more robust in 3D. In that case, for all $\boldsymbol{k}$ vectors the wave-function is mostly of the Q type and quasiparticle properties are strong throughout momentum space.

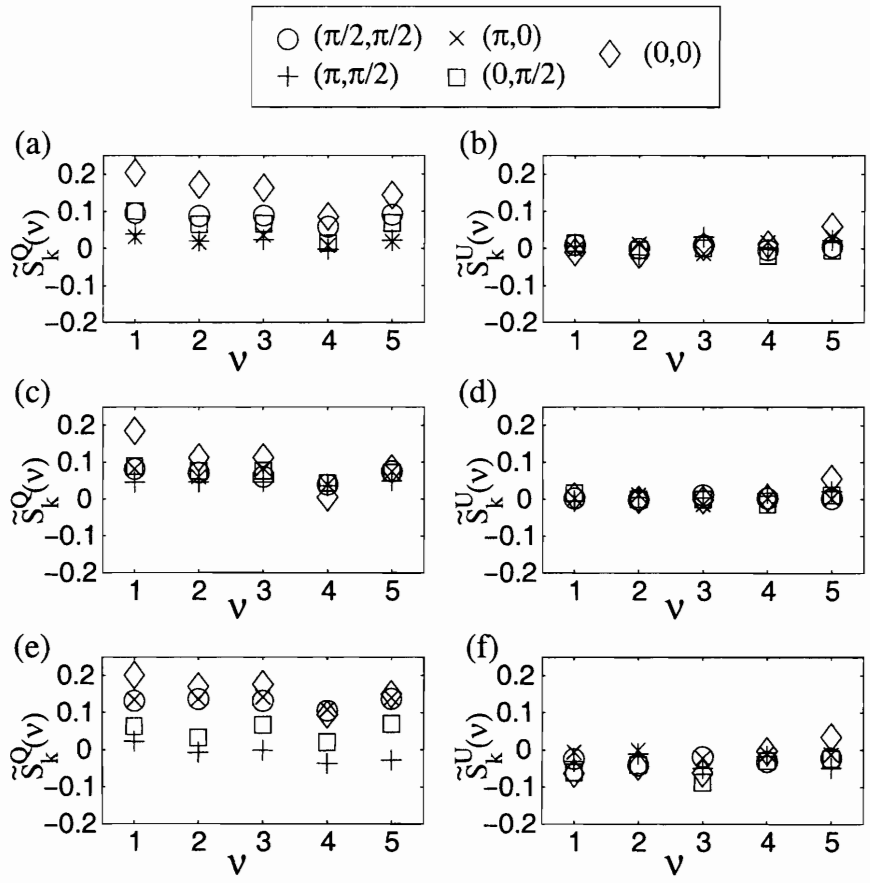

Figure 2-1: Average value of the staggered magnetization on sites that are ν^{th} nearest neighbors to the hole, $\widetilde{S}^Q_{\boldsymbol{k}}(\nu) \equiv \langle(-)^{i_x+i_y} S^Q_{\boldsymbol{k}}(\boldsymbol{i})\rangle_\nu$ and $\widetilde{S}^U_{\boldsymbol{k}}(\nu) \equiv \langle(-)^{i_x+i_y} S^U_{\boldsymbol{k}}(\boldsymbol{i})\rangle_\nu$, for different momenta $\boldsymbol{k}$. (a) and (b) $t' = -0.3, t'' = 0.2$. (c) and (d) $t', t'' = 0$. (e) and (f) $t' = 0.3, t'' = -0.2$.

how they underlie anisotropic behavior in momentum space and show this anisotropy can be strong in the regime of interest to the cuprate materials.

2.3 Properties of Q and U states

To explore how the hole affects the spin background in Q and U states consider the spin density pattern around the hole

$$S^Y_{\boldsymbol{k}}(\boldsymbol{i}) \equiv \langle Y_{\boldsymbol{k}}| \sum_j S^z_{j+i} \widetilde{c}_{j,+1/2} \widetilde{c}^\dagger_{j,+1/2} |Y_{\boldsymbol{k}}\rangle + \tfrac{1}{N-1}\tfrac{1}{2} \tag{2.5}$$

with Y=Q,U[6], as well as the hole momentum distribution function

$$n^{Y}_{\boldsymbol{k}}(\boldsymbol{q},\sigma) \equiv \langle Y_{\boldsymbol{k}}|\, \widetilde{c}_{-\boldsymbol{q},-\sigma}\widetilde{c}^{\dagger}_{-\boldsymbol{q},-\sigma}\,|Y_{\boldsymbol{k}}\rangle \tag{2.6}$$

for Y=Q,U. Figs. 2-1(a), 2-1(c) and 2-1(e) depict the staggered magnetization in Q states, $(-)^{i_x+i_y}S^{Q}_{\boldsymbol{k}}(\boldsymbol{i})$, for different $\boldsymbol{k}$, t' and t''. Since these states have a well defined quasiparticle character, the doped hole coexists with the staggered spin pattern inherited from the undoped system. For the same reason, the hole momentum distribution function $n^{Q}_{\boldsymbol{k}}(\boldsymbol{q},-\frac{1}{2})$ is peaked at $\boldsymbol{q}=\boldsymbol{k}$ while a smaller peak is also observed at $\boldsymbol{q}=\boldsymbol{k}+(\pi,\pi)$ due to the strong antiferromagnetic correlations [52].

U states have no quasiparticle weight and display quite different behavior. Indeed, Figs. 2-1(b), 2-1(d) and 2-1(f) show that in $|U_{\boldsymbol{k}}\rangle$ the antiferromagnetic spin pattern of the undoped system is destroyed and the staggered magnetization around the hole [given by $(-)^{i_x+i_y}S^{U}_{\boldsymbol{k}}(\boldsymbol{i})$] is very close to zero and even negative. Moreover, the hole momentum distribution function $n^{U}_{\boldsymbol{k}}(\boldsymbol{q},-\frac{1}{2})$ peaks around $\boldsymbol{q}=(\pi,\pi)$ for all momenta $\boldsymbol{k}$ [Fig. 2-2 (a)]. The same real and momentum space properties were checked to hold for $\widetilde{\mathrm{U}}$ states [these are the energy eigenfunctions $|\psi_{\boldsymbol{k}},J,t',t''\rangle$ when $J<J_c(\boldsymbol{k},t',t'')$]. This fact is illustrated for $\widetilde{\mathrm{U}}$ states concerning the parameter regime relevant to both hole doped cuprates ($J=0.4$, $t'=-0.3$, $t''=0.2$) and electron doped cuprates ($J=0.4$, $t'=0.3$, $t''=-0.2$) [46] in Table 2.2, which explicitly shows that in these states the hole density also peaks around (π,π) independently of the momenta $\boldsymbol{k}$.

According to the above spin density results the extra $S^z=-\frac{1}{2}$ spin introduced by doping spreads away from the vacancy in both U and $\widetilde{\mathrm{U}}$ states. The resulting loss of spin exchange energy is accompanied by a gain in hole kinetic energy, as it follows from the hole momentum distribution results which support that, in these states, the hole always lies around the bare band bottom [which is located at (π,π)]. This evidence resembles predictions from spin-charge separation scenarios. Indeed, within the slave boson formalism, the electron decays into a charged spinless holon, which condenses at (π,π), and a chargeless spinon, which describes the delocalized spin-$\frac{1}{2}$ that carries the remaining momentum. We should remark that our calculation involves equal time properties in a small lattice and does not aim to prove the existence of true spin-charge separation. However, it supports that in U and $\widetilde{\mathrm{U}}$ states the lattice spins screen the hole in conformity with short-range aspects of spin-charge separation phenomenology.

The previous results demonstrate that the local configuration of spins encircling the hole is quite different in Q and U states. In this context, it is important to remark that the influence of t' and t'' on the hole dispersion is sensitive to the surrounding spin environment (this aspect is addressed at length in Sec. 7.1). For instance, intrasublattice hopping is not frustrated by antiferromagnetic correlations and, indeed, the hole in Q states (which is surrounded by a spin configuration reminiscent of the undoped antiferromagnetic groundstate) strongly disperses along the $(0,\pi)-(\pi,0)$ line for $t',t''\neq 0$ (see Fig. 2-2). The opposite limit occurs, for example, in certain $U(1)$

[6]To reduce finite size effects we subtract the average magnetization $\frac{1}{N-1}\sum_j\langle S^z_j\rangle = -\frac{1}{N-1}\frac{1}{2}$, where N is the number of lattice sites.

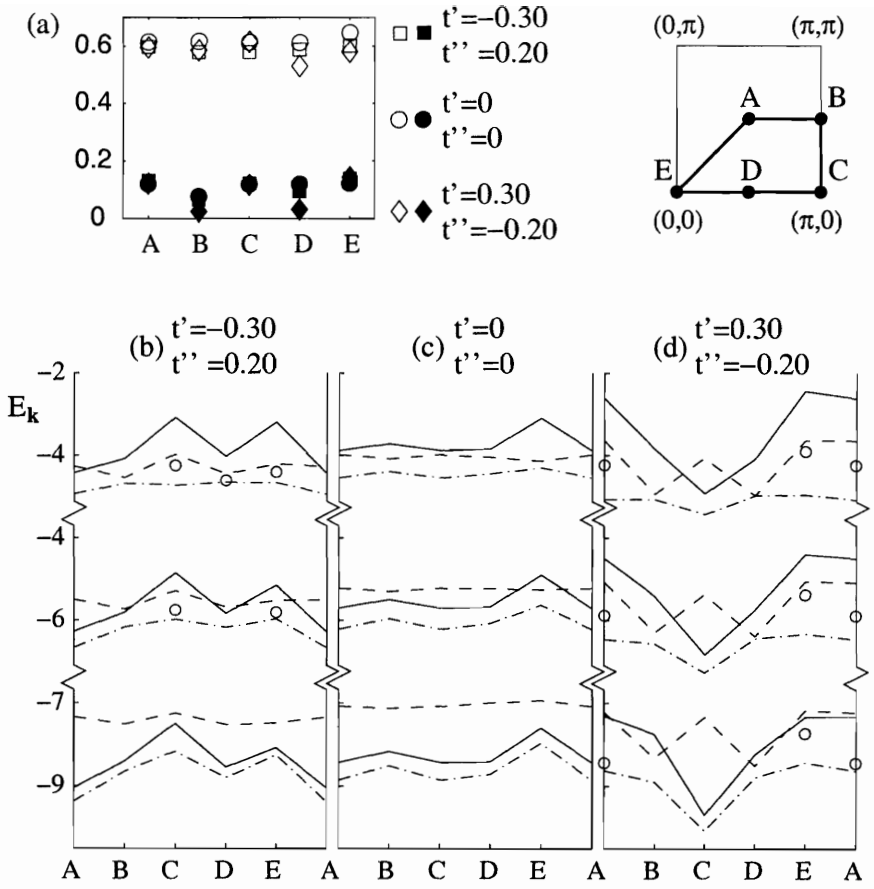

Figure 2-2: (a) $\sum'_{\boldsymbol{q}} n^U_{\boldsymbol{k}}(\boldsymbol{q}, -\frac{1}{2})$. Empty symbols involve sum over $\boldsymbol{q} = (\pi, \pi)$, $\boldsymbol{q} = (\pm\frac{\pi}{2}, \pi)$ and $\boldsymbol{q} = (\pi, \pm\frac{\pi}{2})$. Full symbols involve sum over $\boldsymbol{q} = (0, 0)$, $\boldsymbol{q} = (\pm\frac{\pi}{2}, 0)$ and $\boldsymbol{q} = (0, \pm\frac{\pi}{2})$. (b)-(d) Dispersion relations for $|Q_{\boldsymbol{k}}\rangle$ (full line), $|U_{\boldsymbol{k}}\rangle$ (dashed line) and $|\psi_{\boldsymbol{k}}\rangle$ (dash-dot line). Upper, middle and lower set of dispersions are obtained for J equal to 0.2, 0.4 and 0.7 respectively. ($\circ$) indicates the best energy obtained by a linear combination of $|Q_{\boldsymbol{k}}\rangle$ and $|U_{\boldsymbol{k}}\rangle$ when $J < J_c(\boldsymbol{k}, t', t'')$ (in which case $|\psi_{\boldsymbol{k}}\rangle = \left|\widetilde{U}_{\boldsymbol{k}}, J, t', t''\right\rangle$).

	$t' = -0.3; t'' = 0.2$		$t' = 0.3; t'' = -0.2$	
$\boldsymbol{k}$	$(\pi, 0)$	$(0, 0)$	$(\frac{\pi}{2}, \frac{\pi}{2})$	$(0, 0)$
$\boldsymbol{q} = (0, 0)$	0.0329	0.0343	0.0164	0.0328
$\boldsymbol{q} = (\pi, \pi)$	0.5437	0.6051	0.5293	0.5141

Table 2.2: $\sum'_{\boldsymbol{q}} n^{\widetilde{U}}_{\boldsymbol{k}}(\boldsymbol{q}, -\frac{1}{2}) \equiv \sum'_{\boldsymbol{q}} \left\langle \widetilde{U}_{\boldsymbol{k}} \right| \widetilde{c}_{-\boldsymbol{q}, \frac{1}{2}} \widetilde{c}^{\dagger}_{-\boldsymbol{q}, -\frac{1}{2}} \left| \widetilde{U}_{\boldsymbol{k}} \right\rangle$. $\boldsymbol{q} = (0, 0)$ results involve sum over $\boldsymbol{q} = (0, 0)$, $\boldsymbol{q} = (\pm\frac{\pi}{2}, 0)$ and $\boldsymbol{q} = (0, \pm\frac{\pi}{2})$. $\boldsymbol{q} = (\pi, \pi)$ results involve sum over $\boldsymbol{q} = (\pi, \pi)$, $\boldsymbol{q} = (\pm\frac{\pi}{2}, \pi)$ and $\boldsymbol{q} = (\pi, \pm\frac{\pi}{2})$. $J = 0.4$.

t'	t''	ΔE^{ψ}	ΔE^{Q}	ΔE^{U}	$W^{Q}_{\boldsymbol{k}'}$	$W^{Q}_{\boldsymbol{k}''}$
-0.3	0.2	0.69	1.43	0.22	0	0.75
-0.2	0.1	0.56	0.92	0.14	0.45	0.72
0	0	0	0	0	0.66	0.66
0.2	-0.1	-0.75	-1.08	-0.10	0.76	0.50
0.3	-0.2	-0.80	-2.33	-0.29	0.82	0

Table 2.3: ΔE^{Q}, ΔE^{U}, ΔE^{ψ} and $W^{Q}_{\boldsymbol{k}}$ with $\boldsymbol{k} = \boldsymbol{k'} \equiv (\pi, 0)$ and $\boldsymbol{k} = \boldsymbol{k''} \equiv (\frac{\pi}{2}, \frac{\pi}{2})$ for several t' and t'' and $J = 0.4$.

spin liquids, where the underlying spin correlations inhibit coherent intra-sublattice hopping (see Sec. 3.4). This limit is closer to what is observed in U states, as t' and t'' are heavily renormalized by the spin background (whose antiferromagnetic correlations are depleted by the hole nearest-neighbor hopping processes). In fact, Table 2.3 explicitly shows that for $t', t'' \neq 0$ $\Delta E^{Q} \equiv E^{Q}_{(\pi,0)} - E^{Q}_{(\pi/2,\pi/2)}$ is almost one order of magnitude larger than $\Delta E^{U} \equiv E^{U}_{(\pi,0)} - E^{U}_{(\pi/2,\pi/2)}$, where $E^{Q}_{\boldsymbol{k}} \equiv \langle Q_{\boldsymbol{k}}| H_{tt't''J} |Q_{\boldsymbol{k}}\rangle$ and $E^{U}_{\boldsymbol{k}} \equiv \langle U_{\boldsymbol{k}}| H_{tt't''J} |U_{\boldsymbol{k}}\rangle$.

2.4 Momentum space anisotropy

In the $tt't''J$ model the intra-sublattice hopping parameters t' and t'' control the dispersion $E^{\psi}_{\boldsymbol{k}} \equiv \langle \psi_{\boldsymbol{k}}| H_{tt't''J} |\psi_{\boldsymbol{k}}\rangle$ along $(0,\pi)-(\pi,0)$ and, thus, the pseudogap energy as well (this is the difference between the energy of $(0,\pi)$ and $(\frac{\pi}{2},\frac{\pi}{2})$ states, *i.e.* $\Delta E^{\psi} \equiv E^{\psi}_{(\pi,0)} - E^{\psi}_{(\pi/2,\pi/2)}$). Indeed, both Fig. 2-2 and Table 2.3 show that these parameters set the magnitude of the pseudogap, as well as its location in momentum space [48, 53].

We find that t' and t'' also control the difference in the quasiparticle character of $(\pi,0)$ and $(\frac{\pi}{2},\frac{\pi}{2})$ states, as supported by the dependence of the overlap integral $W^{Q}_{\boldsymbol{k}} \equiv |\langle \psi_{\boldsymbol{k}}|Q_{\boldsymbol{k}}\rangle|^2$ on these parameters (Table 2.3). Indeed, in Table 2.3 we see that for $J = 0.4, t' = -0.3, t'' = +0.2$ the $(\pi,0)$ and $(\frac{\pi}{2},\frac{\pi}{2})$ states have vanishing and large spectral weight respectively. If $t' = +0.3, t'' = -0.2$ instead it is the $(\frac{\pi}{2},\frac{\pi}{2})$ state whose spectral weight vanishes and the $(\pi,0)$ state that has large spectral weight[7].

The main message of this chapter is that the above roles of t' and t'', namely controlling the difference in energy and quasiparticle character between $(\pi,0)$ and

[7]The exchange constant J increases the robustness of the antiferromagnetic background and, thus, enhances quasiparticle-like behavior. Hence, larger values of J decrease the weight of U states throughout the Brillouin zone and, consequently, reduce any eventual anisotropy in momentum space. Interestingly, in the 2D $tt't''J$ model, both Q and U states overlap considerably with the eigenstates $|\psi_{\boldsymbol{k}}\rangle$ at the physically relevant value $J = 0.4$. For instance, when $t' = t'' = 0$ Table 2.3 shows that $W^{Q}_{\boldsymbol{k}}$ is reasonably close to 1/2 for both $\boldsymbol{k} = (\pi,0)$ and $\boldsymbol{k} = (\frac{\pi}{2},\frac{\pi}{2})$. Since t' and t'' shift weight between Q and U states differently in different momentum space regions, for $J = 0.4$ the relative strength of quasiparticle weight in different parts of momentum space is dramatically affected.

$(\frac{\pi}{2}, \frac{\pi}{2})$ states, can be understood with a simple two band picture involving Q and U states which captures the screening properties of the local spins encircling the hole. Indeed, as previously discussed, intra-sublattice hopping is frustrated in U states and the energies $E^U_{(\pi,0)}$ and $E^U_{(\pi/2,\pi/2)}$ have a small dependence on t' and t''. In contrast, $t' < 0$ and $t'' > 0$ clearly increase the energy $E^Q_{(\pi,0)}$ and clearly decrease $E^Q_{(\pi/2,\pi/2)}$ (Fig. 2-2). Since $|\psi_{\boldsymbol{k}}\rangle$ is a superposition of $|Q_{\boldsymbol{k}}\rangle$ and $|U_{\boldsymbol{k}}\rangle$, these t' and t'' induced changes in the energy of Q states push $E^\psi_{(\pi,0)}$ upward and lower $E^\psi_{(\pi/2,\pi/2)}$. Therefore, they increase the pseudogap energy ΔE^ψ. These changes also increase the energy difference $E^Q_{(\pi,0)} - E^U_{(\pi,0)}$ while reducing $E^Q_{(\pi/2,\pi/2)} - E^U_{(\pi/2,\pi/2)}$ and, as a result, $W^Q_{(\pi,0)}$ and $W^Q_{(\pi/2,\pi/2)}$ become smaller and larger respectively. For $J = 0.4, t' = -0.3, t'' = 0.2$ the energy $E^Q_{(\pi,0)}$ is so large that the minimum energy obtained by a linear combination of $\left|Q_{(\pi,0)}\right\rangle$ and $\left|U_{(\pi,0)}\right\rangle$ becomes higher than that of a different state $\left|\widetilde{U}_{(\pi,0)}\right\rangle$ with vanishing quasiparticle spectral weight. As a result, $W^Q_{(\pi,0)} = 0$. At the same time $W^Q_{(\pi/2,\pi/2)} = 0.75$ and the $(\frac{\pi}{2}, \frac{\pi}{2})$ state has strong quasiparticle character, so that a sharp disparity between nodal and antinodal states is encountered for these parameter values. Similar behavior is obtained when $t' > 0$ and $t'' < 0$ with the role of momenta $(\pi, 0)$ and $(\frac{\pi}{2}, \frac{\pi}{2})$ interchanged (Table 2.3).

The above argument shows that, in the pseudogap region, the kinetic energy of a hole surrounded by a staggered configuration of spins increases as the pseudogap gets larger. When this kinetic energy exceeds a certain value the spins around the hole lose their staggered pattern and, at short distances, the doped spin and charge separate. As a result, the quasiparticle character of states in the pseudogap region is strongly depleted. This same phenomenon, as reflected in experiments, is known as the nodal-antinodal dichotomy.

2.5 Conclusions

In this chapter we consider the $tt't''J$ model with a single hole to address the experimentally observed momentum space anisotropy in the underdoped regime of cuprates in terms of the interplay between the hole motion and the spin background correlations. The intra-sublattice hopping parameters control the dispersion along $(0, \pi) - (\pi, 0)$ and, therefore, the pseudogap energy as well. Furthermore, an increasing pseudogap is accompanied by a decrease of quasiparticle spectral weight for states in the pseudogap region. Our results agree with previous studies showing that the $tt't''J$ model is consistent with a sharp nodal-antinodal dichotomy in the parameter regime of interest to the cuprates [44, 45]. Here we argue this behavior naturally follows from local energetic considerations involing a hole hopping in a lattice of antiferromagnetically correlated spins, without the need to invoke the interaction of holes with other holes, an incipient order parameter or disorder. Specifically, we propose a simple two-band picture that identifies the regions of momentum space with strong quasiparticle features as those where local staggered moment correlations are important, whereas those parts of momentum space with depleted quasiparticle

character, namely the pseudogap region, bear signatures reminiscent of local spin-charge separation [44, 45]. We should mention that in Chapter 4 a new mean-field theory of the $tt't''J$ model is introduced which embodies the above two-band picture in the presence of a finite hole density. In particular, it describes the $tt't''J$ model as an effective two-fluid model of vacancies, which can be dressed by the above two different spin configurations. Chapters 5 and 6 show the corresponding mean-field results compare remarkably well with an extensive set of angle-resolved photoemission spectroscopy and tunneling conductance data. This agreement further supports the analysis in this chapter which intrinsically concerns local phenomena. We thus finally remark that the momentum space anisotropy observed in the cuprate materials can be addressed in terms of the role of *short-range* correlations and, therefore, represents generic behavior of doped Mott insulators [33].

Chapter 3

$SU(2)$ slave boson mean-field theory – possible Z_2 phase and spin-charge separation in electron doped cuprates

Separate we come, and separate we go, And this be it known, is all that we know.

Conrad Aiken

3.1 Introduction

A complete understanding of the behavior displayed by high temperature superconducting cuprates is still lacking. In these materials, d-wave superconducting (dSC) samples are obtained upon doping the parent compounds. The latter are Heisenberg antiferromagnets. The presence of low energy properties consistent with standard BCS theory in dSC samples is also generally undisputed. However, the phase-space region intervening between the two aforementioned regimes hosts unusual phenomenology – and a quite debated one as well. In this chapter, we capture the unconventional behavior in underdoped cuprates, which is controlled by the large Mott gap and the two-dimensional spin interactions in the copper-oxide planes [26], in terms of the slave boson approach to doped Mott insulators developed in Refs. [54, 55, 56] and [57, 58].

When a hole is doped into a spin system, it contributes with an electrical charge $+e$ and a spin-1/2. In the slave boson framework the charge is carried by a vacancy surrounded by a spin singlet configuration and the extra spin-1/2 is screened away by the spin background. Hence, the hole decays into two different excitations: one which carries charge, the holon, and another which carries spin, the spinon. These excitations are not free and, instead, interact through gauge fluctuations [57, 58, 59, 32]. The elementary properties of all these excitations and fluctuations are determined by the underlying spin liquid phase [57, 58, 59, 32]. While the $SU(2)$ slave boson MF phase diagram has been worked out for the tJ model [57], it has not been studied

how longer range hopping parameters, such as t', modify the MF phase diagram. Within the generalized-tJ model framework the next-nearest-neighbor (NNN) hopping parameter t' distinguishes between the hole doped (HD) and electron doped (ED) regimes of cuprate materials [60, 61] and accounts for the resulting different phenomenologies. In particular, t' was shown to control the robustness of antiferromagnetic (AF) [60] and dSC [62] correlations, and to change the electron spectral function [48] in accordance with experimental observations on HD and ED compounds [22]. Therefore, in this chapter we extend previous slave boson model studies to include the effect of NNN hopping processes.

Unlike in ED materials, the AF phase in HD compounds is feeble and a pseudogap metallic normal state appears in underdoped samples. This is a paramagnetic state with a $d_{x^2-y^2}$ gapped spectral function [22]. Reconciling the spectral gap with the strong local AF fluctuations is not trivial though [63]. One way to understand it is offered by the slave boson approach to the tJ model. Specifically, in the translation symmetric pseudogap metallic state proposed in Refs. [57, 58], the s-flux state, spinons and holons interact via a $U(1)$ gauge field. Despite the spinon d-wave gap in the s-flux state, the gauge interaction was shown to enhance AF fluctuations [63], in consonance with experiments. The $U(1)$ gauge fluctuations, which then play a key role in the AF instability at very low doping, also enhance quasiparticle-like properties [57, 58, 64, 32, 65]. In fact, the appearance of the spin-pseudogap below a certain energy and the existence of well defined electron-like quasiparticles in the nodal direction above T_c suggest that the $U(1)$ gauge field recombines the spin and charge degrees of freedom before the s-flux state reaches the dSC state [63].

As we enlarge the model parameter range to account for non-zero t' we can obtain new spin liquid states with properties fundamentally different from those in the $SU(2)$ slave boson MF phase diagram for the pure tJ model with $t' = 0$ [57, 58, 59]. In particular, a competing scenario to describe the crossover from the s-flux to the dSC phase, namely one that involves the emergence of an intervening state with a Z_2 gauge structure[66], may be encountered. This Z_2 state would result from the condensation of spinon bilinears [67, 68, 59] and the dSC state would then follow from holon condensation. Z_2 spin liquids are very interesting states with true spin-charge separation. They were predicted theoretically over ten years ago [67, 68] and yet they lack experimental realization. The present work proposes to study the conditions favoring the emergence of these spin liquid states as well as to discuss their relevance for the cuprate superconductors.

Despite the effort to check the applicability of Z_2 spin liquids in the context of high T_c superconductivity, so far all the experimental tests gave negative results[7, 8, 69, 70]. However, this does not imply that Z_2 states do not exist in high T_c samples. In this paper we find that Z_2 states are indeed unlikely to exist in HD compounds. But a Z_2-linear state (*i.e.* with linear gapless spinon excitations) may appear as the pseudogap metallic state for ED materials. In superconducting (SC) samples without AF order spin liquid pseudogap signatures may emerge once SC coherence is destroyed by thermal fluctuations or an external magnetic field. In the first case such a behavior is still to be reported. Experimental evidence in the magnetic field driven normal state, however, seems to be consistent with Z_2 pseudogap phenomenology

[71, 72, 73, 41].

In the first part of this chapter (Sec. 3.2) we extend the tJ model $SU(2)$ slave boson MF theory of Refs. [57, 58] to the $tt'J$ model. In Sec. 3.3 we present the resulting MF phase diagrams which for $t' < 0$ concern the HD regime and for $t' > 0$ address the ED case. For $t' < 0$ our calculations are consistent with the previous studies for $t' = 0$ where only the s-flux state was obtained. However, we find that NNN hopping can stabilize a Z_2-linear state in the $tt'J$ model for values of $t' > 0.5J$. These results show that unfrustrated hopping favors fractionalized phases (Sec. 3.4). In Sec. 3.5 we establish the link between our results and some properties of ED cuprates. We draw our main conclusions in Sec. 3.6.

3.2 Slave boson mean-field theory of the $tt'J$ model

The $tt'J$ model is given by the Hamiltonian

$$H_{tt'J} = H_{hf} + H_{hop} + H' \tag{3.1}$$

with

$$H_{hf} = J \sum_{\langle ij\rangle \in NN} \boldsymbol{S_i}.\boldsymbol{S_j} - \frac{1}{4}, \tag{3.2}$$

$$H_{hop} = -\sum_{\langle ij\rangle} t_{ij} \mathcal{P}(c_i^\dagger c_j + c_j^\dagger c_i)\mathcal{P}, \tag{3.3}$$

$$H' = \frac{1}{4} \sum_{\langle ij\rangle \in NN} 1 - n_i n_j, \tag{3.4}$$

where sums are taken over pairs of sites $\langle ij\rangle$. The exchange coupling J_{ij} is J for $\langle ij\rangle$ nearest-neighbor (NN) sites while the hopping parameter t_{ij} equals t for $\langle ij\rangle$ NN sites and t' for $\langle ij\rangle$ NNN sites. $\boldsymbol{S_i}$ is the spin on site i, $c_i^\dagger$ and $n_i = c_i^\dagger c_i$ are electron creation and occupation number operators and $\mathcal{P}$ projects out doubly occupied sites.

3.2.1 Slave boson mean-field theory of the Heisenberg Hamiltonian

We first consider the half-filling limit, in which case the $tt'J$ model (3.1) reduces to the Heisenberg Hamiltonian (3.2). The slave boson approach uses the fermionic spin representation $\boldsymbol{S}_i = \frac{1}{2} f_i^\dagger \boldsymbol{\sigma} f_i$, where $f_i^\dagger = [f_{i,\uparrow}^\dagger f_{i,\downarrow}^\dagger]$ is the spinon creation spinor operator [74]. Since H_{hf} is a pure spin-1/2 Hamiltonian, spinons are electric charge neutral and carry spin-1/2.

To derive a MF theory for the paramagnetic states of H_{hf} it is convenient to introduce the Nambu notation $\psi_i^\dagger = [\psi_{i,1}^\dagger \psi_{i,2}^\dagger] = [f_{i,\uparrow}^\dagger f_{i,\downarrow}^\dagger]$, in terms of which the spin

operators are written as $\boldsymbol{S}_i.\boldsymbol{\sigma} = \frac{1}{2}(\Psi_i^\dagger \Psi_i - I)$, where [56]

$$\Psi = \begin{bmatrix} \psi_{i,1} & \psi_{i,2}^\dagger \\ \psi_{i,2} & -\psi_{i,1}^\dagger \end{bmatrix} \tag{3.5}$$

and I is the identity matrix. It then follows

$$H_{hf} = -\frac{J}{8} \sum_{\langle ij \rangle \in NN} Tr\left[\widehat{U}_{ij}\widehat{U}_{ji}\right] + \sum_i \boldsymbol{a}_{0,i}.\left(\psi_i^\dagger \boldsymbol{\sigma} \psi_i\right) \tag{3.6}$$

with

$$\widehat{U}_{ij} = -\Psi_i \Psi_j^\dagger = \begin{bmatrix} \psi_{j,1}^\dagger \psi_{i,1} - \psi_{i,2}^\dagger \psi_{j,2} & \psi_{j,2}^\dagger \psi_{i,1} + \psi_{i,2}^\dagger \psi_{j,1} \\ \psi_{j,1}^\dagger \psi_{i,2} + \psi_{i,1}^\dagger \psi_{j,2} & \psi_{j,2}^\dagger \psi_{i,2} - \psi_{i,1}^\dagger \psi_{j,1} \end{bmatrix} \tag{3.7}$$

The Lagrangian multiplier field $\boldsymbol{a}_{0,i}$ is introduced in (3.6) to implement the $f_i^\dagger f_i = 1$ constraint on every site [75], since the on-site Hilbert space in the fermionic spin representation includes both the vacant and doubly occupied states.

The quartic fermionic terms in H_{hf} can be decoupled by means of the Hartree-Fock-Bogoliubov approximation to yield the quadratic MF Hamiltonian [57, 58]

$$\begin{aligned} H_{hf}^{MF} = & \frac{3J}{16} \sum_{\langle ij \rangle \in NN} Tr\left[U_{ij}U_{ji}\right] + \boldsymbol{a}_0.\left(\sum_i \psi_i^\dagger \boldsymbol{\sigma} \psi_i\right) \\ & - \frac{3J}{8} \sum_{\langle ij \rangle \in NN} \psi_i^\dagger U_{ij} \psi_j + h.c. \end{aligned} \tag{3.8}$$

where $U_{ij} = \langle \widehat{U}_{ij} \rangle$ are the singlet bond MF order parameters. Also note that at MF level the local constraint is relaxed and $\boldsymbol{a}_0$ is taken to be site independent. The best non-symmetry breaking MF parameters correspond to the d-wave ansatz [76, 57, 58]

$$\begin{aligned} U_{i,i+\hat{x}} &= \chi\sigma_z + \Delta\sigma_x \\ U_{i,i+\hat{y}} &= \chi\sigma_z - \Delta\sigma_x \\ \boldsymbol{a}_0 &= a_0\sigma_z \end{aligned} \tag{3.9}$$

This MF phase includes two different types of collective excitations, namely spin-1/2 spinons and gauge fluctuations [75, 57, 58]. The former have a d-wave dispersion with Dirac nodes at $(\pm\frac{1}{2}, \pm\frac{1}{2})$. The latter describe the fluctuations around the MF saddle point. To understand the nature of such fluctuations note that the physical spin operator $\boldsymbol{S}_i$ is invariant under an SU(2) transformation $\Psi_i \rightarrow SU(2) \times \Psi_i$ [56] and, as such, the fermionic representation of the Heisenberg model is intrinsically an $SU(2)$ lattice gauge theory [75, 57, 58, 59]. The effect of gauge fluctuations on the spin dynamics is to enhance the AF correlations of the spin d-wave gaped system [63].

The groundstate of the 2D Heisenberg model is believed to have AF long range order [29] unlike the above d-wave spin liquid state. Nevertheless, the energy of the projected d-wave state, namely $-0.319J$ per lattice bond [77], is close to the best

estimate for the AF ordered state, which is $-0.3346J$ [78]. This result suggests the possible relevance of the d-wave state to study the paramagnetic phases observed upon doping away from half-filling [32].

3.2.2 $SU(2)$ mean-field theory of the $tt'J$ model

To extend the above MF approach to the $tt'J$ model we further consider the hopping term (3.3). For the time being we neglect H', which gives a $O(x^2)$ correction to the MF Hamiltonian, where x is the hole concentration[1]. H_{hop} only acts on vacancies, which are objects that carry electric charge but no spin. In the slave boson approach, charged and spinless bosonic operators, known as holons, are introduced to keep track of such vacant sites [79, 80]. Specifically, each holon corresponds to a vacancy and, therefore, the doping level is $x = \frac{1}{N}\sum_i h_i^\dagger h_i$ where N is the number of lattice sites. In Ref. [57] holon operators $h_i^\dagger = [h_{i,1}^\dagger h_{i,2}^\dagger]$ were introduced without breaking the $SU(2)$ gauge structure observed in the Heisenberg model's fermionic representation.

The $tt'J$ model can be written in terms of spinons and holons using the expression for projected electron operators [57, 58, 81]

$$\mathcal{P}\begin{bmatrix} c_{i,\uparrow} & c_{i,\downarrow} \\ c_{i,\downarrow}^\dagger & -c_{i,\uparrow}^\dagger \end{bmatrix}\mathcal{P} = \frac{1}{\sqrt{2}}\begin{bmatrix} h_{i,1}^\dagger & h_{i,2}^\dagger \\ -h_{i,2} & h_{i,1} \end{bmatrix}\begin{bmatrix} \psi_{i,1} & \psi_{i,2}^\dagger \\ \psi_{i,2} & -\psi_{i,1}^\dagger \end{bmatrix} \tag{3.10}$$

provided the constraint that physical states are invariant under $SU(2)$ gauge transformations, namely $(\psi_i^\dagger \boldsymbol{\sigma}\psi_i + h_i^\dagger \boldsymbol{\sigma} h_i) = 0$, is enforced at every site.

After decoupling the resulting quartic terms the $SU(2)$ slave boson MF Hamiltonian is obtained

$$\begin{aligned} H_{sb}^{MF} = & \frac{3}{16}\sum_{\langle ij\rangle} J_{ij} Tr\left[U_{ij}U_{ji}\right] + \frac{1}{2}\sum_{\langle ij\rangle} t_{ij} Tr\left[U_{ij}V_{ji}\right] \\ & + \boldsymbol{a}_0 \cdot \left(\sum_i \psi_i^\dagger \boldsymbol{\sigma}\psi_i + h_i^\dagger \boldsymbol{\sigma} h_i\right) - \mu_h \sum_i h_i^\dagger h_i \\ & - \frac{1}{2}\sum_{\langle ij\rangle} t_{ij}\left(h_i^\dagger U_{ij} h_j + h.c.\right) \\ & - \sum_{\langle ij\rangle}\left[\psi_i^\dagger\left(\frac{3}{8}J_{ij}U_{ij} + \frac{1}{2}t_{ij}V_{ij}\right)\psi_j + h.c.\right] \end{aligned} \tag{3.11}$$

where μ_h is the holon chemical potential and $\boldsymbol{a}_0$, the Lagrange multiplier that enforces the $SU(2)$ projection constraint, is taken to be spatially uniform. In addition, new MF parameters $V_{ij} = \langle \widehat{V}_{ij}\rangle$ are introduced, where

$$\widehat{V}_{ij} = \begin{bmatrix} h_{j,1}^\dagger h_{i,1} - h_{i,2}^\dagger h_{j,2} & h_{i,2}^\dagger h_{j,1} + h_{j,2}^\dagger h_{i,1} \\ h_{i,1}^\dagger h_{j,2} + h_{j,1}^\dagger h_{i,2} & h_{j,2}^\dagger h_{i,2} - h_{i,1}^\dagger h_{j,1} \end{bmatrix} \tag{3.12}$$

[1]Recall the slave boson approach is inherently a low hole density approximation.

Despite ignoring gauge fluctuations, we expect MF theory to account for some qualitatively right features. Indeed, we have the following:

(i) The energetics of the model is correctly captured at MF level. This fact is suggested by the $SU(2)$ slave boson MF theory phase diagram for the tJ model – it includes the pseudogap regime (s-flux state) that turns into the dSC state as holons become coherent, as well as the strange-metal and Fermi-liquid regimes [57, 58]. In particular, the pseudogap metallic state was predicted by the slave boson approach prior to experimental observation [76];

(ii) The nature of fluctuations in each phase is also consistent with experiments. For instance, the $U(1)$ gauge structure in the s-flux state accounts for the spin excitation spectrum in underdoped HD materials [63]. In the strange-metal regime $SU(2)$ gauge fluctuations are responsible for the observed non-Fermi liquid behavior;

(iii) MF states have properties that survive projection even in the presence of long range $U(1)$ gauge fields. Take the s-flux state, which includes both staggered current and d-wave pairing fluctuations, as an example. Remarkably, in Ref. [82] staggered vorticity correlations were reported to emerge from Gutzwiller projecting the dSC wave function. There is also numerical evidence that Z_2 MF states lead to fractionalized phases after performing Gutzwiller projection [83].

3.3 Mean-field phase diagrams

To implement the self-consistent MF equations for the $tt'J$ model, the uniform d-wave ansatz for spinons (3.9) considered in Ref. [57, 58] must be extended to include the NNN MF parameters $U_{i,i+\hat{x}\pm\hat{y}}$. Here we only consider translation invariant ansatsë which do not break any symmetry. In our MF calculation we use the following ansatz which properly comprises both the s-flux and dSC states:

$$\begin{aligned} U_{i,i+\hat{x}} &= \chi\sigma_z + \Delta\sigma_x\,, \\ U_{i,i+\hat{y}} &= \chi\sigma_z - \Delta\sigma_x\,, \\ U_{i,i+\hat{x}\pm\hat{y}} &= \gamma\sigma_z\,, \\ \boldsymbol{a}_0 &= a_0\,. \end{aligned} \tag{3.13}$$

Depending on the values of χ, Δ, and γ, the above ansatz can describe phases with the same symmetry but different quantum orders [59]. These phases may contain $SU(2)$, $U(1)$, or Z_2 gauge fluctuations. Some phases display a large Fermi surface while others have only Fermi points. These different MF states and their labels are summarized in Table 3.1.

The MF phase diagrams are determined for $t = 3J$ and t' between $-1.5J$ and $1.5J$. These values are representative of the cuprates (note that t' is close to J for ED samples). Holons may condense at nonzero temperatures due to interactions or to the projection constraint (as proposed in Refs. [57, 58]). However, at MF level holons are free and *conventional* holon condensation only occurs at $T = 0$. In our calculations we take $T > 0$ and, hence, only consider the aforementioned *unconventional* mechanism.

The resulting (t', x) phase diagram for $T = 0^+$ is shown in Fig. 3-1(a). For

MF phase	Gauge structure	MF parameters		
s-flux (sf)	$U(1)$	$\chi \neq \Delta$	$\gamma = a_0 = \rho = 0$	$\chi, \Delta \neq 0$
Z2	Z_2	$\chi \neq \Delta$	$\chi, \Delta, \gamma, a_0 \neq 0$	$\rho = 0$
dSC	Z_1	$\chi \neq \Delta$	$\chi, \Delta, \gamma, a_0, \rho \neq 0$	
U1	$U(1)$	$\Delta = \rho = 0$	$\chi, \gamma, a_0 \neq 0$	
FL	Z_1	$\Delta = 0$	$\chi, \gamma, a_0, \rho \neq 0$	
uRVB	$SU(2)$	$\chi \neq 0$	$\Delta = \gamma = a_0 = \rho = 0$	
π-flux (πf)	$SU(2)$	$\chi = \Delta \neq 0$	$\gamma = a_0 = \rho = 0$	

Table 3.1: Labels for different MF phases. ρ is the density of condensed holons. All other parameters are defined in the main text

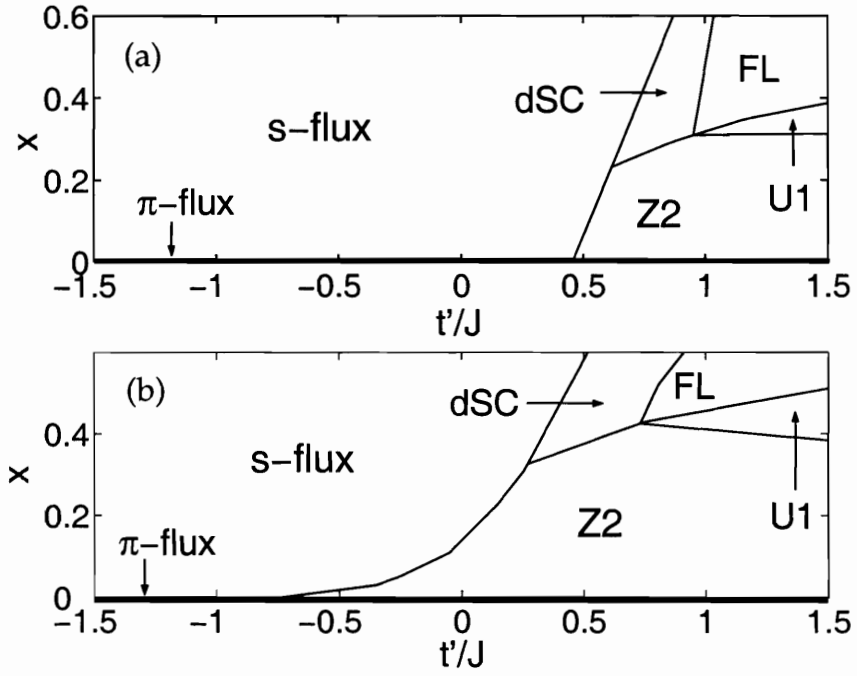

Figure 3-1: (a) (t', x) phase diagram for H_{MF} at $T = 0^+$. (b) (t', x) phase diagram at $T = 0^+$ after including H' and H''

$t' < 0.5J$ the s-flux state survives all the way to $T = 0^+$ – it becomes the dSC state at $T = 0$. However, for $t' > 0.5J$ new MF states are obtained. In the underdoped regime, where the $SU(2)$ theory was proposed to be relevant, the Z2 phase emerges. When $T = 0$ holons condense in the band bottom and the Z2 state changes into the dSC phase. For high enough doping we find the dSC state even at nonzero temperature – resulting from projection constraint driven condensation. As the pseudogap closes ($\Delta \rightarrow 0$) a state with $U(1)$ gauge structure and gapless spinons arises (U1). Upon holon condensation it becomes a Fermi liquid (FL).

For $t' < 0.5J$ we obtain the (x, T) phase diagram reported previously [57, 58]. The MF finite temperature phase diagrams are illustrated for $t' = 0.8J$ and $t' = 1.2J$ in Figs. 3-2(a) and 3-2(b) respectively. As, by construction, the AF phase is absent, the Z_2-linear state appears as the dominant phase at low doping. ED samples can have three different normal metallic states:
(i) a Z2 state with a d-wave pseudogap, true spin-charge separation and a nontrivial topological order [67, 68, 66];
(ii) a strange metal (the U1 phase) with a large Fermi surface and a $U(1)$ gauge interaction, and
(iii) a FL phase.

The above discussion of the MF phase diagrams is qualitatively correct even after including the H' term neglected in Sec. 3.2.2. In terms of spinons and holons, H' has the form

$$\begin{aligned} H' &= -\frac{J}{2}\sum_i (\Psi_i^\dagger \vec{\tau} \Psi_i)(h_i^\dagger \vec{\tau} h_i) \\ &\quad -\frac{J}{16}\sum_i \sum_{\hat{u}=\hat{x},\hat{y}} h_i^\dagger h_i h_{i+\hat{u}}^\dagger h_{i+\hat{u}} + O(x^3), \end{aligned} \tag{3.14}$$

(which is $\propto x^2$ at the MF level). While the second term correctly describes the attraction between holons resulting from the background with AF fluctuations, the first one should have the opposite sign to correctly account for the attraction between spinons and holons caused by gauge fluctuations. Hence, H' should be considered together with an effective contribution arising from the gauge interaction. At MF level the constraint is implemented only globally, *i.e.* $\langle \sum_i \vec{Q}_i \rangle = 0$. Including the following effective interaction,

$$H'' = \frac{3J}{16} \sum_{i,\hat{u}=\hat{x},\hat{y}} (\vec{Q}_i - \vec{Q}_{i+\hat{u}})^2 \tag{3.15}$$

the fluctuations of $(\vec{Q}_i)^2$ away from zero are reduced. The prefactor in H'' is such that the exchange constant is renormalized to $J_{eff} = 1.5J$ (note that Gutzwiller projection is known to increase the effective exchange constant [86]). H'' also makes holons more massive. Including H' and H'' at MF level extends the region where the Z2 state emerges [Fig. 3-1(b)]. Hence gauge fluctuations stabilize the Z2 phase. As expected, projection has a smaller effect in this phase.

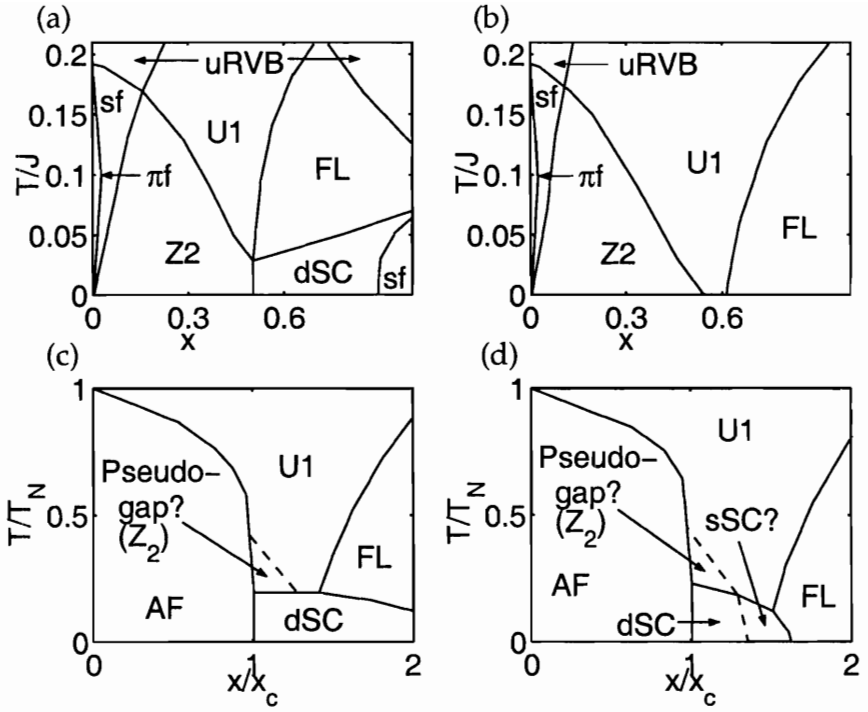

Figure 3-2: (x,T) MF phase diagrams for (a) $t' = 0.8J$ and (b) $t' = 1.2J$. In (c) and (d) *qualitative* phase diagrams, based on the MF results from (a) and (b) respectively, are proposed. These include the experimentally observed AF phase and finite temperature holon condensed phase due to holon interaction. The dashed line describes the transition into the Z2 state in case it is not completely absorbed by the AF phase. Above T_c the Z2 state describes pseudogap behavior. In (d) this transition may describe the reported transition from dSC to an extended s-wave SC (sSC) phase in $Pr_{2-x}Ce_xCuO_{4-y}$ and $La_{2-x}Ce_xCuO_{4-y}$ (Refs. [84, 85]).

The above results support that the Z_2-linear spin liquid introduced in Sec. 3.2 is a competitive state for higher values of t' and low doping levels. In particular, the lower bound $t' > 0.5J$ makes this state relevant for ED cuprates.

3.4 Spin-charge separation: the role of t'

The $SU(2)$ slave boson approach is designed to address the low doping regime. As it is clear from Fig. 3-1, for low doping there are two dominant phases, namely, the s-flux state and the Z2 state. The former becomes the latter as t' is increased above a certain critical value. This parameter driven transition links two states with the same symmetries (they both describe totally symmetric spin liquids). However they have different quantum orders [59]. This statement can be made more explicit by emphasizing the quite different nature of their low-energy effective behavior.

In the s-flux state massless Dirac fermions (spinons) and charged bosons (holons) interact with a long-range $U(1)$ gauge field. The gapless nature of these interacting excitations is protected by the quantum order [59]. Still, the gauge field has a drastic effect on the nature of the excitations – this state is in fact a manifestation of a two-dimensional Luttinger liquid [63, 87, 88] which has no well defined quasiparticles.

On the other hand, in the Z2 state the gauge interaction becomes short-ranged. Hence, the (linearly dispersing) spinons and holons are well defined quasiparticles. For that reason there is true spin-charge separation. The remnant discrete Z_2 gauge structure reflects the topological order of the state [68]. This topological order is related to the ground-state degeneracy of the system when it is embedded in a manifold with nontrivial topology. Such degenerate ground-states are locally similar but have different global (topological) properties.

The different gauge structure in the two states [$U(1)$ and Z_2] naturally gives rise to qualitatively distinct spectra for the collective modes. Indeed, the transition is accompanied by the opening of a gap in the fluctuations around the MF saddle-point [89].

Physically, the transition from the s-flux state to the Z2 state corresponds to the emergence of coherent diagonal (intra-sublattice) charge carrier hopping – *i.e.* $\langle c_i^\dagger c_{i+\hat{u}} + c_{i+\hat{u}}^\dagger c_i \rangle$, with $\hat{u} = \pm\hat{x} \pm \hat{y}$, becomes nonzero. It results from a combination of two factors: *(i)* increasing t' unfrustrates diagonal hopping and *(ii)* electron/hole intra-sublattice hopping is not frustrated and does not frustrate the background AF correlations (unlike inter-sublattice hopping). These play a crucial role in the dynamics of charge carriers (and of spin degrees of freedom as well).

In the s-flux state intra-sublattice hopping is depleted by the negative t'. As charge carriers hop between different sublattices they interact strongly with the background AF fluctuations. Hence charge carrier motion and AF correlations frustrate each other. That is the motive underlying the staggered current and staggered chiral spin correlations [90, 75]. The presence of such correlations in the context of the tJ model was reported in exact diagonalization studies [91]. Moreover, charge carrier density and vorticity correlations are proportional to each other [82, 91]. The emerging picture consists of charge carriers of opposite vorticity attracting each other in a

background of staggered chiral spin fluctuations. This attraction eventually induces dSC coherence.

In the Z2 state charge carriers hop coherently along the diagonals and the staggered current correlations decrease. In particular, the energy difference between the dSC and staggered current states is seen to increase with t'. Therefore, staggered current fluctuations are reduced in the Z2 state. Exact diagonalization studies in doped $tt'J$ ladders show the same trend – *i.e.* staggered currents are stabilized by decreasing t' [92]. According to our calculations, spinon pairing (Δ) is also reduced by the emergence of coherent diagonal hopping (therefore, charge carrier pairing may be expected to decrease as well). This is further consistent with the fact that the Z_2-vortex gap is physically connected to the reduction of staggered chiral spin fluctuations [89]. Interestingly, exact diagonalization calculations for the $tt'J$ on a 32-site lattice find no clear indication of a staggered pattern in both the current-current and vorticity correlations when t' is chosen to be relevant to ED cuprates [62]. The results in Ref. [62] additionally support that charge carrier binding is not favored in the ED regime, in agreement with our MF results and the interpretation that stems from the MF analysis[2].

Topological order in the Z2 state is associated with the intra-sublattice hopping parameter γ. Studies of Gutzwiller-projected wave functions in Ref. [83] further corroborate the importance of the NNN hopping term (*i.e.* a non-vanishing γ) in realizing true fractionalization. Consequently, for underdoped samples, the Z_2-vortex gap in this fractionalized metallic pseudogap phase is set by γ which is $\propto x$. This is qualitatively different from the suggestion of Senthil and Fisher where the Z_2-vortex gap is set by the pseudogap scale (Δ) [69, 70].

The above arguments support and delineate how the parameter t' induces spin-charge separation. However, to fit experimental band structure, an extra hopping term (t'') must be included [61, 96]. This requires an extension of the ansatsë considered in our analysis. Nevertheless, in a tight-binding model with $t > 0$, $t' > 0$ and $t'' < 0$ (as it is the case for ED cuprates), t'' is seen to frustrate hopping along the lattice bonds while unfrustrating hopping along the diagonals – in this sense enhancing the effect of t'.

[2]Results based on numerical calculations on ladder systems show that charge carrier binding is favored by an increasing t' (Refs. [92] and [93, 94]). The sensitiveness to the effective dimensionality of the system under analysis is reflected in Fig.12 of Ref. [95]. In particular, exact diagonalization studies on a two-dimensional system show the opposite trend with the change of t' [62]. In Ref. [93, 94] some qualitative arguments on small clusters were put forth to motivate the aforementioned ladder results. These differ from the picture we propose. In the present approach the pairing parameter Δ (which is not the superconducting order parameter obtained from the electron d-wave pair field correlation function) emerges in the spin sector due to the highly frustrated antiferromagnetic background with non-local correlations. As suggested above such pairing is enhanced by staggered chiral spin fluctuations. Our results support that increasing t' reduces these fluctuations and facilitates single charge carrier intra-sublattice hopping.

3.5 Application to electron doped cuprates

As mentioned before, in ED cuprates the AF state is very stable. Such stability can be addressed within the $tt'J$ model framework. Indeed, an increasing t' unfrustrates intra-sublattice hopping and renders the charge carriers less effective in frustrating the background AF correlations [60, 97]. However, our MF results suggest that, if AF order can be destroyed by tuning parameters in the Hamiltonian, the resulting spin liquid may contain a pseudogap and correspond to the Z2 state.

A distinctive experimental feature of the Z2 phase is the presence of a d-wave pseudogap[3]. Well, in the different $Nd_{2-x}Ce_xCuO_{4-y}$, $Pr_{2-x}Ce_xCuO_{4-y}$ (PCCO), and $La_{2-x}Ce_xCuO_{4-y}$ (LCCO) SC thin films, the SC gap ($\sim 5-10meV$) is reported to survive in the magnetic field driven normal state [71, 72, 73]. The value of the normal state gap is comparable to the SC gap and decreases with doping. Moreover, the low temperature normal state in PCCO SC crystals was reported to violate the Wiedemann-Franz law [41]. This provides evidence for a non-Fermi liquid state compatible with spin-charge separation. According to our MF results, the aforementioned normal state may realize the Z2 state. On the other hand, if the Z2 state is to exist above T_c it probably only covers a small fraction of the phase diagram due to the robust AF phase [Figs.3-2(c) and 3-2(d)][4].

Despite still disputed, there are a number of experiments reporting dSC order in ED samples [13]. In our picture, the $d_{x^2-y^2}$ gap in the SC phase is inherited from spinon pairing in the Z2 state. Recently, however, a SC pairing symmetry transition across optimal doping, from d-wave to extended s-wave, was reported in both LCCO and PCCO [84, 85]. We suggest the extended s-wave pairing may result in the FL state [Fig.3-2(d)] from exchange of collective modes – as the interaction between the Fermi sea and the massive gauge-fields raises an instability in the s-wave pairing channel [100]. We remark that this mechanism is unrelated to the one underlying dSC.

3.6 Conclusions

In this chapter we use a self-consistent $SU(2)$ slave boson approach to study the role of NNN hopping in the context of the $tt'J$ model. We find that t' induces a transition between the s-flux state (an algebraic spin liquid [63, 87]) and the Z2 state (a spin liquid with true spin-charge separation). This transition is interpreted as the emergence of coherent intra-sublattice hopping in the Z2 state. The parameter t' is also found to decrease staggered current and staggered chiral spin fluctuations, as well as to reduce pairing between charge carriers, in accordance with exact diagonalization results [62].

[3]There is a large gap, evolving from $\sim 400meV$ for $x = 0.04$ to $\sim 100meV$ for $x = 0.15$, in the stable AF phase in ED samples of $Nd_{2-x}Ce_xCuO_{4-y}$ according to angle-resolved photoemission spectroscopy [39] and optical conductivity [98] measurements. It results from a (π, π) scattering mechanism [99] and is not the pseudogap in the Z2 state.

[4]As noted above, in the absence of the Z2 pseudogap regime above T_c our MF results indicate that the normal state can be described by either a strange metal (U1 phase) or a Fermi liquid.

The range of parameters involved leads us to propose that a pseudogap metallic state in ED cuprates is likely to be described by a Z_2-linear phase. In contrast, the pseudogap state for HD samples is found to be described only by the s-flux phase with $U(1)$ gauge interaction.

Realizing fractionalized states in real systems is a major challenge. The present work suggests that the search for a pseudogap metallic state in ED cuprate samples may achieve such a goal.

Chapter 4

New formulation of the $tt't''J$ model and the "doped carrier" mean-field theory of cuprates

I'm frightened of eggs, worse than frightened, they revolt me. That white round thing without any holes...

Alfred Hitchcock

4.1 Introduction

The high-temperature superconducting (SC) cuprates are layered materials where the copper-oxide planes are separated by several elements whose chemistry controls the density of carriers in the CuO_2 layers. Due to the localized character of $3d$ orbitals, copper valence electrons feel a large Coulomb interaction which drives strong correlations [26]. The largest in-plane energy scale is the local Coulomb repulsion U, measured to be $\approx$ 2eV [101], thus motivating the use of the generalized-tJ model in the context of cuprate phenomenology [26, 32].

Upon inclusion of the parameters t' and t'' the generalized-tJ model reproduces many spectral features observed in both hole and electron doped cuprates [46, 48] and, in particular, is consistent [44, 45, 102] with the large experimental body supporting the momentum space anisotropy of excitations (for a discussion on experimental evidence in favor of such an anisotropy in underdoped materials see Refs. [102, 31, 36, 103] and Chapters 2 and 5 of this thesis). Therefore we consider the two-dimensional $tt't''J$ Hamiltonian

$$H_{tJ} = J \sum_{\langle ij \rangle \in NN} \left(\boldsymbol{S}_i . \boldsymbol{S}_j - \frac{1}{4} n_i n_j \right) - \sum_{\langle ij \rangle} t_{ij} \mathcal{P} \left(c_i^\dagger c_j + c_j^\dagger c_i \right) \mathcal{P} \tag{4.1}$$

where $t_{ij} = t, t', t''$ for first, second and third nearest neighbor (NN) sites respectively. $c_i^\dagger = [c_{i,\uparrow}^\dagger c_{i,\downarrow}]$ is the electron creation spinor operator, $n_i = c_i^\dagger c_i$ and $\boldsymbol{S}_i = c_i^\dagger \boldsymbol{\sigma} c_i$ are the electron number and spin operators, $\boldsymbol{\sigma}$ are the Pauli matrices and $\mathcal{P}$ projects

out doubly occupied sites. As a result of the no double occupancy constraint, the $tt't''J$ model Hilbert space consists of states where every site has either a spin-1/2 or a vacancy.

The major hurdle to handle the $tt't''J$ model analytically stems from the highly constrained nature of the projected electron operators. Close to half-filling the operator $\mathcal{P}c_i^\dagger\mathcal{P}$ in the hopping sector of (4.1) differs significantly from the bare electron operator $c_i^\dagger$. In fact, right at half-filling $\mathcal{P}c_i^\dagger\mathcal{P} = 0$ and the system is an insulator. In the Gutzwiller approximation [86, 104] the reduction of the hole kinetic energy, as well as any other one electron energy terms [105], due to the projected nature of the Hilbert space is implemented by eliminating the projection operators $\mathcal{P}$ and introducing a renormalization factor $g_t = \frac{2x}{1+x}$ which vanishes in the half-filling limit. Even though this approach performs well in terms of the energetics, which compares favorably with Monte Carlo projection results, it misses the important fact that the dynamics of vacancies in strongly correlated systems depends crucially on the background spin correlations. We further elaborate on this aspect in Chapters 5 to 7 where we discuss the electron spectral function and the tunneling conductance spectrum of strongly correlated superconductors [106, 103].

Conventional band materials are suitably described both in terms of electron or hole operators. In the context of semiconductor physics it is often convenient to describe doped conduction bands in terms of electrons and doped valence bands in terms of holes [107]. Here, we propose a similar rule of thumb might also apply to doped Mott insulators. Of course, band and Mott insulators are different and, therefore, the physical properties of holes doped into band or Mott insulators are distinct as well. Indeed, in the former case, the doped hole corresponds to a site with charge e and spin $\pm\frac{1}{2}$. This is in contrast with a hole inserted in a Mott insulator, which corresponds to the removal of a lattice spin. This process leaves a unit charge e on the vacant site. The extra spin $\pm\frac{1}{2}$, however, is not on the same site, which is a spin singlet, and is carried by the surrounding spin background instead. Hence, strictly speaking, the hole doped into a Mott insulator is not an on-site entity with charge e and spin $\pm\frac{1}{2}$.

In Sec. 4.2 of this chapter we derive a new formulation of the $tt't''J$ model in terms of doped holes. In this formulation doped holes are on-site operators with the same charge and spin as conventional holes. This is achieved by enlarging the $tt't''J$ model Hilbert and leaving out the contribution from the extra, unphysical, states. Physically, these hole operators describe the non-local entities consisting of the vacancy and the extra spin $\pm\frac{1}{2}$ carried by the encircling spins. Two rewarding advantages of this formulation are: *(i)* we explicitly use hole operators in the hopping sector of (4.1) and, since close to half-filling the hole density is small, we are free of the "no double occupancy" problem; *(ii)* reflecting the fact that holes are not true on-site objects the aforementioned hole operator encloses information about the local spin background and, therefore, we are able to capture the interplay between charge dynamics and different spin correlations even at mean-field (MF) level.

In the remainder of the chapter we use the above formulation of the $tt't''J$ model as a starting point to derive a new MF theory (Sec. 4.3) whose relevance to the cuprate compounds is attested by comparing the MF phase diagram to that of hole

and electron doped materials (Sec. 4.4). We also clarify the role played by the hopping parameters t, t' and t'' in determining the robustness of different phases and, in Sec. 4.5, we present our conclusions.

4.2 Doped carrier formulation of the $tt't''J$ model

Before proceeding further, we remark that the $tt't''J$ model can be used to describe both the lower Hubbard band or the upper Hubbard band. In the former case, doped carriers are holes and the operator $c_i^\dagger$ creates an electron. However, in the latter case, doped carriers are electrons and the operator $c_i^\dagger$ creates a hole instead. Above, we have exclusively used the terminology appropriate for the lower Hubbard band. Since in this chapter we want to address both hole and electron doped regimes of the cuprates, from this point on we generally refer to doped carriers instead of specifying whether these are physical holes or physical electrons.

4.2.1 Enlarged Hilbert space

The $tt't''J$ model on-site Hilbert space includes states with either one or zero spin-$\frac{1}{2}$ objects: $\{|\uparrow\rangle, |\downarrow\rangle, |0\rangle\}$ standing for up spin, down spin and vacancy respectively. In order to introduce a local doped carrier operator with both unit electric charge and spin-$\frac{1}{2}$ we consider the enlarged on-site Hilbert space

$$\{|\uparrow 0\rangle, |\downarrow 0\rangle, \frac{|\uparrow\downarrow\rangle - |\downarrow\uparrow\rangle}{\sqrt{2}}, \frac{|\uparrow\downarrow\rangle + |\downarrow\uparrow\rangle}{\sqrt{2}}, |\uparrow\uparrow\rangle, |\downarrow\downarrow\rangle\} \tag{4.2}$$

which contains either one or two spin-$\frac{1}{2}$ objects. The first three states in (4.2) are the physical states that map onto the states $|\uparrow\rangle$, $|\downarrow\rangle$ and $|0\rangle$, respectively, in the $tt't''J$ model on-site Hilbert space. The on-site triplet states, *i.e.* the last three states in (4.2), are unphysical as they do not pertain to the $tt't''J$ model on-site Hilbert space.

To represent states in (4.2) we introduce the spin operator $\widetilde{\boldsymbol{S}}_i$ that labels the state of the first spin and the fermionic operator $d_i^\dagger = [d_{i,\uparrow}^\dagger d_{i,\downarrow}^\dagger]$ that labels the state of the second spin. We remark that there is one $\widetilde{\boldsymbol{S}}_i$ spin in every site, which we thus call lattice spin, and one d-fermion in all the sites that correspond to a physical vacancy. Hence, the number of d-fermions equals the number of doped carriers. In fact, d-fermions have the same electric charge and spin as the carriers inserted in the system and, therefore, describe these doped carriers. For ease of speaking, below we refer to these spin-1/2 charged fermions as *dopons*. In terms of the above operators, states in the enlarged on-site Hilbert space are written as $\left|\widetilde{\boldsymbol{S}}_i, \frac{1}{2}\widetilde{\mathcal{P}} d_i^\dagger \boldsymbol{\sigma} d_i \widetilde{\mathcal{P}}\right\rangle$. Note that in (4.2) there exist no states with two dopons on the same site. Hence, we introduce the projection operator $\widetilde{\mathcal{P}} = \prod_i (1 - d_{i,\uparrow}^\dagger d_{i,\uparrow} d_{i,\downarrow}^\dagger d_{i,\downarrow})$ which enforces the no double occupancy constraint for dopons.

4.2.2 Heisenberg term

The next step is to write the $tt't''J$ model Hamiltonian (4.1) in the enlarged Hilbert space. The resulting Hamiltonian

$$H_{tJ}^{enl} = H_{enl}^{J} + H_{enl}^{t} \tag{4.3}$$

is the sum of the Heisenberg (H_{enl}^{J}) and the vacancy hopping (H_{enl}^{t}) terms. We first consider the former one.

In the absence of a dopon on site i the local spin $\boldsymbol{S}_i = \widetilde{\boldsymbol{S}}_i$ and $n_i = 1$. Both these quantities vanish otherwise. Therefore, $\boldsymbol{S}_i = \widetilde{\boldsymbol{S}}_i \widetilde{\mathcal{P}} \left(1 - d_i^{\dagger} d_i\right) \widetilde{\mathcal{P}}$, $n_i = \widetilde{\mathcal{P}} \left(1 - d_i^{\dagger} d_i\right) \widetilde{\mathcal{P}}$ so that the Heisenberg term becomes

$$H_{enl}^{J} = J \sum_{\langle ij \rangle \in NN} \left(\widetilde{\boldsymbol{S}}_i . \widetilde{\boldsymbol{S}}_j - \frac{1}{4} \right) \widetilde{\mathcal{P}} \left(1 - d_i^{\dagger} d_i\right) \left(1 - d_j^{\dagger} d_j\right) \widetilde{\mathcal{P}} \tag{4.4}$$

4.2.3 Hopping term

The hopping term in the $tt't''J$ model Hamiltonian (4.1) has a matrix element t_{ij} connecting a state with a vacancy on site j and a spin on site i to that with an equal spin state on site j and a vacancy on site i. This is a two site process that leaves the remaining sites unaltered and, schematically, it amounts to

$$\begin{aligned} |0;\uparrow\rangle &\rightarrow |\uparrow;0\rangle \\ |0;\downarrow\rangle &\rightarrow |\downarrow;0\rangle \end{aligned} \tag{4.5}$$

where the notation $|j;i\rangle$ is used to represent the states on sites j and i.

Using the corresponding notation for the enlarged Hilbert space, namely

$$\left| \widetilde{\boldsymbol{S}}_j, \tfrac{1}{2} \widetilde{\mathcal{P}} d_j^{\dagger} \boldsymbol{\sigma} d_j \widetilde{\mathcal{P}} \, ; \, \widetilde{\boldsymbol{S}}_i, \tfrac{1}{2} \widetilde{\mathcal{P}} d_i^{\dagger} \boldsymbol{\sigma} d_i \widetilde{\mathcal{P}} \right\rangle \tag{4.6}$$

the processes described in (4.5) are

$$\begin{aligned} \left| \frac{\uparrow\downarrow - \downarrow\uparrow}{\sqrt{2}} ; \uparrow 0 \right\rangle &\rightarrow \left| \uparrow 0 ; \frac{\uparrow\downarrow - \downarrow\uparrow}{\sqrt{2}} \right\rangle \\ \left| \frac{\uparrow\downarrow - \downarrow\uparrow}{\sqrt{2}} ; \downarrow 0 \right\rangle &\rightarrow \left| \downarrow 0 ; \frac{\uparrow\downarrow - \downarrow\uparrow}{\sqrt{2}} \right\rangle \end{aligned} \tag{4.7}$$

All other processes that move a dopon from site j to site i have a vanishing matrix element. The matrix representation for these hopping terms in the above two site

notation is

$$\begin{bmatrix} 0 & 0 & 0 & 0 & 0 & 0 & 0 & 0 \\ 0 & \frac{t_{ij}}{2} & 0 & 0 & -\frac{t_{ij}}{2} & 0 & 0 & 0 \\ 0 & -\frac{t_{ij}}{2} & 0 & 0 & \frac{t_{ij}}{2} & 0 & 0 & 0 \\ 0 & 0 & 0 & 0 & 0 & 0 & 0 & 0 \\ 0 & 0 & 0 & 0 & 0 & 0 & 0 & 0 \\ 0 & 0 & 0 & \frac{t_{ij}}{2} & 0 & 0 & -\frac{t_{ij}}{2} & 0 \\ 0 & 0 & 0 & -\frac{t_{ij}}{2} & 0 & 0 & \frac{t_{ij}}{2} & 0 \\ 0 & 0 & 0 & 0 & 0 & 0 & 0 & 0 \end{bmatrix} \tag{4.8}$$

where columns correspond to states $|\uparrow\uparrow;\uparrow 0\rangle$, $|\uparrow\downarrow;\uparrow 0\rangle$, $|\uparrow\uparrow;\downarrow 0\rangle$, $|\uparrow\downarrow;\downarrow 0\rangle$, $|\downarrow\uparrow;\uparrow 0\rangle$, $|\downarrow\downarrow;\uparrow 0\rangle$, $|\downarrow\uparrow;\downarrow 0\rangle$ $|\downarrow\downarrow;\downarrow 0\rangle$ respectively and rows to states $|\uparrow 0;\uparrow\uparrow\rangle$, $|\uparrow 0;\uparrow\downarrow\rangle$, $|\uparrow 0;\downarrow\uparrow\rangle$, $|\uparrow 0;\downarrow\downarrow\rangle$, $|\downarrow 0;\uparrow\uparrow\rangle$, $|\downarrow 0;\uparrow\downarrow\rangle$, $|\downarrow 0;\uparrow\downarrow\rangle$, $|\downarrow 0;\downarrow\uparrow\rangle$, $|\downarrow 0;\downarrow\uparrow\rangle$, $|\downarrow 0;\downarrow\downarrow\rangle$ respectively. As we change from particle hopping $c^{\dagger}_{j,\alpha}c_{i,\beta}$ in the initial formulation of the $tt't''J$ model (4.1) to doped carrier hopping $d^{\dagger}_{i,\alpha}d_{j,\beta}$ in the new formulation of the same model, an extra $(-)$ sign appears in the hopping term. This sign is included in the matrix elements of (4.8).

In Appendix 4.6 the matrix (4.8) is written in terms of lattice spin operators $\widetilde{\boldsymbol{S}}_i$ and $\widetilde{\boldsymbol{S}}_j$ and dopon operators $d^{\dagger}_i$ and d_j. As a result, the hopping term in the enlarged Hilbert space is derived to be

$$\begin{aligned} H^t_{enl} \;=\; \sum_{\langle ij\rangle} \frac{t_{ij}}{2}\widetilde{\mathcal{P}} \Bigg[\left(d^{\dagger}_i \boldsymbol{\sigma} d_j\right) . \left(i\widetilde{\boldsymbol{S}}_i \times \widetilde{\boldsymbol{S}}_j - \frac{\widetilde{\boldsymbol{S}}_i + \widetilde{\boldsymbol{S}}_j}{2} \right) + \\ + \frac{1}{4} d^{\dagger}_i d_j + d^{\dagger}_i d_j \widetilde{\boldsymbol{S}}_i . \widetilde{\boldsymbol{S}}_j + h.c. \Bigg] \widetilde{\mathcal{P}} \end{aligned} \tag{4.9}$$

Overall, the $tt't''J$ Hamiltonian in the enlarged Hilbert space (4.3) equals H_{tJ} in the physical Hilbert space. In addition, it does not connect the physical and the unphysical sectors of the enlarged Hilbert space. Following the specific construction of the hopping matrix (4.8), which vanishes for all processes but the ones in (4.7), H^t_{enl} is such that only local singlet states hop between different lattice sites whereas the unphysical local triplet states are localized and have no kinetic energy. Therefore, *the dynamics enclosed in H^t_{enl} effectively implements the local singlet constraint.*

We emphasize that the above "doped carrier" formulation of the $tt't''J$ model, as expressed in Equations (4.3), (4.4) and (4.9), is equivalent to the original "particle" formulation encoded in (4.1). Interestingly, it provides a different starting point to deal with doped spin models.

In the low doping regime the dopon density $x = \frac{1}{N}\sum_i \widetilde{\mathcal{P}} d^{\dagger}_i d_i \widetilde{\mathcal{P}}$ is small and the no double occupancy constraint is safely relaxed. Hence, below we drop all the projection operators $\widetilde{\mathcal{P}}$. We thus propose that the dramatic effect of the projection operators $\mathcal{P}$ in the "particle" formulation of the $tt't''J$ model (4.1) is captured by the dopon-spin interaction in the hopping hamiltonian (4.9), which explicit accounts for the role of local spin correlations on the hole dynamics. In the remainder of the chapter we derive and discuss a MF theory that describes this interaction.

4.3 Doped carrier mean-field theory of the $tt't''J$ model

4.3.1 Heisenberg term

To derive a MF theory of the $tt't''J$ model "doped carrier" formulation we chose to use the fermionic representation of the lattice spins [74] $\widetilde{\boldsymbol{S}}_i = \frac{1}{2} f_i^\dagger \boldsymbol{\sigma} f_i$, where $f_i^\dagger = [f_{i,\uparrow}^\dagger f_{i,\downarrow}^\dagger]$ are spinon operators like the ones introduced in Sec. 3.2.1. In this representation, the $SU(2)$ projection constraint enforcing $f_i^\dagger f_i = 1$ at every site must be added to (4.3) [57, 59]. The Hamiltonian H_{tJ}^{enl} is then the sum of terms with multiple-fermionic operators, which we replace by their average so that the resulting MF Hamiltonian is quadratic in the operators $f^\dagger$, f, $d^\dagger$ and d, and describes the hopping, pairing and mixing of spinons and dopons. We remark that, in contrast to the slave boson approach, the resulting MF Hamiltonian is purely fermionic.

We first implement such a decoupling procedure to the spin exchange interaction (4.4). After replacing the operator $\widetilde{\mathcal{P}}\left(1 - d_i^\dagger d_i\right)\widetilde{\mathcal{P}}$ by its average value $(1-x)$, the Hamiltonian (4.4) reduces to the Heisenberg Hamiltonian (3.2) with the renormalized exchange constant $\widetilde{J} = (1-x)^2 J$. We then use the d-wave ansatz (3.9) to decouple the quartic fermionic terms and obtain the MF Hamiltonian (3.8) derived in Sec. 3.2.1 [57, 58]. In terms of the f-spinon operators, the d-wave pairing structure of the spinon sector is explicit

$$-\frac{3\widetilde{J}}{8} \sum_{\langle ij \rangle \in NN} \left[\chi f_i^\dagger f_j + (-)^{j_y - i_y} \Delta \left(f_{i\uparrow}^\dagger f_{j\downarrow}^\dagger - f_{i\downarrow}^\dagger f_{j\uparrow}^\dagger \right) + h.c. \right] + a_0 \sum_i (f_i^\dagger f_i - 1) \quad (4.10)$$

4.3.2 Hopping term

We now consider the hopping Hamiltonian (4.9), which describes the hopping of holes on top of a spin background with strong local antiferromagnetic (AF) correlations. It is well understood that, under such circumstances, the hole dispersion is renormalized by spin fluctuations [30, 108]. As it is further elaborated in Sec. 4.3.4, at MF level we capture the result of this renormalization by replacing the bare t, t' and t'' by effective hopping parameters t_1, t_2 and t_3 which are determined phenomenologically.

The hopping term (4.9) involves both spinon and dopon operators. Following the steps outlined in Sec. 3.2, we introduce the $SU(2)$ matrix representation of dopon operators

$$D_i = \begin{bmatrix} d_{i,\uparrow} & d_{i,\downarrow} \\ d_{i,\downarrow}^\dagger & -d_{i,\uparrow}^\dagger \end{bmatrix} \quad (4.11)$$

and of spinon operators (3.5). We also introduce the operators

$$\hat{B}_{ij} = D_j \Psi_i^\dagger = \begin{bmatrix} d_{j,\uparrow}\psi_{i,1}^\dagger + d_{j,\downarrow}\psi_{i,2} & d_{j,\uparrow}\psi_{i,2}^\dagger - d_{j,\downarrow}\psi_{i,1} \\ d_{j,\downarrow}^\dagger \psi_{i,1}^\dagger - d_{j,\uparrow}^\dagger \psi_{i,2} & d_{j,\downarrow}^\dagger \psi_{i,2}^\dagger + d_{j,\uparrow}^\dagger \psi_{i,1} \end{bmatrix} \quad (4.12)$$

which are electrically charged spin singlets and transform with the same $SU(2)$ gauge transformation as Ψ_i. Thus, they have the same quantum numbers as holons and we name them generalized holon operators. The resulting $SU(2)$ matrix representation of the hopping Hamiltonian (4.9) is

$$\sum_{\langle ij\rangle} \frac{t_{ij}}{8} \left\{ Tr\left[\left(\Psi_j^\dagger \Psi_j - I \right) D_j^\dagger \sigma_z D_i \left(\Psi_i^\dagger \Psi_i - I \right) \right] + \right.$$
$$\left. + Tr\left[D_i \Psi_i^\dagger \Psi_i D_j^\dagger \right] + Tr\left[D_j \Psi_j^\dagger \Psi_j D_i^\dagger \right] + Tr\left[D_j^\dagger \sigma_z D_i \right] \right\} \tag{4.13}$$

The first term in (4.13) corresponds to the $[(d_i^\dagger \boldsymbol{\sigma} d_j).(i\boldsymbol{S}_i \times \boldsymbol{S}_j)]$ and $(d_i^\dagger d_j \boldsymbol{S}_i.\boldsymbol{S}_j)$ terms in H_{enl}^t. This term has six fermionic operators and, thus, differs from the quartic fermionic terms conventionally decoupled by schemes like the Hartree-Fock approximation or the Hubbard-Stratanovich transformation. The approximation scheme followed below has to be discussed in some detail in order to understand the physical picture captured by the resulting approach.

The contribution from (4.13) to the MF spinon hopping arises from introducing the average

$$\langle \Psi_j D_j^\dagger \sigma_z D_i \Psi_i^\dagger \rangle = \langle \hat{B}_{jj}^\dagger \sigma_z \hat{B}_{ii} \rangle \approx x \sigma_z \delta_{\langle ij\rangle \in NN} \tag{4.14}$$

which yields the term

$$\sum_{\langle ij\rangle \in NN} \frac{t_1 x}{4} \left(f_i^\dagger f_j + f_j^\dagger f_i \right) \tag{4.15}$$

This term is also present, albeit with a different prefactor, in the $SU(2)$ slave boson MF Hamiltonian (3.11), and determines the effect of holons in the magnitude of the spinon d-wave pairing gap. The result in (4.14) assumes the temperature is low enough that the magnitude of the $\hat{B}_{ii}$ field is $\sim \sqrt{x}$. This approximation is expected to be correct between zero temperature and a certain temperature below the MF d-wave superconducting (dSC) transition temperature (which as discussed in Sec. 4.4 is above the true T_c for long-range dSC phase coherence).

The contribution from (4.13) to the MF dopon hopping comes, instead, from taking the average

$$\begin{aligned} \langle \left(\Psi_i^\dagger \Psi_i - I \right) \left(\Psi_j^\dagger \Psi_j - I \right) \rangle &= 4 \langle \widetilde{\boldsymbol{S}}_i.\boldsymbol{\sigma}\, \widetilde{\boldsymbol{S}}_j.\boldsymbol{\sigma} \rangle \\ &= 4 \langle \widetilde{\boldsymbol{S}}_i.\widetilde{\boldsymbol{S}}_j + i\boldsymbol{\sigma}.\left(\widetilde{\boldsymbol{S}}_i \times \widetilde{\boldsymbol{S}}_j \right) \rangle \\ &\approx (-1)^{j_x + j_y - i_x - i_y} \end{aligned} \tag{4.16}$$

Close to the Mott insulating limit the spin background is characterized by the presence of *local* AF correlations and, thus, the vacancy in the quasiparticle state is surrounded by an AF-like configuration of spins [102] (see Chapter 2). To approximately account for this effect we assume the spins encircling the vacancy in the one-dopon state are in a *local* Néel configuration. Therefore, in (4.16) we use $\langle \widetilde{\boldsymbol{S}}_i \times \widetilde{\boldsymbol{S}}_j \rangle = 0$ and $4\langle \widetilde{\boldsymbol{S}}_i.\widetilde{\boldsymbol{S}}_j \rangle = (-1)^{j_x + j_y - i_x - i_y}$. As a result, the contribution from the first and fourth

terms in (4.13) to the MF dopon sector is

$$\sum_{\langle ij\rangle\in 2^{nd}NN}\frac{t_2}{4}\left(d_i^\dagger d_j+d_j^\dagger d_i\right)+\sum_{\langle ij\rangle\in 3^{rd}NN}\frac{t_3}{4}\left(d_i^\dagger d_j+d_j^\dagger d_i\right) \tag{4.17}$$

Hence, the approximation used in (4.16) captures the fact that, due to the local correlations of the spin background close to the AF insulator phase, coherent NN hole hopping is strongly suppressed [30, 108]. Ideally, the average in (4.16) should be calculated self-consistently to reproduce the doping induced change in the local spin correlations. In the present MF scheme this is not performed and, instead, we introduce doping dependent effective hopping parameters t_2 and t_3 (see Sec. 4.3.4 and Sec. 7.4).

The dopon-spin interaction is enclosed in the second and third terms of (4.13), which can be recast as

$$\sum_{\langle ij\rangle}\frac{t_{ij}}{8}Tr\left[\hat{B}_{ii}\hat{B}_{ij}^\dagger+\hat{B}_{jj}\hat{B}_{ji}^\dagger\right] \tag{4.18}$$

In the Hartree-Fock-Bogoliubov approximation the above quartic term becomes

$$\begin{aligned}-\sum_{\langle ij\rangle}\frac{3t_{ij}}{16}\Big\{&Tr\left[B_{ii}B_{ij}^\dagger+B_{jj}B_{ji}^\dagger\right]+\\&+\left(\eta_i^\dagger B_{ij}\psi_i+\eta_j^\dagger B_{ii}\psi_i+\eta_j^\dagger B_{ji}\psi_j+\eta_i^\dagger B_{jj}\psi_j+h.c.\right)\Big\}\end{aligned} \tag{4.19}$$

where the MFs $B_{ij}=\langle\hat{B}_{ij}\rangle$ and the dopon Nambu operators $\eta_i^\dagger\equiv[\eta_{i1}^\dagger\eta_{i2}^\dagger]\equiv[d_{i\uparrow}^\dagger d_{i\downarrow}]$ are introduced.

Different choices for the mean-fields B_{ij} may describe distinct MF phases. Since we are interested in the properties of SC cuprate materials and given that, from slave boson MF theory, we know that d-wave superconductivity is energetically favored over states like the staggered-flux phase [57, 58], we use the MF ansatz

$$\begin{aligned}B_{ii}&=-b_0\sigma_z\\\left(\frac{3}{16}\sum_\nu t_\nu\sum_{\hat{u}\in\nu\,NN}B_{ii+\hat{u}}\right)&=-b_1\sigma_z\end{aligned} \tag{4.20}$$

where $\hat{u}=\pm\hat{x},\pm\hat{y}$, $\hat{u}=\pm\hat{x}\pm\hat{y}$ and $\hat{u}=\pm2\hat{x},\pm2\hat{y}$ for $\nu=1,2,3$ respectively. The resulting MF spinon-dopon interaction is

$$\sum_i\left(b_1d_i^\dagger f_i+\frac{3b_0}{16}\sum_\nu t_\nu\sum_{\hat{u}\in\nu\,NN}d_{i+\hat{u}}^\dagger f_i+h.c.\right) \tag{4.21}$$

This interaction describes the hybridization of dopons and spinons that occurs as a means to enhance dopon hopping processes which are frustrated by the underlying AF correlations. In particular, (4.21) provides the only mechanism for dopons to hop between different sublattices, since the dopon hopping term (4.17) prevents such

processes. From (4.20) we have that $b_0 = \langle f_i^\dagger d_i \rangle$ and $b_1 = \langle \frac{3}{16} \sum_\nu t_\nu \sum_{\hat{u} \in \nu\, NN} f_i^\dagger d_{i+\hat{u}} \rangle$ are the local and non-local MF parameters that emerge from such spin assisted hole hopping events and which describe the hybridization of spinons and dopons. In the rest of the chapter we interchangeably refer to the condensation of the bosonic mean-fields b_0 and b_1 as the coherent spinon-dopon hybridization, mixing or pairing. As a final remark, note that for $b_1 \neq 0$ the term $\sim b_1 d_i^\dagger f_i$ in (4.21) drives local mixing of spinons and holons and leads to a non-zero b_0. Similarly, if $b_0 \neq 0$ the term $\sim b_0 d_{i+\hat{u}}^\dagger f_i$ leads to non-local spinon-dopon mixing and, thus, to non-zero b_1. Hence, either b_0 and b_1 are both zero or both non-zero.

4.3.3 Mean-field Hamiltonian

Putting the terms (4.10), (4.15), (4.17) and (4.21) together leads to the full "doped carrier" MF Hamiltonian, which in momentum space and using the Nambu notation becomes

$$H_{tJ}^{MF} = \sum_{\boldsymbol{k}} \begin{bmatrix} \psi_{\boldsymbol{k}}^\dagger & \eta_{\boldsymbol{k}}^\dagger \end{bmatrix} \begin{bmatrix} \alpha_{\boldsymbol{k}}^z \sigma_z + \alpha_{\boldsymbol{k}}^x \sigma_x & \beta_{\boldsymbol{k}} \sigma_z \\ \beta_{\boldsymbol{k}} \sigma_z & \gamma_{\boldsymbol{k}} \sigma_z \end{bmatrix} \begin{bmatrix} \psi_{\boldsymbol{k}} \\ \eta_{\boldsymbol{k}} \end{bmatrix} + \\ + \frac{3\widetilde{J}N}{4}(\chi^2 + \Delta^2) - 2Nb_0 b_1 - N\mu_d \tag{4.22}$$

where

$$\alpha_{\boldsymbol{k}}^z = -\left(\frac{3\widetilde{J}}{4}\chi - \frac{t_1 x}{2}\right)(\cos k_x + \cos k_y) + a_0$$

$$\alpha_{\boldsymbol{k}}^x = -\frac{3\widetilde{J}}{4}\Delta\,(\cos k_x - \cos k_y)$$

$$\beta_{\boldsymbol{k}} = \frac{3b_0}{8}\left[t_1\,(\cos k_x + \cos k_y) + 2t_2 \cos k_x \cos k_y + \right. \\ \left. + t_3\,(\cos 2k_x + \cos 2k_y)\right] + b_1$$

$$\gamma_{\boldsymbol{k}} = t_2 \cos k_x \cos k_y + \frac{t_3}{2}\,(\cos 2k_x + \cos 2k_y) - \mu_d \tag{4.23}$$

In (4.22) N stands for the lattice size and we introduce the dopon chemical potential μ_d that sets the doping level $\left\langle d_i^\dagger d_i \right\rangle = x$.

The "doped carrier" MF theory of the $tt't''J$ model has two different spin-$\frac{1}{2}$ fermions and, thus, four fermionic bands described by the eigenenergies of H_{tJ}^{MF}, namely

$$\epsilon_{1,\boldsymbol{k}}^{\pm} = \pm\sqrt{\rho_{\boldsymbol{k}} - \sqrt{\delta_{\boldsymbol{k}}}}$$

$$\epsilon_{2,\boldsymbol{k}}^{\pm} = \pm\sqrt{\rho_{\boldsymbol{k}} + \sqrt{\delta_{\boldsymbol{k}}}} \tag{4.24}$$

where

$$\delta_{\boldsymbol{k}} = \beta_{\boldsymbol{k}}^2 \left[(\gamma_{\boldsymbol{k}} + \alpha_{\boldsymbol{k}}^z)^2 + (\alpha_{\boldsymbol{k}}^x)^2 \right] + \frac{1}{4} \left[\gamma_{\boldsymbol{k}}^2 - (\alpha_{\boldsymbol{k}}^x)^2 - (\alpha_{\boldsymbol{k}}^z)^2 \right]^2$$

$$\rho_{\boldsymbol{k}} = \beta_{\boldsymbol{k}}^2 + \frac{1}{2} \left[\gamma_{\boldsymbol{k}}^2 + (\alpha_{\boldsymbol{k}}^x)^2 + (\alpha_{\boldsymbol{k}}^z)^2 \right] \tag{4.25}$$

From (4.24) we conclude the energy spectrum is symmetric around zero energy. The lowest energy bands (the ones closer to zero energy) are $\epsilon_{1,\boldsymbol{k}}^{\pm}$ and correspond to a d-wave-like dispersion with nodal points along the $(0,0)-(\pm\pi,\pm\pi)$ directions. When $b_0 = b_1 = 0$ spinons and dopons do not mix and $\epsilon_{1,\boldsymbol{k}}^{\pm}$ comes from the spinon sector of H_{tJ}^{MF} and describes the same spin dynamics as slave boson theory [63]. The highest energy bands (the ones further from zero energy) are $\epsilon_{2,\boldsymbol{k}}^{\pm}$ and, in the absence of spinon-dopon hybridization, only include intra-sublattice hopping processes [Expression (4.17)], as appropriate in the one-hole limit of the $tt't''J$ model [109, 110, 108]. For $b_0, b_1 \neq 0$ the hole and spin degrees of freedom mix and provide an effective multi-band description of the interplay between spin and local charge dynamics. The generic dispersion of these MF bands is displayed in Fig. 5-3(a) in Chapter 5 and in Fig. 6-2(b) in Chapter 6.

4.3.4 Renormalized hopping parameters

In Sec. 4.3.2 we mention that at MF level we do not use the bare hopping parameters t, t' and t'' and instead resort to effective parameters t_1, t_2 and t_3. To motivate this procedure consider the single hole problem of the $tt't''J$ model with $t' = t'' = 0$. In this case the hole disperses along $(0,0)-(\pi,\pi)$ but disperses far less between $(0,\pi)-(\pi,0)$ [46, 30, 61]. The dispersion along $(0,0)-(\pi,\pi)$ peaks at $(\frac{\pi}{2},\frac{\pi}{2})$ and is essentially symmetric upon reflection around this point. Such a dispersion is, therefore, well fit using second and third NN hopping parameters only and, in order to reproduce the flatness along $(0,\pi)-(\pi,0)$ requires $t_2 \approx 2t_3$. Hence, in the one-hole limit, NN hopping is frustrated and the hole hops coherently only within the same sublattice[1]. These hopping processes can be understood as three step processes allowed by spin fluctuations [108]. Even though the "doped carrier" formulation of the $tt't''J$ model easily captures the frustration of NN hopping [Expression (4.17)], the spin fluctuation induced contribution to hole hopping is inherently a loop contribution and escapes the realm of MF theory, which is a semiclassical saddle-point approach.

The dispersion observed experimentally in undoped cuprates is not flat along $(0,\pi)-(\pi,0)$ [22, 61] and requires the introduction of non-zero t' and t'' [46, 48, 61, 109, 110]. Band calculations expect these parameters to be $t' \approx -2t''$ [111], in which case the resulting $4t' \cos k_x \cos k_y + 2t''(\cos 2k_x + \cos 2k_y)$ contribution to the dispersion is flat along $(0,0)-(\pi,\pi)$ but not along $(0,\pi)-(\pi,0)$. Note that t' and

[1]It is important to remark that a coherent dispersion involving only intra-sublattice processes, like 2^{nd} and 3^{rd} NN hopping processes, is consistent with the symmetries of the pure tJ model where $t' = t'' = 0$. The tJ model has particle-hole symmetry, which is broken in the $tt't''J$ model due to the inclusion of t' and t''. However, if NN hopping vanishes, *i.e.* t is set to zero, the resulting $t't''J$ model also satisfies particle-hole symmetry.

t'' do not frustrate nor are frustrated by local AF correlations, in contrast to the NN hopping parameter t.

The dopon dispersion $\gamma_{\boldsymbol{k}}$ describes the local dynamics of a vacancy surrounded by staggered local moments and reproduces the one-hole dispersion in the $tt't''J$ model. Given all the above, we separately consider the contributions to the effective parameters t_2 and t_3 that control $\gamma_{\boldsymbol{k}}$ along $(0,0)-(\pi,\pi)$ and along $(0,\pi)-(\pi,0)$. We thus write $t_2 = t_2^A + t_2^B$ and $t_3 = \frac{t_2^A}{2} - \frac{t_2^B}{2}$ and recast $\gamma_{\boldsymbol{k}}$ as

$$\begin{aligned}\gamma_{\boldsymbol{k}} + \mu_d = t_2^A \left[\cos k_x \cos k_y + \frac{1}{4}\left(\cos 2k_x + \cos 2k_y\right)\right] + \\ + t_2^B \left[\cos k_x \cos k_y - \frac{1}{4}\left(\cos 2k_x + \cos 2k_y\right)\right]\end{aligned} \tag{4.26}$$

The first term in (4.26) captures the spin fluctuation assisted hopping described above, while the second term reflects the effect of t' and t''.

Both experiments [34, 112, 24, 22, 61, 113, 53] and numerical calculations of the $tt't''J$ model [46, 30] yield a nodal dispersion width $\sim 2J$, which implies $t_2^A = J$. At zero doping the single hole dispersion is quite symmetric around $(\frac{\pi}{2}, \frac{\pi}{2})$ and the dispersion width along $(0,\pi)-(\pi,0)$ is also $\sim 2J$ [22, 61, 113], which requires $t_2^B = -J$. We remark that $t' \approx -J$ is the estimate from band theory [111]. This means that the dopon MF dispersion $\gamma_{\boldsymbol{k}}$ in the undoped limit captures not only the NN hopping frustration, but also the renormalization of t' and t'' by a factor $\approx \frac{1}{4}$ [Expression (4.17)]. Numerical calculations of the single hole $tt't''J$ model also appear to suggest a similar renormalization by a factor in the range $\approx \frac{1}{3} - \frac{1}{2}$ [46].

The high energy band $\epsilon^{\pm}_{2,\boldsymbol{k}}$, which up to corrections of order x is given by the dopon dispersion $\gamma_{\boldsymbol{k}}$, fits not only the angle-resolved photoemission spectroscopy (ARPES) dispersion in undoped compounds but also reproduces these same features which survive in doped samples at energies above the observed dSC dispersion [34, 24]. In particular, at $(0,\pi)$ the $\epsilon^{-}_{2,\boldsymbol{k}}$ band corresponds to the high energy pseudogap [22] which ARPES data shows continuously decreases upon increasing doping, eventually vanishing at $x \approx 0.20 - 0.30$ [22, 53]. This reflects the change in character of local spin correlations, which deplete t' and t'' (see discussion in Sec. 7.4) and, here, we consider that t' and t'' are renormalized to zero at $x = 0.30$. We do not capture this effect at MF level and, below, we simply interpolate the effective hopping parameters t_2 and t_3 between their values at $x = 0$ and $x = 0.30$. As a result, t_2 and t_3 become doping dependent. Following Ref. [106] we consider a linear interpolation between $x = 0$ and $x = 0.30$

$$\begin{aligned} t_2^{HD} &= J - J\left(1 - \frac{x}{0.3}\right) \\ t_3^{HD} &= \frac{J}{2} + \frac{J}{2}\left(1 - \frac{x}{0.3}\right) \end{aligned} \tag{4.27}$$

However, at this stage, there is no theoretical motivation to select one interpolation scheme over another. For that reason, we have also considered alternative interpolations schemes, say by changing the exponent of $\left(1 - \frac{x}{0.3}\right)$ in (4.27) from 1 to 2 (not

shown though), without affecting our general conclusions. The superscript HD in t_2^{HD} and t_3^{HD} indicates that the above discussion concerns the hole doped regime of cuprates. In the electron doped regime, t' and t'' change sign [48, 60] and, hence, we take

$$t_2^{ED} = J + J\left(1 - \frac{x}{0.3}\right)$$
$$t_3^{ED} = \frac{J}{2} - \frac{J}{2}\left(1 - \frac{x}{0.3}\right) \tag{4.28}$$

In Ref. [106] we took $t_1 = 2J$. Here, we rather use the, almost equal, conventional bare value $t_1 = 3J$. The resulting differences are minor, as discussed below.

We would like to emphasize that at $x = 0$ the effective hopping parameters t_1, t_2 and t_3 agree with the bare values obtained from band calculations and lead to a MF dispersion *quantitatively* consistent with experiments and numerical calculations. Away from half-filling, we are required to change t_2 and t_3 with doping in order to fit the high energy pseudogap scale. Even though this effect is beyond the scope of the current MF scheme, in Sec. 7.4 we qualitatively discuss it and propose an explanation for the observed behavior. Still, note that t_2 and t_3 are used to control the high energy dispersion $\epsilon_{2,\boldsymbol{k}}$ in consonance with experiments. There is no such direct experimental input on the low energy band $\epsilon_{1,\boldsymbol{k}}$, and all its properties result from the theory.

4.4 Doped carrier mean-field phase diagram

Starting from the MF Hamiltonian (4.22) the MF phase diagram can be computed for different values of doping x and temperature T by requiring the self-consistency of the MF parameters and by determining the value of the Lagrange multipliers μ_d and a_0 that enforce the doping density ($\langle d_i^\dagger d_i \rangle = x$) and the global $SU(2)$ projection ($\langle f_i^\dagger f_i \rangle = 1$) constraints. The resulting equations are derived in Appendix 4.7.

The MF parameters that determine the different MF phases in the "doped carrier" MF theory of the $tt't''J$ model bear a close resemblance to those of the slave boson approach. In both cases, χ and Δ arise from introducing the fermionic representation of spins. In the present MF formulation of the $tt't''J$ model the bound state of a dopon and a spinon is analogous to the holon in the slave boson approach as it is further motivated in Sec. 7.5. Hence, the spinon-dopon pairing transition which leads to non-zero b_0 and b_1 is equivalent to the holon condensation transition in the slave boson framework. Therefore, it is not surprising that, at the level of the MF phase diagram, both approaches are similar to each other. In particular, the "doped carrier" MF phase diagram includes the same phases as the slave boson MF phase diagram [57].

Fig. 4-1(a) depicts the MF phase diagram for both the hole and electron doped regimes, which are distinguished by the effective hopping parameters (4.27) and (4.28). The maximum temperature shown is $T = 0.30J$, in which case we always find that $\chi \neq 0$. Only at higher temperatures does χ vanish and, thus, do the lattice spins decouple from each other at MF level. The MF phase diagram, Fig 4-1a, shows

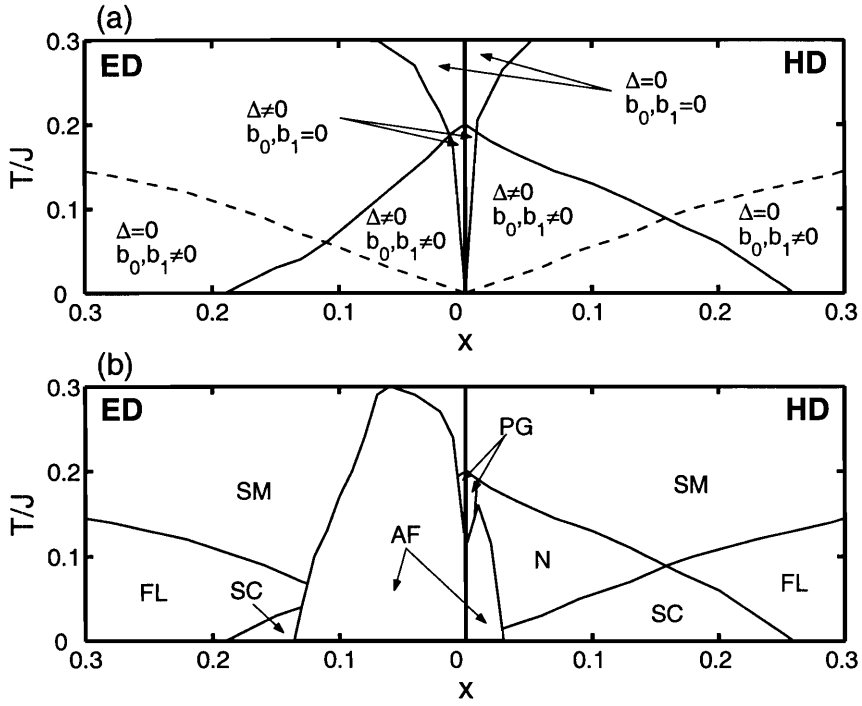

Figure 4-1: (a) Doping-temperature MF phase diagram of H_{tJ}^{MF} in (4.22). It contains four regions where $\Delta = 0$ or $\Delta \neq 0$ and where $b_0 = b_1 = 0$ or $b_0, b_1 \neq 0$. The dashed lines indicate the T_{KT} described in the main text where long-range order in the spinon-dopon mixing channel is destroyed by phase fluctuations. (b) Doping-temperature MF phase diagram of H_{AF}^{MF} in (4.30) in the absence of coexistence of spinon-dopon mixing and staggered magnetization. It includes the AF, dSC, strange metal (SM), Fermi liquid (FL), and pseudogap with and without Nernst signal, labeled by N and PG respectively. Both hole doped (HD) and electron doped (ED) cases, as defined by the effective hopping parameters in (4.27) and (4.28) and $t_1 = 3J$, are depicted in (a) and (b).

four different regions that correspond to the strange metal ($b_0, b_1, \Delta = 0$), pseudogap metal ($b_0, b_1 = 0$ and $\Delta \neq 0$), d-wave SC ($b_0, b_1, \Delta \neq 0$) and Fermi liquid ($b_0, b_1 \neq 0$ and $\Delta = 0$) states, whose physical properties and relevance to the physical phase diagram of cuprates has been discussed in the literature [32, 57, 58], as we briefly review in the following.

In the strange metal state the low lying excitations are spinons, which have an ungaped Fermi surface and, as such, lead to a large low energy spin density of states. Since spinons, which are charge neutral, do not coherently mix with dopons, which are charged, the resulting phase is an incoherent metal. When $\Delta \neq 0$ spinons pair up and open a gap in the uniform susceptibility in agreement with the observed reduction of the Knight shift in the pseudogap regime [19]. Despite the gap, spin correlations at (π, π) are enhanced by the gapless $U(1)$ gauge field [63], as expected in the underdoped regime close to half-filling. Below the spinon-dopon pairing temperature, the motion of spinons leads to a backflow in the charged $b_{0,1}$ condensate and, effectively, spinons transport electric charge. As a result, if spinons are paired in the dSC channel, the resulting state is a d-wave superconductor. If, instead, spinons are not superfluid the electronic system is in the Fermi liquid state, in consistency with the Ioffe-Larkin sum rule [114].

We note that the spinon-dopon MF mixing transition temperature is very high even at very low values of x and, as such, the pseudogap regime with no spinon-dopon mixing is reduced to a tiny region in phase space and, at the same time, the maximum T_c for the dSC state occurs at higher temperature and lower doping than in real materials. Before discussing the steepness of this transition temperature slope, we remark that at MF level the effect of phase fluctuations is neglected. Hence, despite the high MF transition temperature, phase fluctuations may destroy long-range SC phase coherence at a lower temperature. Since SC order appears upon the condensation of b_0, we must assess the strength of b_0's phase fluctuations. As stated above, b_0 is a bosonic collective mode which is closely related to the holon in the slave boson approach. Thus, to estimate b_0's condensate's effective action we make use of the holon hopping term in the slave boson decoupling of the $tt't''J$ model (3.11) in Chapter 3. The resulting 2D lattice-XY model $-\frac{|t_1|\chi}{2}\sum_{<ij>}(b^*_{0i}b_{0j} + h.c.)$ has a Kosterlitz-Thouless transition temperature $T_{KT} = 0.9|t_1|\chi b_0^2$ [115], which is plotted as the dashed-line in Fig. 4-1(a). Below this temperature the fields b_0 and b_1 display long-range phase coherence and the electronic system is a d-wave superconductor. Above T_{KT} the condensate average $\langle b_0 \rangle$ vanishes but its magnitude $\langle |b_0| \rangle$ is non-zero in the temperature range between T_{KT} and the MF spinon-dopon mixing temperature. In the underdoped regime, the pseudogap normal state then has two different regions. Below the MF spinon-dopon mixing temperature there exist strong short-range SC fluctuations, which can be experimentally detected through the Nernst effect [116, 117, 118, 119] or the diamagnetic response [120] and we call this the Nernst region [labelled by N in Fig. 4-1(b)]. Above this temperature a pseudogap state with no signatures of SC correlations is present [labelled by PG in Fig. 4-1(b)]. Even though the existence of two such regions receives experimental support the size of the Nernst regime in Fig. 4-1(b) is far larger than observed in real materials. As

we discuss in Sec. 7.4, at higher temperatures we overestimate the stability of spinon-dopon pairs and, thus, we expect the Nernst region to be smaller than shown in Fig. 4-1(b).

At and close to half-filling the cuprate compounds display long-range AF order [101, 121, 122, 123]. The above MF theory of the $tt't''J$ model assumes a spin liquid background and ignores the AF phase believed to be present close to the Heisenberg limit [29]. Therefore, below we further introduce the MF decoupling channels that account for the staggered magnetization in the lattice spin and dopon systems

$$\begin{aligned} m &= (-1)^{i_x+i_y}\langle S_i^z\rangle \\ n &= -\frac{(-1)^{i_x+i_y}}{16}\langle \sum_{\nu=2,3} t_\nu \sum_{\hat{u}\in \nu\, NN} d_i^\dagger \sigma_z d_{i+\hat{u}} + h.c.\rangle \end{aligned} \tag{4.29}$$

The resulting MF Hamiltonian for the AF phase is

$$\begin{aligned} H_{AF}^{MF} &= H_{tJ}^{MF} + 2J^* N m^2 - 4Nmn - \\ &\quad - 2\left(J^* m - n\right)\sum_{\boldsymbol{k}} \psi_{\boldsymbol{k}+(\pi,\pi)}^\dagger \psi_{\boldsymbol{k}} - 2m\sum_{\boldsymbol{k}} (\gamma_{\boldsymbol{k}} + \mu_d)\eta_{\boldsymbol{k}+(\pi,\pi)}^\dagger \eta_{\boldsymbol{k}} \end{aligned} \tag{4.30}$$

It is well known that the above MF AF decoupling scheme overestimates the strength of magnetic moments. To effectively include the effect of fluctuations, which decrease the staggered magnetization, it is customary to introduce a renormalized exchange constant $J^* = \lambda J$ in the staggered magnetization decoupling channel [124]. The renormalization factor is determined upon fitting the MF staggered magnetization at half-filling to the quantum Monte-Carlo estimate $m = 0.31$ [125]. In the present case, this condition requires $\lambda = 0.34$.

To construct the phase diagram we ignore states with coexistence of antiferromagnetism and superconductivity. Hence, we compare the free-energy of self-consistent solutions of the AF MF theory in (4.30) with b_0 and b_1 set to zero, to that of self-consistent solutions of the paramagnetic MF theory (4.22). The saddle point solutions of (4.30) are derived in Appendix 4.8. The resulting phase diagram, which displays all experimentally observed regions, is depicted in Fig. 4-1(b). We see that the change of hopping parameters between hole and electron doped regimes leads to an asymmetric phase diagram. Antiferromagnetism is very feeble on the hole doped side, where it is destroyed at $x = 0.01$, and a large SC dome dominates the low temperature region. In the underdoped regime a large pseudogap region is present mostly covered by the Nernst regime of short-range SC fluctuations. In the electron doped case, however, AF order is more robust while superconductivity is weaker than on the hole doped side. As a result, AF order survives up to $x = 0.125$ and covers a considerable fraction of the SC dome, whose maximum doping level is smaller than for the hole doped regime. The Nernst region is also covered by the AF phase in the electron doped case, in conformity with the lack of experimental evidence for a vortex induced Nernst signal on these materials [126]. We remark that the strength of magnetic moments is controlled by the renormalized J^*, which is determined by the behavior of the MF

theory at half-filling. Still, the phase diagram in Fig. 4-1(b) shows that, for both hole and electron doped cases, AF order is destroyed at a doping level consistent with experiments [101, 121, 122, 123].

The above differences between the hole and electron doped phase diagrams are easily rationalized in terms of the different bare intra-sublattice hopping parameters t' and t'', which frustrate intra-sublattice hopping, and thus antiferromagnetism as well, in the hole doped regime. On the electron doped side, t' and t'' favor intra-sublattice hopping instead and, as such, decrease the coupling between holes and AF correlations [60]. In addition, on the electron doped side the dopon dispersion is gaped at $(\frac{\pi}{2}, \frac{\pi}{2})$, instead of $(\pi, 0)$ as in hole doped materials. This fact frustrates the spinon $d_{x^2-y^2}$-wave dispersion, whose gap appears at $(0, \pi)$, and enfeebles the SC state in the electron doped regime.

Comparing the phase diagram in Fig. 4-1 to that of Ref. [106], where $t_1 = 2J$ was used, also demonstrates the role played by this parameter in strengthening SC correlations. Indeed, a main difference between both phase diagrams is that the spinon-dopon mixing transition temperature is higher in Fig. 4-1. To understand this effect recall that, without spinon-dopon mixing, dopons cannot hop between NN (Sec. 4.3.2). However, upon hybridizing with spinons, dopons manage to hop between the two different sublattices, leading to a kinetic energy gain which increases with t_1. Hence, a larger t_1 naturally enhances SC correlations.

The above discussion points out how the hopping parameters t, t' and t'' control the phase boundaries in the MF phase diagram. For instance, the maximum doping value at which SC occurs decreases as t' and t'' change from their values in the hole doped case toward the electron doped regime values. This change is continuous and indicates that as $-t'$ and t'' are reduced SC is weakened, in agreement with experiments and other theoretical approaches. Indeed, band theory calculations together with experimental data support that the maximum T_c for various cuprate families increases with $-t'/t$ [111]. ARPES results also suggest the correlation between the high energy pseudogap scale, which is controlled by t' and t'', and the maximum T_c [53]. In addition, variational Monte Carlo calculations further substantiate the above role of t' in determining the strength of SC correlations [127].

Interestingly, t, t' and t'' also control the competition between AF and SC order. As discussed before, the change in t' and t'' between the hole and electron doped cases greatly modifies the extension of the AF region in the phase diagram [Fig. 4-1(b)]. The above competition is even more striking when we consider electron doped compounds alone. The as-grown electron doped samples are not SC and display long-range AF order up to $x \approx 0.20$ [128]. After the oxygen reduction process, which removes about 1% of the oxygen atoms in these materials, AF is destroyed at $x \approx 0.10-0.14$ and, at higher doping values, the samples superconduct [129, 122, 123]. Within the present context, we propose this sharp change follows the alteration of the effective in-plane parameters t, t' and t''. Both t' and t'' depend on the chemical composition outside the copper-oxide layers [111]. If such a composition changes in a way that the magnitude of t' and t'' decreases, the phase-space volume of AF is reduced while SC correlations are enhanced. Alternatively, if the oxygen reduction process acts on the copper-oxide planes in such a manner that t effectively decreases,

then $\frac{t}{J} \sim \frac{U}{t}$ increases, which favors superconductivity over antiferromagnetism. The latter scenario receives support from experimental evidence for the removal of oxygen atoms from the copper-oxide planes under the reduction process in both PCCO [130] and NCCO [131].

4.5 Conclusions

In this chapter we derive a new formulation of the $tt't''J$ model in terms of hole and spin operators instead of electron and spin operators. Since holes are the doped carriers, we name it the "doped carrier" formulation of the $tt't''J$ model. Close to half-filling the doped carrier density is small and, thus, we circumvent the use of the projection operators $\mathcal{P}$, whose effect is captured by the interaction between doped carriers and spins in (4.9).

The Hamiltonian (4.3) provides a new starting point to deal with doped spin models, which we pursue to develop a new, fully fermionic, MF theory of doped Mott insulators. The resulting "doped carrier" MF theory is constructed to address the low doping and low temperature paramagnetic regime of the $tt't''J$ model.

In the undoped limit, the above MF theory accounts for the frustration of NN hopping and for the renormalization of t' and t'' that lead to a MF dispersion in quantitative agreement with experiments [22, 61, 113] and numerical calculations [46, 48, 61, 109, 110]. In this context, we emphasize that, for $x = 0$, the bare hopping parameters t, t' and t'' obtained from band calculations [111] reproduce the ARPES dispersion of the undoped parent compounds. For finite doping, though, we reduce t' and t'' to fit the evolution of the high energy pseudogap scale at $(0, \pi)$. This procedure is not self-consistent in the present MF theory, but in Sec. 7.4 we argue such a doping dependence reflects the growing relevance of singlet bond correlations over short-range AF correlations as materials are doped away from half-filling.

Remarkably, using t, t' and t'' motivated by band theory and with the aforementioned little experimental input the "doped carrier" MF theory leads to a semi-quantitative correct phase diagram for both hole and electron doped cuprates (Fig. 4-1). Specifically, in the hole doped case a large SC dome and extended pseudogap regime are obtained, while superconductivity is much weaker on the electron doped side where it is partly overtaken by the robust AF phase.

The "doped carrier" formulation of the $tt't''J$ model explicitly describes the interaction between doped carriers and the surrounding spins in the term (4.9). Therefore, it provides the means to account for the interplay between charge dynamics and the local spin correlations, *whatever they are*. This fact is captured in the above MF theory: the vacancy in the one-dopon state is encircled by staggered local moments which inhibit NN hopping; upon spinon-dopon mixing the vacancy changes the surrounding spin background and gains kinetic energy, which is the driving force for the dSC state at low doping. Interestingly, short-range AF correlations can enhance or deplete dSC correlations depending on the sign of t' and t''. Specifically, if these hopping parameters favor a gap in the single hole $tt't''J$ model dispersion at $(\frac{\pi}{2}, \frac{\pi}{2})$, as in the electron doped regime, the vacancies when in the presence of local AF configura-

tions frustrate the dSC gap and, thus, superconductivity as well. The opposite effect occurs if, instead, t' and t'' induce a gap at $(0, \pi)$ in the single hole $tt't''J$ model dispersion. Hence, the interplay between short-range AF and dSC correlations provides a rational for the role of t' and t'' in strengthening superconductivity as expected by experiments and other theoretical approaches [111, 53, 127]. This theory also offers possible scenarios for the difference between phase diagrams of as-grown and oxygen reduced electron doped samples [128, 129, 122, 123].

In this chapter we analyze how different spin background correlations conspire to yield a phase diagram that is consistent with experiments and other theoretical studies. Doped carrier dynamical properties are also strongly affected by the presence of such correlations as demonstrated in the following chapters. In particular, in Chapters 5 and 6 we show that several non-trivial features of the electron spectral function and of the tunneling conductance spectrum of cuprates are reproduced by the herein introduced MF theory.

4.6 Appendix A: Hopping term in enlarged Hilbert space

In Sec. 4.2.3 the $tt't''J$ model hopping term is written in the enlarged Hilbert space of the "doped carrier" formulation (4.9). All dopon hopping processes with non-vanishing matrix elements are shown in (4.7) and, in (4.8), the Hamiltonian matrix term for a dopon hopping between site j and site i is explicitly written. This matrix acts on the initial state vectors with a dopon on site j

$$\begin{bmatrix} |\uparrow\uparrow;\uparrow 0\rangle \\ |\uparrow\downarrow;\uparrow 0\rangle \\ |\uparrow\uparrow;\downarrow 0\rangle \\ |\uparrow\downarrow;\downarrow 0\rangle \\ |\downarrow\uparrow;\uparrow 0\rangle \\ |\downarrow\downarrow;\uparrow 0\rangle \\ |\downarrow\uparrow;\downarrow 0\rangle \\ |\downarrow\downarrow;\downarrow 0\rangle \end{bmatrix} \tag{4.31}$$

and transforms them into the final state vectors with a dopon on site i

$$\begin{bmatrix} |\uparrow 0;\uparrow\uparrow\rangle \\ |\uparrow 0;\uparrow\downarrow\rangle \\ |\uparrow 0;\downarrow\uparrow\rangle \\ |\uparrow 0;\downarrow\downarrow\rangle \\ |\downarrow 0;\uparrow\uparrow\rangle \\ |\downarrow 0;\uparrow\downarrow\rangle \\ |\downarrow 0;\uparrow\downarrow\rangle \\ |\downarrow 0;\downarrow\uparrow\rangle \\ |\downarrow 0;\downarrow\uparrow\rangle \\ |\downarrow 0;\downarrow\downarrow\rangle \end{bmatrix} \tag{4.32}$$

The ket notation $\left|\widetilde{\boldsymbol{S}}_j, \frac{1}{2}\widetilde{\mathcal{P}}d_j^\dagger \boldsymbol{\sigma} d_j \widetilde{\mathcal{P}}\,;\, \widetilde{\boldsymbol{S}}_i, \frac{1}{2}\widetilde{\mathcal{P}}d_i^\dagger \boldsymbol{\sigma} d_i \widetilde{\mathcal{P}}\right\rangle$ is used above.

The hopping matrix (4.8) can be written as linear combination of terms involving lattice spin and dopon operators. These terms must hop a dopon from site j to site i and must be spin rotation invariant. The list of all such terms is: $\widetilde{\mathcal{P}}\left(d_i^\dagger \boldsymbol{\sigma} d_j\right).\left(i\widetilde{\boldsymbol{S}}_i \times \widetilde{\boldsymbol{S}}_j\right)\widetilde{\mathcal{P}}$, $\widetilde{\mathcal{P}}\left(d_i^\dagger \boldsymbol{\sigma} d_j.\widetilde{\boldsymbol{S}}_i\right)\widetilde{\mathcal{P}}$, $\widetilde{\mathcal{P}}\left(d_i^\dagger \boldsymbol{\sigma} d_j.\widetilde{\boldsymbol{S}}_j\right)\widetilde{\mathcal{P}}$, $\widetilde{\mathcal{P}}\left(d_i^\dagger d_j \widetilde{\boldsymbol{S}}_i.\widetilde{\boldsymbol{S}}_j\right)\widetilde{\mathcal{P}}$, $\widetilde{\mathcal{P}}\left(d_i^\dagger d_j\right)\widetilde{\mathcal{P}}$. Below we write these terms in matrix form for the initial and final states in (4.31) and (4.32) respectively.

(i) Matrix elements of $\widetilde{\mathcal{P}}\left(d_i^\dagger \boldsymbol{\sigma} d_j\right).\left(i\widetilde{\boldsymbol{S}}_i \times \widetilde{\boldsymbol{S}}_j\right)\widetilde{\mathcal{P}}$ are easily calculated after rewriting it as

$$\begin{aligned} &\widetilde{\mathcal{P}}\left[\tfrac{1}{2}d_i^\dagger \sigma_z d_j\left(\widetilde{\boldsymbol{S}}_i^- \widetilde{\boldsymbol{S}}_j^+ - -\widetilde{\boldsymbol{S}}_i^+ \widetilde{\boldsymbol{S}}_j^-\right) + \widetilde{\boldsymbol{S}}_i^z\left(\widetilde{\boldsymbol{S}}_j^- d_i^\dagger \sigma_+ d_j - \widetilde{\boldsymbol{S}}_j^+ d_i^\dagger \sigma_- d_j\right) + \right. \\ &\left. + \widetilde{\boldsymbol{S}}_j^z\left(d_i^\dagger \sigma_- d_j \widetilde{\boldsymbol{S}}_i^+ - d_i^\dagger \sigma_+ d_j \widetilde{\boldsymbol{S}}_i^-\right)\right]\widetilde{\mathcal{P}} \end{aligned} \tag{4.33}$$

where $\widetilde{\boldsymbol{S}}^\pm = \widetilde{\boldsymbol{S}}^x \pm i\widetilde{\boldsymbol{S}}^y$ and $\sigma_\pm = \frac{1}{2}\left(\sigma_x \pm i\sigma_y\right)$. The full matrix is

$$\frac{1}{2}\begin{bmatrix} 0 & 0 & 0 & 0 & 0 & 0 & 0 & 0 \\ 0 & 0 & 1 & 0 & -1 & 0 & 0 & 0 \\ 0 & -1 & 0 & 0 & 1 & 0 & 0 & 0 \\ 0 & 0 & 0 & 0 & 0 & -1 & 1 & 0 \\ 0 & 1 & -1 & 0 & 0 & 0 & 0 & 0 \\ 0 & 0 & 0 & 1 & 0 & 0 & -1 & 0 \\ 0 & 0 & 0 & -1 & 0 & 1 & 0 & 0 \\ 0 & 0 & 0 & 0 & 0 & 0 & 0 & 0 \end{bmatrix} \tag{4.34}$$

To illustrate how (4.34) is computed, consider the matrix element on the fifth row and second column, which is the hopping integral between the second state in (4.31) and the fifth state in (4.32). Its numerical value is determined by the relation $\widetilde{\mathcal{P}}\left(\widetilde{\boldsymbol{S}}_i^z \widetilde{\boldsymbol{S}}_j^- d_i^\dagger \sigma_+ d_j\right)\widetilde{\mathcal{P}}\,|\uparrow\downarrow;\uparrow 0\rangle = \frac{1}{2}\,|\downarrow 0;\uparrow\uparrow\rangle$

(ii) The second and third terms in the above list appear with the same coef-

ficient in the hopping matrix (4.8). We rewrite the dopon-lattice spin exchange $\widetilde{\mathcal{P}}\left(d_i^{\dagger}\boldsymbol{\sigma}d_j\right).\left(\widetilde{\boldsymbol{S}}_i+\widetilde{\boldsymbol{S}}_j\right)\widetilde{\mathcal{P}}$ as

$$\widetilde{\mathcal{P}}\left[d_i^{\dagger}\sigma_z d_j\left(\widetilde{\boldsymbol{S}}_i^z+\widetilde{\boldsymbol{S}}_j^z\right)+d_i^{\dagger}\sigma_+ d_j\left(\widetilde{\boldsymbol{S}}_i^-+\widetilde{\boldsymbol{S}}_j^-\right)+d_i^{\dagger}\sigma_- d_j\left(\widetilde{\boldsymbol{S}}_i^+\widetilde{\boldsymbol{S}}_j^+\right)\right]\widetilde{\mathcal{P}} \tag{4.35}$$

to get the matrix form

$$\begin{bmatrix} 1 & 0 & 0 & 0 & 0 & 0 & 0 & 0 \\ 0 & -1 & 1 & 0 & 1 & 0 & 0 & 0 \\ 0 & 1 & 0 & 0 & 0 & 0 & 0 & 0 \\ 0 & 0 & 0 & 0 & 0 & 0 & 1 & 0 \\ 0 & 1 & 0 & 0 & 0 & 0 & 0 & 0 \\ 0 & 0 & 0 & 0 & 0 & 0 & 1 & 0 \\ 0 & 0 & 0 & 1 & 0 & 1 & -1 & 0 \\ 0 & 0 & 0 & 0 & 0 & 0 & 0 & 1 \end{bmatrix} \tag{4.36}$$

(iii) $\widetilde{\mathcal{P}}\left(d_i^{\dagger}d_j\widetilde{\boldsymbol{S}}_i.\widetilde{\boldsymbol{S}}_j\right)\widetilde{\mathcal{P}}$ leaves the dopon spin unaltered but acts on the lattice spin subspace. We proceed as above to obtain the corresponding matrix

$$\frac{1}{4}\begin{bmatrix} 1 & 0 & 0 & 0 & 0 & 0 & 0 & 0 \\ 0 & 1 & 0 & 0 & 0 & 0 & 0 & 0 \\ 0 & 0 & -1 & 0 & 2 & 0 & 0 & 0 \\ 0 & 0 & 0 & -1 & 0 & 2 & 0 & 0 \\ 0 & 0 & 2 & 0 & -1 & 0 & 0 & 0 \\ 0 & 0 & 0 & 2 & 0 & -1 & 0 & 0 \\ 0 & 0 & 0 & 0 & 0 & 0 & 1 & 0 \\ 0 & 0 & 0 & 0 & 0 & 0 & 0 & 1 \end{bmatrix} \tag{4.37}$$

(iv) $\widetilde{\mathcal{P}}\left(d_i^{\dagger}d_j\right)\widetilde{\mathcal{P}}$ leaves the lattice spins unchanged and reduces to

$$\begin{bmatrix} 1 & 0 & 0 & 0 & 0 & 0 & 0 & 0 \\ 0 & 1 & 0 & 0 & 0 & 0 & 0 & 0 \\ 0 & 0 & 1 & 0 & 0 & 0 & 0 & 0 \\ 0 & 0 & 0 & 1 & 0 & 0 & 0 & 0 \\ 0 & 0 & 0 & 0 & 1 & 0 & 0 & 0 \\ 0 & 0 & 0 & 0 & 0 & 1 & 0 & 0 \\ 0 & 0 & 0 & 0 & 0 & 0 & 1 & 0 \\ 0 & 0 & 0 & 0 & 0 & 0 & 0 & 1 \end{bmatrix} \tag{4.38}$$

Using the above matrices (4.34), (4.36), (4.37) and (4.38) we write the $tt't''J$ hopping matrix (4.8) as

$$\frac{t_{ij}}{2}\widetilde{\mathcal{P}}\left[\left(d_i^{\dagger}\boldsymbol{\sigma}d_j\right).\left(i\widetilde{\boldsymbol{S}}_i\times\widetilde{\boldsymbol{S}}_j-\frac{\widetilde{\boldsymbol{S}}_i+\widetilde{\boldsymbol{S}}_j}{2}\right)+\frac{1}{4}d_i^{\dagger}d_j+d_i^{\dagger}d_j\widetilde{\boldsymbol{S}}_i.\widetilde{\boldsymbol{S}}_j\right]\widetilde{\mathcal{P}} \tag{4.39}$$

4.7 Appendix B: Doped carrier mean-field self-consistent equations

Below we write the set of self-consistent equations that determine the phase diagrams depicted in Sec. 4.4. These conditions are the saddle point equations

$$\frac{\partial F}{\partial \chi} = \frac{\partial F}{\partial \Delta} = \frac{\partial F}{\partial b_0} = \frac{\partial F}{\partial b_1} = \frac{\partial F}{\partial \mu_d} = \frac{\partial F}{\partial a_0} = 0 \tag{4.40}$$

of the MF free-energy F corresponding to the fermionic system described by the MF Hamiltonian (4.22), namely

$$\begin{aligned}\frac{F}{N} = &\frac{3\widetilde{J}}{4}\left(\chi^2+\Delta^2\right) - 2b_0 b_1 - \mu_d(1-x) - \\ &- \frac{T}{N}\sum_{\boldsymbol{k}} \ln\left[1+\cosh\left(\frac{\epsilon^+_{1,\boldsymbol{k}}}{T}\right)\right]\left[1+\cosh\left(\frac{\epsilon^+_{2,\boldsymbol{k}}}{T}\right)\right]\end{aligned} \tag{4.41}$$

The resulting self-consistent equations for the mean-fields χ, Δ, b_0 and b_1, as well as the doping concentration and $SU(2)$ projection constraints, are:

$$\chi = -\frac{1}{4N}\sum_{\boldsymbol{k}}\left(\cos k_x + \cos k_y\right)\left\{\alpha^z_{\boldsymbol{k}} A_{\boldsymbol{k}} - \frac{2\gamma_{\boldsymbol{k}}\beta^2_{\boldsymbol{k}} + \alpha^z_{\boldsymbol{k}}\left[2\beta^2_{\boldsymbol{k}} + \left(\alpha^x_{\boldsymbol{k}}\right)^2 + \left(\alpha^z_{\boldsymbol{k}}\right)^2 - \gamma^2_{\boldsymbol{k}}\right]}{2\sqrt{\delta_{\boldsymbol{k}}}} B_{\boldsymbol{k}}\right\} \tag{4.42}$$

$$\Delta = -\frac{1}{4N}\sum_{\boldsymbol{k}}\alpha^x_{\boldsymbol{k}}\left(\cos k_x - \cos k_y\right)\left\{A_{\boldsymbol{k}} - \frac{2\beta^2_{\boldsymbol{k}} + \left(\alpha^x_{\boldsymbol{k}}\right)^2 + \left(\alpha^z_{\boldsymbol{k}}\right)^2 - \gamma^2_{\boldsymbol{k}}}{2\sqrt{\delta_{\boldsymbol{k}}}} B_{\boldsymbol{k}}\right\} \tag{4.43}$$

$$\begin{aligned}b_1 = -\frac{3}{16N}\sum_{\boldsymbol{k}}\beta_{\boldsymbol{k}}&\left[t_1\left(\cos k_x + \cos k_y\right) + 2t_2\cos k_x\cos k_y + t_3\left(\cos 2k_x + \cos 2k_y\right)\right]\times \\ &\times\left\{A_{\boldsymbol{k}} - \frac{\left(\gamma_{\boldsymbol{k}} + \alpha^z_{\boldsymbol{k}}\right)^2 + \left(\alpha^x_{\boldsymbol{k}}\right)^2}{2\sqrt{\delta_{\boldsymbol{k}}}} B_{\boldsymbol{k}}\right\}\end{aligned} \tag{4.44}$$

$$b_0 = -\frac{1}{2N}\sum_{\boldsymbol{k}}\beta_{\boldsymbol{k}}\left\{A_{\boldsymbol{k}} - \frac{\left(\gamma_{\boldsymbol{k}} + \alpha^z_{\boldsymbol{k}}\right)^2 + \left(\alpha^x_{\boldsymbol{k}}\right)^2}{2\sqrt{\delta_{\boldsymbol{k}}}} B_{\boldsymbol{k}}\right\} \tag{4.45}$$

$$x = 1 - \frac{1}{2N}\sum_{\boldsymbol{k}}\left\{\gamma_{\boldsymbol{k}} A_{\boldsymbol{k}} - \frac{2\alpha^z_{\boldsymbol{k}}\beta^2_{\boldsymbol{k}} + \gamma_{\boldsymbol{k}}\left[2\beta^2_{\boldsymbol{k}} + \gamma^2_{\boldsymbol{k}} - \left(\alpha^x_{\boldsymbol{k}}\right)^2 - \left(\alpha^z_{\boldsymbol{k}}\right)^2\right]}{2\sqrt{\delta_{\boldsymbol{k}}}} B_{\boldsymbol{k}}\right\} \tag{4.46}$$

$$0 = \frac{1}{2N}\sum_{\boldsymbol{k}}\left\{\alpha^z_{\boldsymbol{k}} A_{\boldsymbol{k}} - \frac{2\gamma_{\boldsymbol{k}}\beta^2_{\boldsymbol{k}} + \alpha^z_{\boldsymbol{k}}\left[2\beta^2_{\boldsymbol{k}} + \left(\alpha^x_{\boldsymbol{k}}\right)^2 + \left(\alpha^z_{\boldsymbol{k}}\right)^2 - \gamma^2_{\boldsymbol{k}}\right]}{2\sqrt{\delta_{\boldsymbol{k}}}} B_{\boldsymbol{k}}\right\} \tag{4.47}$$

where we introduce

$$A_{\boldsymbol{k}} = \frac{\sinh\left(\frac{\epsilon^+_{1,\boldsymbol{k}}}{T}\right)}{\epsilon^+_{1,\boldsymbol{k}}\left[1+\cosh\left(\frac{\epsilon^+_{1,\boldsymbol{k}}}{T}\right)\right]} + \frac{\sinh\left(\frac{\epsilon^+_{2,\boldsymbol{k}}}{T}\right)}{\epsilon^+_{2,\boldsymbol{k}}\left[1+\cosh\left(\frac{\epsilon^+_{2,\boldsymbol{k}}}{T}\right)\right]} \tag{4.48}$$

and

$$B_{\boldsymbol{k}} = \frac{\sinh\left(\frac{\epsilon^+_{1,\boldsymbol{k}}}{T}\right)}{\epsilon^+_{1,\boldsymbol{k}}\left[1+\cosh\left(\frac{\epsilon^+_{1,\boldsymbol{k}}}{T}\right)\right]} - \frac{\sinh\left(\frac{\epsilon^+_{2,\boldsymbol{k}}}{T}\right)}{\epsilon^+_{2,\boldsymbol{k}}\left[1+\cosh\left(\frac{\epsilon^+_{2,\boldsymbol{k}}}{T}\right)\right]} \tag{4.49}$$

The remaining notation is defined in (4.23) and (4.25).

4.8 Appendix C: Antiferromagnetic mean-field self-consitent equations

In Sec. 4.4 we extend the "doped carrier" MF theory to include the staggered magnetization decoupling channel and obtain the MF Hamiltonian (4.30). In this paper we do not consider states with coexisting AF and SC order and we set b_0 and b_1 to zero in (4.30). Staggered moments break translation symmetry and reduce the BZ by half. Yet, in the present case, we can define two spinon and two dopon bands in the full BZ, namely

$$\begin{aligned}\epsilon^{\pm}_{s,\boldsymbol{k}} &= \pm\sqrt{\left(\alpha^x_{\boldsymbol{k}}\right)^2 + \left(\alpha^z_{\boldsymbol{k}}\right)^2 + \nu^2_{\boldsymbol{k}}} \\ \epsilon^{\pm}_{d,\boldsymbol{k}} &= \left(1 \mp 2|m|\right)\gamma_{\boldsymbol{k}} - \mu_d\end{aligned} \tag{4.50}$$

where $\nu_{\boldsymbol{k}} = -2\left(J^* m - n\right)$. In the absence of spinon-dopon hybridization $a_0 = 0$ and $\alpha^z_{\boldsymbol{k}} = -\left(\frac{3\tilde{J}}{4}\chi - \frac{t_1 x}{2}\right)\left(\cos k_x + \cos k_y\right)$.

The resulting MF free-energy is

$$\begin{aligned}\frac{F}{N} = {} & \frac{3\tilde{J}}{4}\left(\chi^2+\eta^2\right) + 2J^* m^2 - 4mn - \mu_d(1-x) - \\ & - \frac{T}{N}\sum_{\boldsymbol{k}}\left\{\ln\left[\cosh\left(\frac{\gamma_{\boldsymbol{k}}-\mu_d}{T}\right) + \cosh\left(\frac{2m\gamma_{\boldsymbol{k}}}{T}\right)\right] + \ln\left[1+\cosh\left(\frac{\epsilon^+_{s,\boldsymbol{k}}}{T}\right)\right]\right\}\end{aligned} \tag{4.51}$$

and the self-consistency equations

$$\frac{\partial F}{\partial \chi} = \frac{\partial F}{\partial \Delta} = \frac{\partial F}{\partial m} = \frac{\partial F}{\partial n} = \frac{\partial F}{\partial \mu_d} = 0 \tag{4.52}$$

reduce to

$$\chi = -\frac{1}{2N}\sum_{\boldsymbol{k}} \frac{\alpha^z_{\boldsymbol{k}}\left(\cos k_x + \cos k_y\right)}{\epsilon^+_{s,\boldsymbol{k}}} \frac{\sinh\left(\frac{\epsilon^+_{s,\boldsymbol{k}}}{T}\right)}{1+\cosh\left(\frac{\epsilon^+_{s,\boldsymbol{k}}}{T}\right)} \tag{4.53}$$

$$\Delta = -\frac{1}{2N}\sum_{\boldsymbol{k}} \frac{\alpha^x_{\boldsymbol{k}}\left(\cos k_x - \cos k_y\right)}{\epsilon^+_{s,\boldsymbol{k}}} \frac{\sinh\left(\frac{\epsilon^+_{s,\boldsymbol{k}}}{T}\right)}{1+\cosh\left(\frac{\epsilon^+_{s,\boldsymbol{k}}}{T}\right)} \tag{4.54}$$

$$m = \frac{1}{N}\sum_{\boldsymbol{k}} \frac{J^* m - n}{\epsilon^+_{s,\boldsymbol{k}}} \frac{\sinh\left(\frac{\epsilon^+_{s,\boldsymbol{k}}}{T}\right)}{1+\cosh\left(\frac{\epsilon^+_{s,\boldsymbol{k}}}{T}\right)} \tag{4.55}$$

$$n = -\frac{1}{2N}\sum_{\boldsymbol{k}} \frac{\gamma_{\boldsymbol{k}} \sinh\left(\frac{2m\gamma_{\boldsymbol{k}}}{T}\right)}{\cosh\left(\frac{\gamma_{\boldsymbol{k}}-\mu_d}{T}\right)+\cosh\left(\frac{2m\gamma_{\boldsymbol{k}}}{T}\right)} \tag{4.56}$$

$$x = 1 - \frac{1}{N}\sum_{\boldsymbol{k}} \frac{\sinh\left(\frac{\gamma_{\boldsymbol{k}}-\mu_d}{T}\right)}{\cosh\left(\frac{\gamma_{\boldsymbol{k}}-\mu_d}{T}\right)+\cosh\left(\frac{2m\gamma_{\boldsymbol{k}}}{T}\right)} \tag{4.57}$$

Chapter 5

Electron spectral function of superconducting doped Mott insulators

How now, wit! Whither wander you?

William Shakespeare

5.1 Introduction

The evolution of the electronic structure from the undoped antiferromagnetic (AF) insulator to the overdoped metallic state of cuprates is a long standing problem. The plethora of anomalous behavior displayed by these materials is particularly striking in hole underdoped samples both in the normal metallic state – the well renown pseudogap regime [132] – and in the d-wave superconducting (dSC) state. Even though the dSC phase that intervenes between the undoped insulator and overdoped metal is believed to be conventional, as attested by flux quantization experiments [5, 7, 8] and the evidence for long-lived Bogoliubov nodal excitations [9, 10, 11, 12], quasiparticle properties in these materials deviate in many ways from the BCS pairing state of otherwise effectively free electrons. In fact, angle-resolved photoemission spectroscopy (ARPES), which is particularly suited to probe the electronic properties of the aforementioned high-temperature superconducting (SC) state, reveals strong band renormalization effects such as the nodal dispersion kink [31, 34, 133, 134, 135] and the flatness of the dispersion around $(0, \pi)$ and $(\pi, 0)$ [136, 135, 137] in all studied cuprate families. In the underdoped regime this experimental probe further unveils the redistribution of spectral weight in energy-momentum space, offering evidence for a dichotomy of the electronic excitations: excitations around the nodal points $[\boldsymbol{k} = (\pm\frac{\pi}{2}, \pm\frac{\pi}{2})]$ are well described as Landau's quasiparticles while those near the anti-nodal points $[\boldsymbol{k} = (\pi, 0), (0, \pi)]$ show no signs of quasiparticle-like behavior. This momentum space anisotropy, which underlies the observed spectral weight arcs around the nodal direction [31, 23, 34, 112], is also supported by numerical studies of the $tt't''J$ model. These studies relate the absence of quasiparticles close to the

antinodal points to the presence of excitations that only carry spin [44, 45, 47, 102], as suggested by some experimental work [138, 139].

In the slave boson approach to the tJ model [57] the electron is split into a spinon (a spin-1/2 neutral fermion) and a holon (a spin-0 charged boson). The spin-charge separation phenomenon corresponds to the rapid decay of an electron excitation into a spinon and a holon, leading to the lack of quasiparticle features as observed near the anti-nodal points. However, the appearance of quasiparticles near the nodal points means that, in this $\boldsymbol{k}$-space region, the spinon and the holon form a bound state [57, 63]. Within the slave boson theory this fact can only be captured if we go beyond the mean-field (MF) approximation. In order to overcome this shortcoming, here we resort to the new MF approach to the generalized-tJ model introduced in Chapter 4. Instead of using spinons and holons, the "doped carrier" MF theory describes the model in terms of spinons and dopons. The latter objects correspond to the doped carriers and, thus, are spin-1/2 charged fermions responsible for quasiparticle properties in the underdoped regime.

The above mentioned features observed by ARPES suggest that paired electrons in the dSC phase have additional correlations. Since deviations of the quasiparticle properties of SC cuprates from BCS mean-field (MF) theory are more pronounced near the Mott insulating state and that the undoped insulators are well described by the Heisenberg model with $J > 0$ [29] short-range AF correlations are a natural candidate. Superconductivity is obtained upon doping the parent insulating compounds, which are Heisenberg antiferromagnets, and thus is expected to fall within the generalized-tJ model realm [26, 32]. This model describes vacancies hopping in a background of antiferromagnetically correlated spins. Given that AF correlations frustrate the motion of vacancies, these modify spin correlations and drive the system into the dSC state. The "doped carrier" MF theory accounts for vacancies surrounded by both staggered moment and d-wave spin singlet correlations and, in this chapter, we find reproduces the effect of strong electron correlations on both the single electron dispersion and quasiparticle spectral weight in consonance with ARPES experiments on cuprate superconductors. This agreement follows from the fact that hole dynamics is determined by the configuration of spins encircling the vacancy and offers support for the relevance of AF short-range correlations in superconductors neighbored by the Mott insulating transition.

The structure of this chapter is as follows. In Sec. 5.2 we review some recent experiments that study the doping evolution of the electron spectral function close to the insulating state and which motivate the present work. After that, in Sec. 5.3 we point out some shortcomings of the plain BCS and slave boson MF theories in addressing the spectral function as observed in the cuprates. We then focus on the "doped carrier" MF theory and explore how AF and dSC correlations conspire to yield a MF electron spectral function which we extensively compare to experimental data (Sec. 5.4). Finally, in Sec. 5.5 we discuss our results.

5.2 ARPES and the cuprates

In the course of the last almost 20 years both undoped, hole and electron doped cuprates have been heavily studied with a variety of experimental probes. Given the layered nature of these materials, ARPES has proved a highly valuable technique which provides both momentum and frequency resolved information concerning the microscopic electronic structure of the CuO2 planes [22]. ARPES measures the single electron spectral properties, from which the quasiparticle dispersion, quasiparticle lifetime and quasiparticle weight can be extracted. These features unveil not only the electronic character of excitations, but also the local correlations that determine the dynamics of electrons and holes. As an example take the role played by ARPES in establishing the validity of local moment physics in the undoped AF compounds [61] and the d-wave symmetry of electron pairs in the SC state [140]. Due to the recent improvement of experimental resolution and the quality of deeply underdoped samples, ARPES has also addressed the evolution of the electronic structure between the AF and SC phases [34, 112, 23, 24]. The resulting data provides crucial insights to understand the short-range correlations that develop in these materials, which lie at the heart of the cuprate underdoped regime problem. The central point of this chapter is to propose a theoretical interpretation of such data, which we briefly review in the remainder of this section.

5.2.1 Undoped materials

ARPES experiments have been conducted for several half-filled cuprates, like La_2CuO_4 [141], $Sr_2CuO_2Cl_2$ [113], $Ca_2CuO_2Cl_2$ [142], Nd_2CuO_4 [39] and Sm_2CuO_4 [143], with similar results in all cases. These experiments remove a photo-electron from the system and, therefore, probe the single hole dynamics in these materials. The observed electron spectrum captures various dispersive features at different energy scales as depicted in Fig. 5-1(a). The spectrum at low energy probes the dynamics of holes in the CuO_2 layers which have one valence electron per lattice site. The hole doped into the copper-oxide plane can be described by an effective three-band Hubbard model [144, 145]. However, both theoretical arguments [146] and experimental evidence [147, 148] show that it is energetically favorable for the hole doped in the oxygen valence band to form a singlet with the copper atom hole, which has become known as the Zhang-Rice singlet. The effective Hamiltonian that describes the hopping of this singlet in a two-dimensional lattice with a spin-1/2 in all occupied lattice sites corresponds to the generalized-tJ model [146]. Notably, the lowest energy dispersion in Fig. 5-1(a), which is separated from the remaining spectral features by more than 1eV, is well fit by theoretical estimates for the single hole dispersion in the $tt't''J$ model [46, 48, 109, 110] where all parameters can be estimated from band calculations, as detailed below.

Using the value $t \approx 400$meV for the nearest-neighbor (NN) hopping parameter, as obtained from band calculations [149, 111], and $J \approx 130$meV, as determined both from band calculations [149] and from fitting Raman scattering [150] and neutron scattering [151] experiments, the tJ model reproduces the above low energy exper-

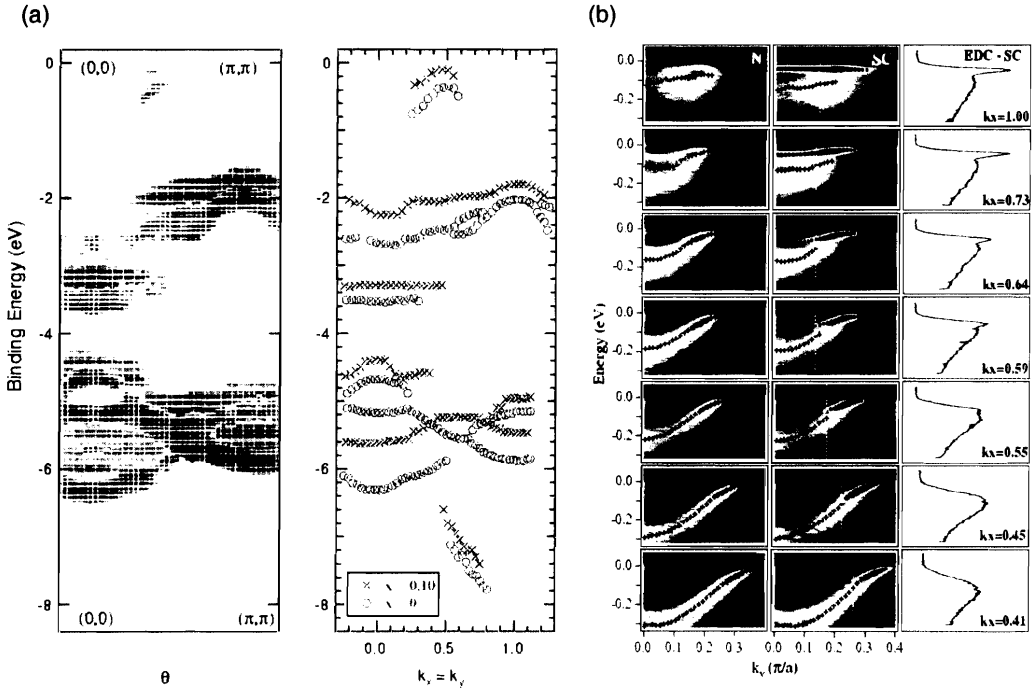

Figure 5-1: (a) Experimental ARPES data from Ref. [34]. Valence band comparison of $Ca_2CuO_2Cl_2$ and 10% Na-doped CCOC. The left panel plots the second derivative of the energy distribution curves, retaining only points with negative curvature. The right panel maps the dispersion of these features. Close to zero binding energy a dispersion consistent with that of a single hole in the $tt't''J$ model is observed. This dispersion is present even in the superconducting $x = 0.10$ NaCCOC sample. In fact, the main difference between the $x = 0$ and $x = 0.10$ spectra results from a chemical potential shift. (b) Experimental ARPES data from Ref. [135]. $T = 140$K normal (left panel) and $T = 40$K superconducting (middle panel) state ARPES intensity. Measurements taken on a $T_c = 89$K optimally doped Bi2212 sample. The SC state energy distribution curves from the momenta indicated by the vertical dashed lines in the middle panels are shown in the right panel. Data taken along Brillouin zone cuts where k_x is indicated in the right panels and k_y changes as indicated in the horizontal axis in the left and middle panels.

imental dispersion along $(0,0)-(\pm\pi,\pm\pi)$ [46, 30]. Since $t \approx 3J$ holes move faster than the spins which have to adjust to the hole motion and, as such, the tJ model band width is renormalized to $\approx 2.2J \approx 300$meV in accordance with experiments [34, 112, 24, 22, 61, 113, 53]. In case the 2^{nd} and 3^{rd} NN hopping parameters are set to vanish, *i.e.* $t' = t'' = 0$, the tJ model dispersion along $(0,\pi)-(\pi,0)$ is very flat [46, 61, 30], in contrast with the aforementioned experimental band whose dispersion between $(\frac{\pi}{2},\frac{\pi}{2})$ and $(0,\pi)$ is of order J [22, 61]. t' and t'' control intra-sublattice hopping processes and, as such, they are not strongly renormalized by the spin background AF correlations. Therefore, one would naively use $t' \approx -2t''$ of order J to fit the experimental dispersion along $(0,\pi)-(\pi,0)$ since the corresponding tight-binding contribution to the dispersion, namely $4t'\cos k_x \cos k_y + 2t''(\cos 2k_x + \cos 2k_y)$, disperses along $(0,\pi)-(\pi,0)$ but not along $(0,0)-(\pi,\pi)$. In fact, band calculations do estimate $t' \approx -2t'' \approx -J$ [111]. Interestingly, the values of t' and t'' are predicted by band theory to differ for different cuprate families [111] in consonance with the observed changes in the dispersion along $(0,\pi)-(\pi,0)$ between these same families [53]. All the above facts constitute strong evidence for the applicability of the $tt't''J$ model within the present context.

5.2.2 Hole doped materials

The undoped parent compounds are insulators due to strong interactions and display long-range AF order while, upon doping, these materials become d-wave superconductors. The dispersion of the half-filled system is of $d_{x^2-y^2}$-wave symmetry since its energy is higher at $(0,\pi)$ and $(\pi,0)$ than at $(\frac{\pi}{2},\frac{\pi}{2})$. Therefore, one could suspect it evolves into the $d_{x^2-y^2}$-wave dispersion of the SC Bogoliubov quasiparticles. This scenario turns out to be countered by experimental evidence regarding both data close to the Brillouin zone (BZ) boundary and data around the nodal direction.

We first refer to the former case and, in particular, we focus on the spectral line shape at $(0,\pi)$ which is very broad and, for undoped samples, peaks around 300meV. The maximum of this spectral hump is observed to decrease continuously in energy as materials are doped away from half-filling [22, 53], however, it does not match the SC gap energy defined by the peak at $(0,\pi)$ in the SC state. Instead, this peak develops at the leading edge midpoint energy [155, 156]. Hence, the $(0,\pi)$ spectrum naturally defines two different energy scales which became known as the high energy pseudogap (the energy at the hump maximum) and the low energy pseudogap (the leading edge midpoint energy) [157]. As shown in Fig. 5-2(a), these energy scales differ by a factor of $\times 4$, indicating that the dispersion from the AF insulators does not evolve into that of the SC quasiparticles. We can even argue that the high energy pseudogap scale is unrelated to superconductivity. Indeed, experiments show this energy scale changes for different materials in accordance with band theory estimates for t' and t'' [53] and the naive tight-binding argument presented in Sec. 5.2.1. Additional evidence for the connection between the aforementioned high energy band and short-range AF correlations comes from ARPES data showing it disperses along the perpendicular directions $(0,\pi)-(0,0)$ and $(0,\pi)-(\pi,\pi)$ in similar ways [152].

Notably, the U-shaped dispersion along the diagonal direction in undoped ma-

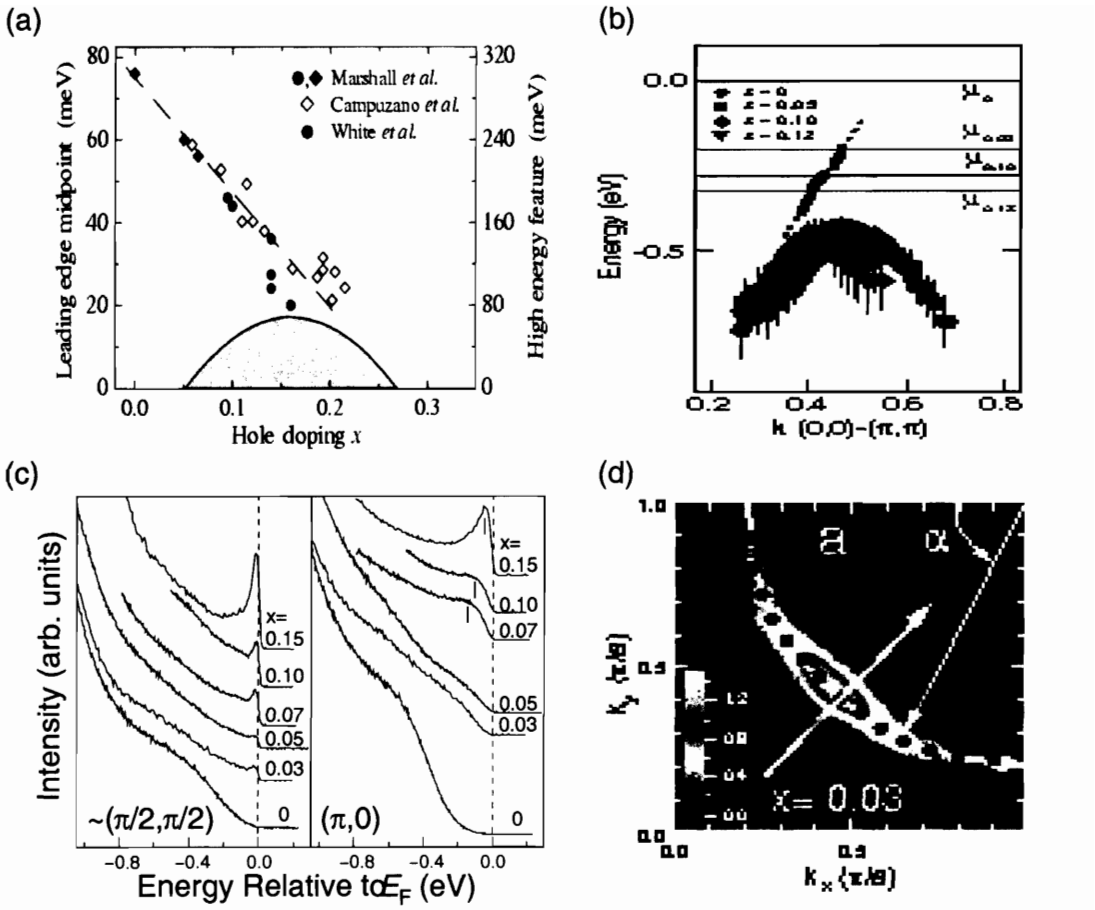

Figure 5-2: Experimental figures taken from (a) Ref. [22], (b) Ref. [24], (c) and (d) Ref. [23]. (a) Doping dependence of the pseudogap magnitude as determined from the leading edge midpoint (circles, left axis) and the hump energy (diamonds, right axis) in the $(\pi, 0)$ spectra of Bi2212. The data used in this plot is extracted from Refs. [152, 153, 154]. (b) Schematic representation of the two nodal dispersive features observed in $x = 0$, $x = 0.05$, $x = 0.10$ and $x = 0.12$ NaCCOC. These include the high energy hump, identified both in the antiferromagnetic $x = 0$ sample and in the superconducting $x = 0.10$ and $x = 0.12$ samples, and the linear dispersion that crosses the Fermi level close to $(\pi/2, \pi/2)$ and whose spectral intensity vanishes with underdoping. (c) LSCO ARPES spectra taken at the nodal point (left panel) and at $(\pi, 0)$ (right panel) at various doping levels. Notice that a small peak feature appears at the nodal point close to the Fermi energy right at $x = 0.03$. The $(\pi, 0)$ spectra only show a low energy peak at much higher doping. The clear difference between the nodal and antinodal spectra has been coined the "nodal-antinodal dichotomy" [31], which is sharper in the more underdoped compounds. (d) The spectral weight at the Fermi energy for $x = 0.03$ LSCO plotted in momentum space displays the above dichotomy in terms of a low energy spectral weight arc around the nodal direction.

terials is resolved by experiments even in doped compounds with SC long-range order [34, 24]. It is observed at energies higher than the Fermi energy and continues smoothly into the dispersion of AF samples, as shown in Figs. 5-1(a) and 5-2(b). On the other hand, a low energy band that disperses linearly across the Fermi level along the nodal direction emerges in doped compounds [24], as depicted in Fig. 5-2(b). This dispersion, whose spectral peaks develop above the AF band as the CuO_2 layers are doped away from half-filling, is characteristic of $d_{x^2-y^2}$-wave superconductors. The above experimental evidence is observed both in NaCCOC [34, 24] and LSCO [112, 23] and suggests the existence of states inside the Mott gap that lose spectral weight as the insulator is approached.

The spectral function of hole underdoped samples thus suggests that the AF and $d_{x^2-y^2}$-wave dispersions coexist at different energies: while the former, defined by the high-energy spectral hump, fades away as the density of doped holes increases, the latter loses its spectral intensity as the doping level vanishes. The existence of these two dispersive features argues in favor of the presence of both AF and dSC short-range correlations in cuprate superconductors, as described by the "doped carrier" MF theory.

Evidence for two spectral dispersions is identified along the different directions in momentum space and defines a new energy scale, namely the one that separates both features [135]. This is the dip energy that intervenes between the low energy quasiparticle peaks and the high energy spectral hump and, as seen in Fig. 5-1(b), it occurs at $\approx 70\text{meV} \approx \frac{J}{2}$. As documented by experiments, a kink appears in the momentum distribution curve derived dispersion at the dip energy scale [31, 34, 134]. In the literature, this kink is considered to be a manifestation of a bosonic mode whose nature has been the topic of vivid debate in recent years [133, 22, 134, 158, 135]. In the context of the present work, the kink derives from the coexistence of two distinct short-range correlations, each manifested in separate energy ranges.

An additional remarkable feature displayed by ARPES measurements in underdoped samples has to do with the strong momentum dependence of the spectral weight distribution [34, 31, 112, 23, 35]. Above we refer to experimental data showing the development of peaks close to the Fermi level upon hole doping. The same experiments also show that these peaks appear first in the nodal direction and are only observed close to the antinodes at higher hole densities [23] [see Fig. 5-2(c)]. As a result, the low energy spectral weight forms arcs around the nodal direction [Fig. 5-2(d)], as observed in various materials [34, 112, 23]. This anisotropy in momentum space, which consists in the robustness of nodal quasiparticles almost into the insulator regime and the rapid loss of antinodal quasiparticle coherence upon decreasing hole doping, became known as the nodal-antinodal dichotomy, and is consistent with a diversity of experimental observations: while tunneling evidence for quasiparticle interference effects [15], thermal conductivity [12] and c-axis penetration depth measurements [16] support the survival of nodal excitations in the deeply underdoped regime, the absence of coherent peaks in tunneling data [159, 36, 160, 42] of underdoped samples indicates that quasiparticles close to the BZ boundary are incoherent in the same limit; Raman scattering [161], optical transient grating spectroscopy [162], c-axis penetration depth [163], optical conductivity [37] and c-axis resistivity

[38] measurements are all consistent with anisotropic scattering processes; the disparity between different critical magnetic fields in the cuprate materials suggests orbital and Zeeman coupling in the nodal and antinodal regions respectively [138, 139]. Furthermore, all the experimental evidence supports that this dichotomy is sharper in more underdoped samples.

5.2.3 Electron doped materials

Despite less studied, electron doped cuprates like Ce doped Nd_2CuO_4 [39, 164, 165], $PrLaCuO_4$ [166] and Sm_2CuO_4 [143] have also been analyzed by ARPES. Since this experimental probe measures the spectral features concerning occupied electronic states, in electron doped materials ARPES identifies both the lower Hubbard band, which is approximately 1.3eV below the Fermi energy [39], and the bottom of the upper Hubbard band, which is intercepted by the chemical potential. As a result, near half-filling doped electrons form pockets around $(0, \pi)$ and $(\pi, 0)$ [39]. This state of affairs is to be contrasted with that of hole underdoped materials, in which case the spectral signature of doped holes appears in the nodal region. This particle-hole asymmetry is well understood within the context of the $tt't''J$ model [48, 109, 167]: under a particle-hole transformation t' and t'' change signs; since $t' \approx -2t''$ control the dispersion along $(0, \pi) - (\pi, 0)$, changing the sign of these parameters switches the dispersion maximum and minimum between the wave-vectors $(\frac{\pi}{2}, \frac{\pi}{2})$ and $(0, \pi)$. The presence of electron pockets in these materials is consistent with the rigid filling of the upper Hubbard band in the AF state and is reproduced by numerical calculations of the $tt't''J$ model [48, 62]. Since AF long-range order survives up to $x \approx 0.10 - 0.14$ these spectral weight pockets are observed in a wide doping range [39, 165].

Given that, upon electron doping, the chemical potential shifts to the bottom of the upper Hubbard band ARPES has access to the full correlation gap and detects how the spectral weight is transfered from the lower Hubbard band into the mid-gap region close to the Fermi level. In particular, as the electron concentration is increased and these materials approach the SC state ARPES data shows the build up of spectral intensity around the nodal direction [39, 164, 165, 166, 143]. This spectral weight approaches the Fermi level upon doping and, in the SC phase, it defines the gapless Dirac dispersion characteristic of d-wave superconductors. Hence, the electron spectral function in SC samples consists of two different contributions at low energy: it displays the spectral features close to the BZ boundary that evolve continuously from the pockets at $(0, \pi)$ and $(\pi, 0)$ in the AF phase [39, 164, 165]; in addition, it shows the spectral weight that defines the nodal Bogoliubov quasiparticles. Within the "doped carrier" MF theory these contributions are evidence for both AF and dSC local correlations which, in the electron doped regime, manifest themselves in separate momentum space regions.

The coexistence of these short-range correlations is also believed to modify the momentum dependence of the SC gap. In pure $d_{x^2-y^2}$-wave superconductors the maximum gap occurs at the BZ boundary. However, ARPES data [166] and Raman spectroscopy measurements [168] show that the maximum value of the gap occurs between the nodal direction and the BZ boundary, close to the intersection with the

antiferromagnetic BZ boundary. The observed gap is well fit if higher harmonics consistent with d-wave symmetry are introduced. In fact, the SC gap is also known to deviate from the $\cos 2\theta_{\boldsymbol{k}}$ form in hole doped materials [169]. In Sec. 5.4.3 we propose such a deviation follows from the effect of short-range AF correlations in the dSC state.

5.3 Electron spectral function of superconductors

5.3.1 BCS mean-field spectral function

The BCS "reduced" Hamiltonian [3, 4] provides the simplest theory to describe a superconductor. It starts with the electron Fermi sea and adds the coherent particle-hole mixing that captures the essence of off-diagonal long-range order. Since it is quadratic in the electron creation and annihilation operators, $c^{\dagger}_{i,\sigma}$ and $c_{i,\sigma}$ respectively, it is trivially solved with the appropriate Slater determinant of Bogoliubov quasiparticles. The one electron Green's function, which in time and real space variables is defined to be

$$G_c(i,t) = -\langle T_t \left[c_{i,\sigma}(t) c^{\dagger}_{0,\sigma}(0) \right] \rangle \tag{5.1}$$

is then exactly computed as is the electron spectral function which, by definition, is

$$A(\boldsymbol{k},\omega) = -\frac{1}{\pi} \mathrm{Im} G_c(\boldsymbol{k}, \omega + i0^+) \tag{5.2}$$

At MF level the above spectral function reduces to the sum of two δ-peaks, one at negative and the other at positive energy:

$$A_{BCS}(\boldsymbol{k},\omega) = u^2_{\boldsymbol{k}} \delta\left(\omega - E_{\boldsymbol{k}}\right) + v_{\boldsymbol{k}} \delta\left(\omega + E_{\boldsymbol{k}}\right) \tag{5.3}$$

Here, $E_{\boldsymbol{k}} = \sqrt{\epsilon^2_{\boldsymbol{k}} + \Delta^2_{\boldsymbol{k}}}$ stands for the quasiparticle dispersion that results from opening the SC energy gap $\Delta_{\boldsymbol{k}}$ on top of the normal state dispersion $\epsilon_{\boldsymbol{k}}$. The coherence factors $u_k = \sqrt{\frac{1}{2}(1 + \frac{\epsilon_{\boldsymbol{k}}}{E_{\boldsymbol{k}}})}$ and $v_k = \mathrm{sgn}(\Delta_{\boldsymbol{k}}) \sqrt{\frac{1}{2}(1 + \frac{\epsilon_{\boldsymbol{k}}}{E_{\boldsymbol{k}}})}$ encode the coherent superposition of electrons and holes. These factors determine that the probability of a bare particle state with momentum $\boldsymbol{k}$ to be unoccupied or occupied is $u^2_{\boldsymbol{k}}$ and $v^2_{\boldsymbol{k}}$ respectively, and may differ from 0 or 1 due to the pairing interaction.

The MF spectral function (5.3) does not account for the finite level widths and for the continuum contributions that are present if we go beyond the quadratic MF level or as observed in experimental spectra. Still, the dispersion defined by the MF spectral function δ-peaks, as well as the associated spectral intensity, can be recognized in the ARPES spectrum of SC samples and, indeed, are considered fundamental evidence for the $d_{x^2-y^2}$ symmetry of the single particle spectral gap [22, 157]. Remarkably, in Ref. [11] both the particle and the hole branches of the electron spectral function are probed for overdoped Bi2223, finding good quantitative agreement between the coherence factors, above and below the Fermi energy and as a function of momentum, determined both from the spectral intensity and from the energy dispersion based

on BCS theory. This agreement strongly supports that low energy nodal excitations in cuprate superconductors are BCS Bogoliubov quasiparticles. Furthermore, it illustrates the relevance of MF approaches in describing spectral dispersions and the momentum space distribution of spectral intensity. In this context, let us recall that the main goal of the present chapter is precisely to propose a MF description of the spectral dispersions and the momentum space distribution of spectral intensity in the underdoped regime of cuprates. As mentioned above, in the underdoped limit several deviations from BCS theory are encountered. These include not only dispersion renormalization effects but also non-trivial patterns in the distribution of spectral weight in energy-momentum space, such as the sharp momentum space anisotropy and the vanishing of the spectral intensity of the SC d-wave dispersion as the system is brought closer to half-filling.

5.3.2 Slave boson mean-field spectral function

The discrepancy between BCS MF predictions and the electron spectral function in underdoped cuprates follows from the fact that BCS theory does not capture the proximity to the Mott insulator transition. In other words, BCS MF superconductors are conventional superconductors whereas underdoped cuprate superconductors are strongly correlated superconductors. The generalized-tJ model provides the simplest, albeit not simple at all, route to encode the physics of strong local interactions as of interest to the cuprates. A standard approach to describe the superconducting state in the context of this model is provided by the slave boson approximation, which we overview in Chapter 3.

In the slave boson approximation the projected electron operators $\mathcal{P}c_i\mathcal{P}$ are decomposed into spin-1/2 charge neutral spinon operators $\psi_i^\dagger = [\psi_{i,1}^\dagger \psi_{i,2}^\dagger]$ and charged spinless holon operators $h_i^\dagger = [h_{i,1}^\dagger h_{i,2}^\dagger]$ [Expression (3.10)]. While spinons are fermionic, holons are bosonic operators which Bose condense ($\langle h_i \rangle \neq 0$) at low temperature.

Even though the slave boson MF Hamiltonian (3.11) is quadratic the slave boson MF electron spectral function does not reduce to the sum of δ-peaks [57, 58] because the electron operator itself is decomposed into spinons and holons and the electron Green's function is recast as $G_e(i,t) = -\langle T_t \left[h_i^\dagger(t)\psi_i(t)h_0(0)\psi_0^\dagger(0) \right] \rangle$. At MF level spinons and holons do not interact and the above Green's function simplifies to the product of the holon and spinon Green's functions

$$G_e^{MF}(i,t) = -\langle T_t \left[h_i^\dagger(t)h_0(0) \right] \rangle \langle T_t \left[\psi_i(t)\psi_0^\dagger(0) \right] \rangle \tag{5.4}$$

At low temperature holons condense and (5.4) can be written as the sum of a coherent and an incoherent term [57, 58]. The former has the form

$$\tfrac{1}{2}\langle h_0 \rangle^2 G_f(i,t) \tag{5.5}$$

where $G_f(i,t)$ is the spinon Green's function. The latter mostly reflects the holon density of states [57].

Following the discussion in Sec. 5.3.1 we now focus on the coherent contribution (5.5) in order to compare to the spectral features of underdoped cuprates alluded to above. In the slave boson MF approach spinons are found to pair up in the d-wave channel. Therefore, in the presence of holon condensation, the coherent spectral function (5.5) shows well defined dSC quasiparticles. Since $\langle h_0 \rangle^2 \sim x$ the spectral intensity associated with the d-wave dispersion vanishes with underdoping, once again in agreement with ARPES results [34, 24]. In contrast with the experimentally observed nodal-antinodal anisotropy, though, the MF spectral weight distribution in momentum space is uniform. Additionally, for the tJ model, the spectral weight at the nodes is expected to be numerically larger than x [170, 171, 172, 173]. In the $SU(2)$ MF theory, however, this weight is $\frac{\langle h_0 \rangle^2}{2} \leq \frac{x}{2}$ [58].

In the absence of double electron occupancy, a simple state counting argument requires [174] $\langle c_{i,\sigma} c_{i,\sigma}^\dagger \rangle = x$ and $\langle c_{i,\sigma}^\dagger c_{i,\sigma} \rangle = \frac{1-x}{2}$ for each spin direction σ (in the absence of overall magnetization). Yet, for $\langle h_0 \rangle^2 = x$ the $SU(2)$ MF theory yields $\langle c_{i,\sigma} c_{i,\sigma}^\dagger \rangle = \frac{x(1+x)}{4}$ and $\langle c_{i,\sigma}^\dagger c_{i,\sigma} \rangle = \frac{1}{2} + \frac{x(1-x)}{4}$. Hence, despite correctly yielding a total spectral weight equal to $\frac{1+x}{2}$, away from half-filling the MF slave boson approach violates the sum rule that determines the occupied and the unoccupied part of the spectral weight [57].

We remark that some of the above results change if the $U(1)$ slave boson formulation [75] is considered instead. In particular, the coherent spectral weight at the nodes is $\langle h_0 \rangle^2 \leq x$ and, for $\langle h_0 \rangle^2 = x$ we find $\langle c_{i,\sigma} c_{i,\sigma}^\dagger \rangle = \frac{x(1+x)}{2}$ and $\langle c_{i,\sigma}^\dagger c_{i,\sigma} \rangle = \frac{1-x^2}{2}$. Interestingly, these MF results for the spectral function improve over the $SU(2)$ formulation ones and hint at the important role of gauge fluctuations in binding spinons and holons into holes. In fact, the above weaknesses of the slave boson MF approach are healed if the coupling between spinons, holons and gauge fluctuations would be properly considered [32, 57, 58, 64]. The "doped carrier" formulation of the generalized-tJ model includes hole-like objects even at MF level and, in the remainder of this chapter, we show it overcomes the above problems and reproduces many other features displayed by ARPES data.

5.4 Doped carrier mean-field electron spectral function

In Chapter 4 we introduce the "doped carrier" MF theory of the $tt't''J$ model which is consistent with the observed phase diagram of both hole and electron doped cuprates. This theory describes the physical degrees of freedom in terms of spinons and dopons. The former are spin-1/2 excitations of the spin background. Dopons correspond to doped carriers in the deeply underdoped limit. More specifically, they describe vacancies surrounded by staggered local moments. Upon mixing with spinons, dopons can also account for vacancies surrounded by singlet spin configurations that enhance the vacancy mobility. Therefore, the "doped carrier" MF theory captures the interplay between different local spin correlations and the single hole dynamics which, ultimately, is translated into the electron spectral function. The purpose of this section

is to compute the "doped carrier" MF electron spectral function, to address how AF and dSC short-range correlations are reflected in the spectral properties of superconducting electrons close to the Mott insulating state and to compare our results to ARPES data from hole and electron doped cuprates. The difference between the hole and electron doped regimes comes from using different 2^{nd} and 3^{rd} NN effective hopping parameters, namely t_2 and t_3 in (4.27) correspond to the hole doped case and those in (4.28) to the electron doped one. For notational and other formal details we refer the reader to Chapter 4 where the "doped carrier" theory is introduced.

5.4.1 Mean-field electron operator

To compute the spectral function (5.2) requires the knowledge of the electron operators c_i and $c_i^\dagger$. In Appendix 5.6 we derive the expression for these operators in the fermionic representation of the enlarged Hilbert space (4.2). In the hole doped regime, (5.17) is the operator that acts on physical states as the electron destruction operator and that vanishes for all unphysical states. This same operator is interpreted as the electron creation operator in the electron doped regime.

(5.17) is a multi-fermionic operator and, therefore, the exact calculation of (5.2) is not a trivial task. For that reason we drop the projection operators $\widetilde{\mathcal{P}}$ and introduce fermionic averages to reduce (5.17) to a single fermionic operator. The resulting MF electron operator is

$$\begin{aligned} c_{i,\sigma}^{MF} &= \frac{1}{\sqrt{2}}\left(d_{i,-\sigma}^\dagger \langle f_{i,\sigma}^\dagger f_{i,\sigma} f_{i,-\sigma} f_{i,-\sigma}^\dagger\rangle + f_{i,-\sigma}^\dagger \langle d_{i,\sigma}^\dagger f_{i,\sigma}\rangle\right) \\ &= \frac{1}{\sqrt{2}}\left(d_{i,-\sigma}^\dagger + b_0 f_{i,-\sigma}^\dagger\right) \end{aligned} \tag{5.6}$$

Using the notation from Appendix 5.6 it is easy to realize that the above expression captures the two orthogonal ways to dope site i. The undoped site i with a $\widetilde{S}_z = +\frac{1}{2}$ lattice spin is represented by $|\uparrow\rangle_i^{phys} = f_{i,\uparrow}^\dagger |0\rangle_i^{enl}$. To dope such a site we can: (i) act with the dopon operator $d_{i,\downarrow}^\dagger$, which creates the state $d_{i,\downarrow}^\dagger f_{i,\uparrow}^\dagger |0\rangle_i^{enl}$ whose overlap with $|0\rangle_i^{phys}$ is $\frac{1}{\sqrt{2}}$ or (ii) allow the spinon $f_{i,\uparrow}^\dagger$ to turn into a dopon $d_{i,\uparrow}^\dagger$ with a transition amplitude $b_0^* = b_0$ and then act with the spinon operator $f_{i,\downarrow}^\dagger$, which creates the state $f_{i,\downarrow}^\dagger d_{i,\uparrow}^\dagger |0\rangle_i^{enl}$ whose overlap with $|0\rangle_i^{phys}$ is also $\frac{1}{\sqrt{2}}$.

To further motivate the form of the MF electron operator (5.6) we check the negative and positive energy spectral weight sum-rules alluded to in Sec. 5.3.2. Making use of the relations

$$\begin{aligned} \langle d_{i,-\sigma}^\dagger d_{i,-\sigma}\rangle &= 1 - \langle d_{i,-\sigma} d_{i,-\sigma}^\dagger\rangle = \frac{x}{2} \\ \langle f_{i,-\sigma}^\dagger d_{i,-\sigma}\rangle &= \langle d_{i,-\sigma}^\dagger f_{i,-\sigma}\rangle = b_0 \\ \langle f_{i,-\sigma}^\dagger f_{i,-\sigma}\rangle &= \langle f_{i,-\sigma} f_{i,-\sigma}^\dagger\rangle = \frac{1}{2} \end{aligned} \tag{5.7}$$

it is a trivial matter to show that

$$\langle c_{i,\sigma}^{MF}\left(c_{i,\sigma}^{MF}\right)^{\dagger}\rangle = \frac{x+3b_0^2}{4}$$
$$\langle\left(c_{i,\sigma}^{MF}\right)^{\dagger} c_{i,\sigma}^{MF}\rangle = \frac{2-x-b_0^2}{4} \tag{5.8}$$

In the case of full coherence $b_0 = \sqrt{x}$. Then, the expressions in (5.8) reduce to $\langle c_{i,\sigma}^{MF}\left(c_{i,\sigma}^{MF}\right)^{\dagger}\rangle = x$ and $\langle\left(c_{i,\sigma}^{MF}\right)^{\dagger} c_{i,\sigma}^{MF}\rangle = \frac{1-x}{2}$. These are the correct expressions for the $tt't''J$ model [174].

5.4.2 Mean-field electron spectral function

For a number of different reasons, in this chapter we only consider the $T = 0$ MF electron spectral function. Firstly, the nature of the approximations incurred in the derivation of the present MF theory are valid in the low temperature regime (see Chapter 4). Secondly, the MF spectral function is calculated with the MF electron operators (5.6), which overlook the multi-fermionic structure of the exact operators (5.17) and, thus, miss the structure of the incoherent spectral weight, whose relevance increases with that of thermal fluctuations. Finally, the main goal of this chapter is to address the spectral properties of the SC state near the Mott transition.

At $T = 0$ the MF spectral function is a collection of δ-peaks at the eigenenergies of H_{tJ}^{MF} in (4.22) [or H_{AF}^{MF} in (4.30) for the case of the AF phase] whose strength is determined by the eigenvectors of the same Hamiltonian. In particular, the MF Hamiltonian (4.22) can be recast in its diagonalized form as

$$H_{tJ}^{MF} = \# + \sum_{\boldsymbol{k}} \Phi_{\boldsymbol{k}}^{\dagger} \begin{bmatrix} \epsilon_{1,\boldsymbol{k}}^{+}\sigma_z & 0 \\ 0 & \epsilon_{2,\boldsymbol{k}}^{+}\sigma_z \end{bmatrix} \Phi_{\boldsymbol{k}} \tag{5.9}$$

where $\Phi_{\boldsymbol{k}}^{\dagger} = \left[\left(\phi_{1,\boldsymbol{k}}^{+}\right)^{\dagger}\left(\phi_{1,\boldsymbol{k}}^{-}\right)^{\dagger}\left(\phi_{2,\boldsymbol{k}}^{+}\right)^{\dagger}\left(\phi_{2,\boldsymbol{k}}^{-}\right)^{\dagger}\right]$ are linear combinations of the Nambu operators $\psi_{\boldsymbol{k},\alpha}$ and $\eta_{\boldsymbol{k},\beta}$ such that $(\phi_{l,\boldsymbol{k}}^{s})^{\dagger}$ with $l \in \{1,2\}$ and $s \in \{+,-\}$ creates the MF quasiparticle eigenstate with momentum $\boldsymbol{k}$ and eigenenergy $\epsilon_{l,\boldsymbol{k}}^{s}$. Using the above notation the $T = 0$ MF groundstate is $|GS\rangle_{MF} = \left[\Pi_{\boldsymbol{k}}\left(\phi_{1,\boldsymbol{k}}^{-}\right)^{\dagger}\left(\phi_{2,\boldsymbol{k}}^{-}\right)^{\dagger}\right]|0\rangle^{N}$, where $|0\rangle^{N}$ is the vacuum for the Nambu operators $\psi_{\boldsymbol{k},\alpha}$ and $\eta_{\boldsymbol{k},\beta}$. Hence, the $T = 0$ MF spectral function is

$$A(\boldsymbol{k},\omega) = \sum_{\substack{l\in\{1,2\}\\ s\in\{+,-\}}} Z_{l,\boldsymbol{k}}^{s}\,\delta\left(\omega - \epsilon_{l,-\boldsymbol{k}}^{s}\right) \tag{5.10}$$

in the hole doped case and

$$A(\boldsymbol{k}+(\pi,\pi),\omega) = \sum_{\substack{l\in\{1,2\}\\ s\in\{+,-\}}} Z_{l,\boldsymbol{k}}^{s}\,\delta\left(\omega + \epsilon_{l,-\boldsymbol{k}}^{s}\right) \tag{5.11}$$

in the electron doped case. The wave vector (π,π) is added in (5.11) to make up for

the fact that under a particle-hole transformation the hopping parameters change sign and the dispersions are shifted in momentum space by (π, π). The spectral weight in each peak is given by

$$\begin{aligned} Z^s_{l,\boldsymbol{k}} &= \left| {}^N\langle 0| \left[\frac{1}{\sqrt{2}} \left(d^\dagger_{\boldsymbol{k},\downarrow} + b_0 f^\dagger_{\boldsymbol{k},\downarrow} \right) \right] \left(\phi^s_{l,-\boldsymbol{k}} \right)^\dagger |0\rangle^N \right|^2 \\ &= \frac{\frac{1+b_0^2}{2}}{1 + \frac{\left(\gamma_{\boldsymbol{k}}+\beta_{\boldsymbol{k}} b_0+\epsilon^s_{l,\boldsymbol{k}}\right)^2}{\left(\beta_{\boldsymbol{k}}-\gamma_{\boldsymbol{k}} b_0-\epsilon^s_{l,\boldsymbol{k}} b_0\right)^2} + \frac{(1+b_0)^2\left[\left(\epsilon^s_{l,\boldsymbol{k}}+\alpha^z_{\boldsymbol{k}}\right)\left(\epsilon^s_{l,\boldsymbol{k}}+\gamma_{\boldsymbol{k}}\right)-\beta^2_{\boldsymbol{k}}\right]^2\left[\left(\epsilon^s_{l,\boldsymbol{k}}-\gamma_{\boldsymbol{k}}\right)^2+\beta^2_{\boldsymbol{k}}\right]}{\left(\alpha^x_{\boldsymbol{k}}\right)^2\left(\epsilon^s_{l,\boldsymbol{k}}-\gamma_{\boldsymbol{k}}\right)^2\left[\beta_{\boldsymbol{k}}-b_0\left(\epsilon^s_{l,\boldsymbol{k}}+\gamma_{\boldsymbol{k}}\right)\right]^2}} \end{aligned} \tag{5.12}$$

5.4.3 Hole doped case

Dispersive features

In Fig. 5-3(a) we plot the four MF bands for $x = 0$ along the high symmetry directions. These are the d-wave paired spinon bands $\epsilon^{\pm}_{1,\boldsymbol{k}}$ and the dopon bands $\epsilon^{\pm}_{2,\boldsymbol{k}}$. The electron spectral function (5.10) vanishes for all the bands but $\epsilon^{-}_{2,\boldsymbol{k}}$ [see Fig. 5-3(b)], which is the lower Hubbard band and is consistent with the self-consistent Born approximation for the electronic dispersion in the undoped limit [46, 109, 110]. The upper Hubbard band is not present since these results apply to the $tt't''J$ model where $U \rightarrow \infty$.

Away from half-filling spinons and dopons mix and spectral weight is transfered from the $\epsilon^{-}_{2,\boldsymbol{k}}$ band to the lower energy $\epsilon^{\pm}_{1,\boldsymbol{k}}$ bands. Fig. 5-3(c) concerns the resulting SC phase with $x = 0.12$ and the evidence for particle-hole mixing is particularly clear around $(0, \pi)$. Note that this evidence disappears for $x = 0.25$, which concerns the Fermi liquid state [Fig. 5-3(d)].

The spinon-dopon hybridization leads to the appearance of spectral peaks above the insulating valence band, hence inside the Mott-Hubbard gap. This result is consistent with the experimental observation of in-gap spectral features whose weight vanishes in the parent insulator compound [34, 112, 23, 24]. Figs. 5-3(b)-5-3(d) also show that the low energy spectral weight in bands $\epsilon^{\pm}_{1,\boldsymbol{k}}$, which increases with x, is mostly transfered from the region around (π, π) and not from the region around $(0, 0)$. Physically, this fact reflects the weakening of local AF correlations with increasing hole concentration. Particularly in Fig. 5-3(d) we see the development of a conventional electronic band, crossed by the Fermi level at $\omega = 0$, as the signatures inherited from the AF insulator dispersion fade away.

As it is further discussed in Sec. 7.3, the spectral peak in the high energy $\epsilon^{-}_{2,\boldsymbol{k}}$ band is very sharp at MF level. However, beyond the MF approximation, the strong interaction between an electron in the $\epsilon^{-}_{2,\boldsymbol{k}}$ band and spinons in the $\epsilon^{-}_{1,\boldsymbol{k}}$ band provides the means for the electron to decay, for instance, into an electron plus a pair of spinons. Inclusion of these processes would, therefore, broaden the $\epsilon^{-}_{2,\boldsymbol{k}}$ band.

Figs. 5-4(a)-5-4(c) focus on the evolution of the spectral function along the nodal direction between the undoped insulator and the overdoped Fermi liquid with a large Fermi surface. As holes are introduced in the undoped system the dispersion characteristic of the AF insulator persists at high energy, while a second spectral feature

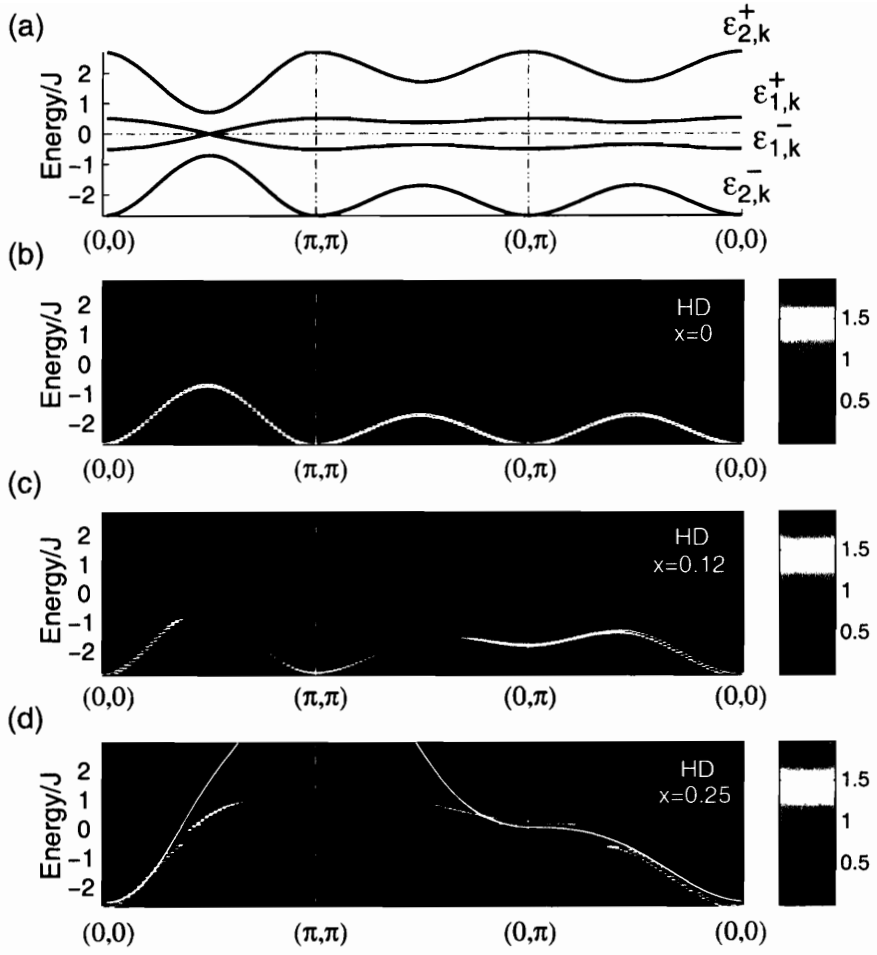

Figure 5-3: Energy dispersions along $(0,0)-(\pi,\pi)-(0,\pi)-(0,0)$ at different hole doping levels. (a) MF dispersions $\epsilon^{\pm}_{1,\boldsymbol{k}}$ and $\epsilon^{\pm}_{2,\boldsymbol{k}}$ for $x=0$. In this case, $\epsilon^{\pm}_{1,\boldsymbol{k}}$ stand for the spinon bands and $\epsilon^{\pm}_{2,\boldsymbol{k}}$ for the dopon bands. (b)-(d) show the MF electron spectral function (5.10) with Lorentzian broadening $\Gamma = J/10$ for $x=0$, $x=0.12$ and $x=0.25$ respectively. The solid white line in (d) plots the tight-binding dispersion $-2[t(\cos k_x+\cos k_y)+2t'\cos k_x\cos k_y+t''(\cos 2k_x+\cos 2k_y)+2t'''(\cos 2k_x\cos k_y+\cos 2k_y\cos k_x)+2t''''\cos 2k_x\cos 2k_y]-\mu$ with $t=148.8$meV, $t'=-40.9$meV, $t''=13.0$meV, $t'''=14.0$meV and $t''''=-12.7$meV as obtained from the fitting to the experimental energy dispersions in Ref. [175]. We chose μ to obtain $x=0.25$ and use $J=130$meV.

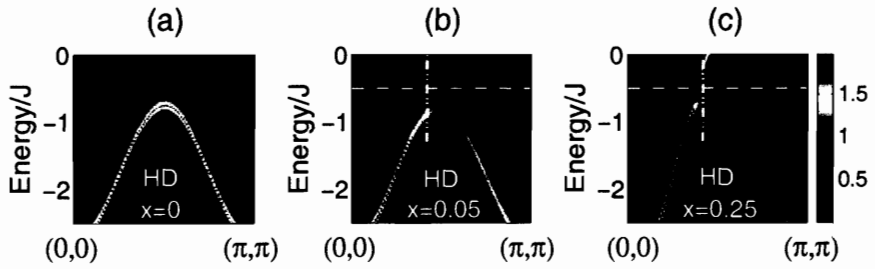

Figure 5-4: Nodal direction electron spectral function (5.10) with Lorentzian broadening $\Gamma = J/10$ for doped hole density (a) $x = 0$, (b) $x = 0.05$ and (c) $x = 0.25$. The presence of two spectral features leads to a peak-dip-hump spectral structure along the vertical white dashed line in (b) and (c). The horizontal white dashed line in (b) and (c) indicates the energy $\omega = J/2$ which lies at the dip energy and at which the nodal dispersion kink is observed (see main text).

emerges at low energy. The former disperses back in energy for momenta beyond $(\frac{\pi}{2}, \frac{\pi}{2})$, whereas the latter disperses linearly across the Fermi level ($\omega = 0$) close to $(\frac{\pi}{2}, \frac{\pi}{2})$, as seen in ARPES experiments [24]. Fig. 5-5(a) shows that the nodal point deviates from $(\frac{\pi}{2}, \frac{\pi}{2})$ toward $(0, 0)$. At low doping the Fermi point evolves linearly with x and, for $x > 0.10$ it remains around $k_x, k_y = 0.45\pi$. A similar pattern is observed experimentally in different cuprate families [31, 136, 24, 176].

In doped band insulators the chemical potential falls on top of the valence band and moves with doping in accordance with conventional rigid band filling of hole pockets. This picture is to be contrasted with the non-trivial behavior that follows the hybridization of spinons and dopons. In this case, the chemical potential remains in the insulating gap and, consequently, a new energy scale $\omega \approx \frac{J}{2}$ marked by the horizontal white dashed line in Figs. 5-4(b) and 5-4(c) appears. It separates the low energy dispersion reminiscent of the underlying SC correlations from the high energy spectral feature that reflects the local AF correlations which survive even in the absence of long-range AF order. We remark that such an energy scale is observed throughout the BZ [135] not only in underdoped samples [112, 24, 134] but also in overdoped materials [177].

Low energy spectral arcs

The absence of hole Fermi pockets with area x raises the question of where in momentum space the hole density comes from and, in Figs. 5-6(a) - 5-6(c), we depict the doping evolution of the electron momentum distribution $n_{\boldsymbol{k}} = \int_{-\infty}^{0} d\omega A(\boldsymbol{k}, \omega)$. At low doping most of the spectral weight comes from a small region around $(\frac{\pi}{2}, \frac{\pi}{2})$ and, in that sense, resembles the hole pocket scenario. More generally, the doping induced changes in $n_{\boldsymbol{k}}$ occur beyond the minimum gap locus, denoted by the black dashed line in Figs. 5-6(a) - 5-6(c), toward (π, π). By definition, this locus identifies the momentum vector $\boldsymbol{k}$ where the d-wave gap is lower along the direction defined by θ in Fig. 5-6(d). The variation of $n_{\boldsymbol{k}}$ across the minimum gap locus is particularly

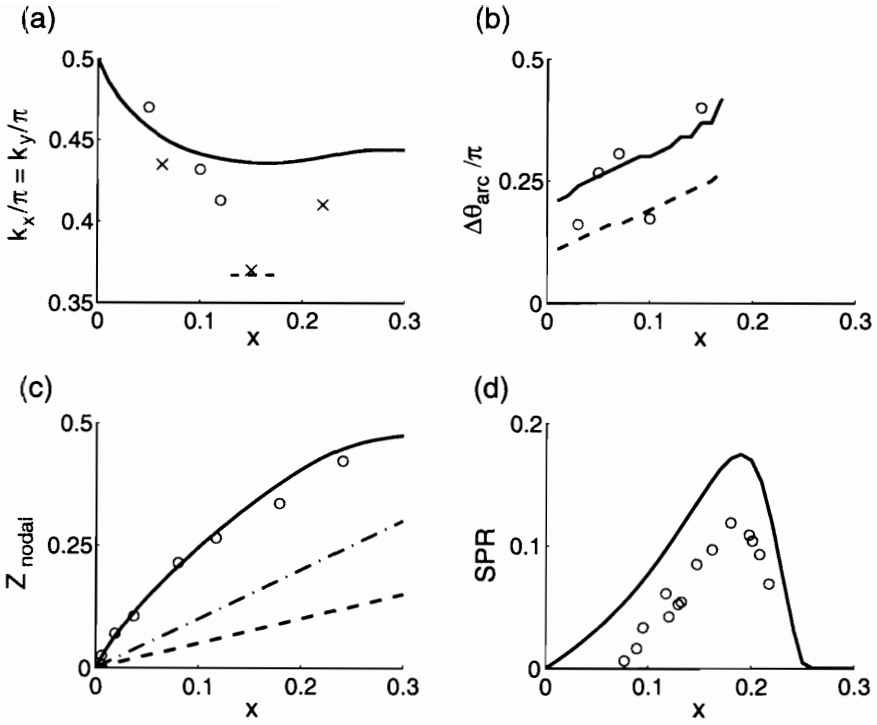

Figure 5-5: (a) MF theory results for the hole doping dependence of the nodal point location along the $(0,0)-(\pi,\pi)$ direction (solid line). Comparison to BSCCO [176] (dashed line), LSCO [31, 136] ($\times$) and NaCCOC [24] ($\circ$) results. (b) Low energy spectral weight arc length $\Delta\theta_{arc}$ as measured by the full angular width at half spectral weight maximum along minimum gap locus (solid line) and maximum spectral weight locus (dashed line). Comparison to LSCO results [23] ($\circ$). We only plot results up to $x = 0.17$, at which point the minimum gap locus changes from hole to electron topology. (c) Hole doping dependence of nodal spectral weight Z_{nodal} in the "doped carrier" MF theory (solid line), the $U(1)$ slave boson MF theory (dash-dot line) and the $SU(2)$ slave boson MF theory (dashed line). Comparison to variational Monte Carlo results for the tJ model with $t = 3J$ [171] ($\circ$). (d) SC peak ratio (SPR), *i.e.* the relative intensity of the spectral function peak at $(0,\pi)$, as given by the theoretical ratio $Z^-_{1,(0,\pi)}/(Z^-_{1,(0,\pi)} + Z^-_{2,(0,\pi)})$ (solid line) and as measured in BSCCO [177, 178] ($\circ$).

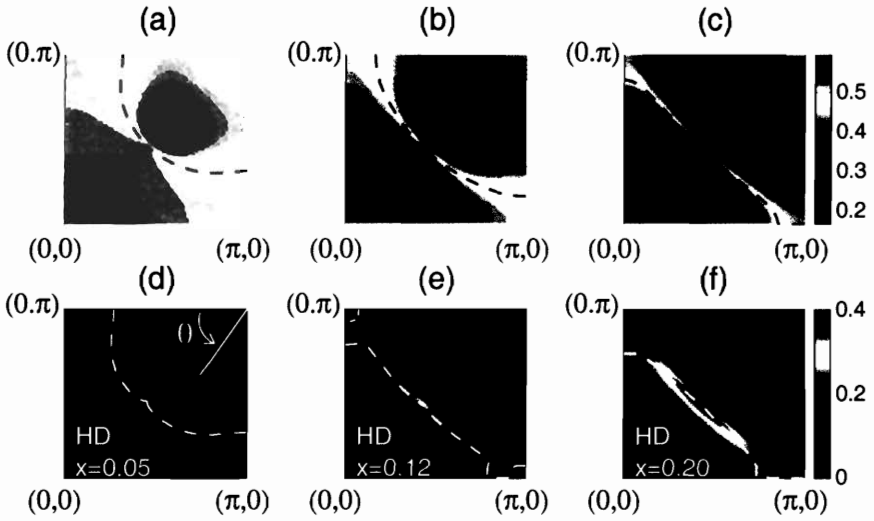

Figure 5-6: (a)-(c) Electron momentum distribution $n_{\boldsymbol{k}} = Z^{-}_{1,\boldsymbol{k}} + Z^{-}_{2,\boldsymbol{k}}$ (top color scale). The black dashed line depicts the minimum gap locus. (d)-(f) Electron spectral weight $Z^{-}_{1,\boldsymbol{k}}$ of the $\epsilon^{-}_{1,\boldsymbol{k}}$ band states (bottom color scale). The white dashed line represents the maximum spectral weight locus. Doped hole density is $x = 0.05$ for (a) and (d), $x = 0.12$ for (b) and (e), and $x = 0.20$ for (c) and (f).

sharp in the overdoped regime [see Fig. 5-6(c) where $x = 0.20$] as expected from the proximity to the Fermi liquid regime.

The electron momentum distribution integrates the spectral function in energy space and, as such, misses the momentum space structure of the spectral weight transfered from the high energy $\epsilon^{-}_{2,\boldsymbol{k}}$ band to the $\epsilon^{-}_{1,\boldsymbol{k}}$ band. In Figs. 5-6(d) - 5-6(f) we plot $Z^{-}_{1,\boldsymbol{k}}$, the spectral weight of states in the latter band. We find that it forms arcs of low energy spectral weight around the nodal direction as observed in LSCO [23] and NaCCOC [34, 112]. The total spectral weight at low energy increases with x and, as a result, doping both elongates the arcs and increases the spectral intensity in that region of momentum space.

Figs. 5-7(a) - 5-7(c) specifically show how the spectral weight of the $\epsilon^{-}_{1,\boldsymbol{k}}$ band states changes along the minimum gap locus for different doping values. Clearly, at low energy, states along the diagonal direction $[(0,0) - (\pm\pi, \pm\pi)]$ have more spectral weight than those close to the BZ boundary. This fact is consistent with the experimental nodal-antinodal dichotomy, a term motivated by the observation that in underdoped cuprates quasiparticle features around the nodes are stronger than in the antinodal region. [31, 34, 112, 35]

The MF spectral function is singular at the Dirac point and, in particular, the $Z^{-}_{1,\boldsymbol{k}}$ plots along the minimum gap locus are discontinuous at $\theta = \frac{\pi}{4}$. Indeed, in Figs. 5-7(a) - 5-7(c) the spectral weight at the nodal point is denoted by the $(\times)$ symbol above the curve defined by the spectral weight at other $\boldsymbol{k}$ vectors along the minimum gap locus. Alternatively, we can define the maximum spectral weight locus which identifies the $\boldsymbol{k}$ vectors that maximize $Z^{-}_{1,\boldsymbol{k}}$ for each θ. This locus is plotted as the

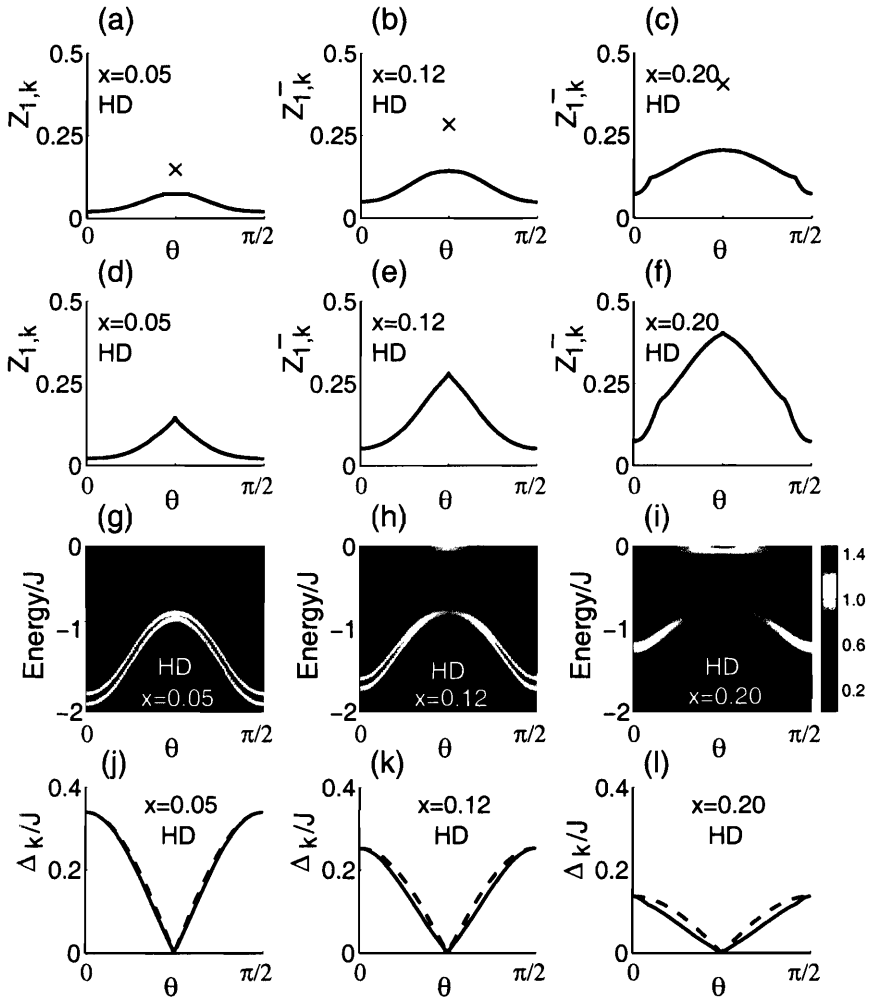

Figure 5-7: MF electron spectral function results for hole doping level $x = 0.05$ [(a),(d),(g) and (j)], $x = 0.12$ [(b),(e),(h) and (k)] and $x = 0.20$ [(c),(f),(i) and (l)]. (a)-(c) Electron spectral weight $Z^{-}_{1,\boldsymbol{k}}$ along minimum gap locus. The spectral weight is singular at $\theta = \pi/4$ and $Z^{-}_{1,\boldsymbol{k}}$ at the nodal point is depicted by the $\times$ symbol. (d)-(f) Electron spectral weight $Z^{-}_{1,\boldsymbol{k}}$ along maximum spectral weight locus. (g)-(i) Electron spectral function (5.10) along minimum gap locus. A Lorentzian broadening with $\Gamma = J/10$ is used. (j)-(l) $\epsilon^{+}_{1,\boldsymbol{k}}$ dispersion gap (solid line) and pure d-wave dispersion $[\Delta_{\boldsymbol{k}} = \Delta_0 \cos 2\theta_{\boldsymbol{k}}]$ with same gap magnitude (dashed line) along minimum gap locus. Note that the pure d-wave dispersion lies above $\epsilon^{+}_{1,\boldsymbol{k}}$ implying $B < 1$ (see main text). The angular variable θ used to parameterize the points along the minimum gap locus and the maximum spectral weight locus is defined in Fig. 5-6(d).

white dashed line in Figs. 5-6(d) - 5-6(f) and differs slightly from the the minimum gap locus [plotted in Figs. 5-6(a) - 5-6(c)]. The $Z^{-}_{1,\boldsymbol{k}}$ plot along the maximum spectral weight locus is continuous across $\theta = \frac{\pi}{4}$ and also displays the dichotomy between the nodal and antinodal regions [Figs. 5-7(d) - 5-7(f)].

An interesting question has to do with the doping evolution of the arcs. To quantify the doping dependence of the arc length ($\Delta\theta_{arc}$) we consider the full angular width at half maximum of the $Z^{-}_{1,\boldsymbol{k}}$ plots along both the minimum gap locus and the maximum spectral weight locus. In Fig. 5-5(b) we see that both definitions of arc length are consistent with two facts: (i) the arc length is finite in the zero doping limit and (ii) the low energy spectral arcs extend away from the nodal direction with increasing hole density. However, we find that the quantitative estimate of the spectral arc length depends sensitively on whether we chose the minimum gap or the maximum spectral weight locus. Interestingly, in Fig. 5-5(b) we compare both theoretical estimates with the arc length values deduced from Fig. 2(c) of Ref. [23] to find quantitative agreement between the MF results and the spread and doping dependence of experimental data.

Figs. 5-6(d) - 5-6(f) and 5-7(a) - 5-7(f) demonstrate that the spectral weight intensity also increases with doping level. In Fig. 5-5(c) we plot the doping evolution of the nodal spectral weight. It falls linearly to 0 as $x \rightarrow 0$ but deviates from the pure straight line behavior displayed by the spectral weight in the slave boson MF approximation. In addition, nodal states in the "doped carrier" MF approach show enhanced quasiparticle behavior when compared to the results from slave boson MF theory. Fig. 5-5(c) also compares our results to those obtained in the variational Monte Carlo approach to the tJ model with $t = 3J$ [171], which implements the projection onto the tJ model Hilbert space exactly. Given the different values of t' and t'' in both approaches the almost exact quantitative agreement has to be taken with a grain of salt. Nevertheless, the curves also display the same qualitative structure (linear at low x and saturating at larger x) and suggest that the "doped carrier" MF approach captures the enhancement of nodal quasiparticle properties due to projection.

We remark that, above, we refer to arcs of low energy spectral weight in the d-wave gaped SC state and, therefore, these arcs are not true, ungaped, Fermi arcs. These persist above T_c, as seen by experiments [34, 112], once they arise in the presence of a non-vanishing magnitude of the spinon-dopon mixing MF order parameters b_0 and b_1. Right above T_c, in the Nernst region, we expect the arcs to remain gaped everywhere but along the nodal direction, as the d-wave gap parameter Δ does not vanish, in consonance with the presence of local SC fluctuations. Ungaped Fermi arcs can emerge, however, along the crossover between the Nernst and strange metal regimes.

Two spectral gaps

In Figs. 5-7(g) - 5-7(i) we plot the spectral function along the minimum gap locus. Following the aforementioned nodal-antinodal dichotomy, the SC dispersion $\epsilon^{-}_{1,\boldsymbol{k}}$ is easier to detect along the arc region. As a result, in the deeply underdoped regime

the SC peaks are hard to locate in the antinodal region and the spectrum near $(0.\pi)$ mostly reflects the high energy dispersion $\epsilon^{-}_{2,\boldsymbol{k}}$ [see Fig. 5-7(g) with $x = 0.05$]. This result is consistent with ARPES data in various cuprate families [34, 31, 23, 53, 178]. In this case the spectral function displays two gap features, of two different energy scales, as we move away from the nodal direction: close to the diagonal direction the low energy d-wave gap dispersion is easily identified, whereas near the BZ boundary only the high energy gap associated with the motion of a hole in the presence of strong local AF correlations is resolved. Evidence for such a two gap structure, of two different energy scales, has been reported for NaCCOC [34].

Peak-dip-hump spectral structure

As doping is varied toward optimal doping the spectral intensity on the $\epsilon^{-}_{1,\boldsymbol{k}}$ band close to $(0,\pi)$ increases [Figs. 5-7(h) and 5-7(i)] [31, 178, 179]. The spectral function in this momentum space region then shows two different spectral features and is consistent with the experimentally observed peak-dip-hump structure [22, 152, 135]. The peak and hump energy scales have become known as the low energy and the high energy pseudogap respectively [22]. Therefore, in the current theoretical description the low energy pseudogap is the energy $\epsilon^{-}_{1,\boldsymbol{k}}$ at $(0,\pi)$ and the high energy pseudogap is the energy $\epsilon^{-}_{2,\boldsymbol{k}}$ at $(0,\pi)$. In agreement with the experimental evidence referred to in Sec. 5.2, the low energy pseudogap $\epsilon^{-}_{1,(0,\pi)}$ coincides with the SC gap energy scale and the high energy pseudogap $\epsilon^{-}_{2,(0,\pi)}$ evolves to the large energy scale at $(0,\pi)$ observed in undoped insulators.

The existence of two spectral dispersions and two energy scales implies that similar peak-dip-hump structures are present in other regions of momentum space [135]. Indeed, in Figs. 5-4(b) and 5-4(c) we also see a nodal peak-dip-hump line shape (indicated by the vertical white dotted line) in agreement with ARPES results for LSCO [31], NaCCOC [34], Bi2201 [134], and Bi2212 [135]. We remark that the spectral peak-dip-hump is observed in single layer compounds and is not a bilayer artifact.

ARPES experiments also address the doping evolution of the spectral intensity of the SC peak at $(0,\pi)$. Specifically, the SC peak ratio (SPR), defined to be the relative intensity of the peak at $(0,\pi)$ normalized by the intensity of the entire spectrum, is studied [177, 178]. We plot the ARPES data in Fig. 5-5(d) together with the corresponding theoretical ratio $\frac{Z^{-}_{1,(0,\pi)}}{Z^{-}_{1,(0,\pi)}+Z^{-}_{2,(0,\pi)}}$ and find both curves are qualitatively similar: they increases in the underdoped regime and, around optimal doping, a downturn is observed.

Spectral weight transfer to low energy: the role of t' and t''

The spectral intensity in the low energy $\epsilon^{-}_{1,\boldsymbol{k}}$ band is stronger in the momentum space region where the high energy $\epsilon^{-}_{2,\boldsymbol{k}}$ band is closer to $\epsilon^{-}_{1,\boldsymbol{k}}$. This fact, that is easily appreciated in Figs. 5-7(g) - 5-7(i), is consistent with experiments. Indeed, the SC peak in the ARPES spectrum of cuprates is stronger when the difference between the

Fermi level and the hump energy decreases below $\approx J$, while it dies out when the hump disperses to higher energy [177]. The above observation underlies the location and doping dependence of the low energy spectral weight arcs. In fact, at low doping the $\epsilon^{-}_{2,\boldsymbol{k}}$ band disperses strongly along $(0,\pi)-(\pi,0)$ and is lower in energy close to $(\frac{\pi}{2},\frac{\pi}{2})$. Thus, dopons hybridize more strongly with spinons in the nodal region. In addition, recall that t_2 and t_3 were explicitly chosen to change with doping so that we reproduce the doping induced renormalization of t' and t'' which flattens the $\epsilon^{-}_{2,\boldsymbol{k}}$ dispersion along $(0,\pi)-(\pi,0)$ as observed by experiments [22, 53] [see Figs. 5-3(b) - 5-3(d) and Figs. 5-7(g) - 5-7(i)]. This doping dependence is introduced by hand in Sec. 4.3.4 and the underlying physical processes are discussed in Sec. 7.4. As the high energy pseudogap decreases and the $\epsilon^{-}_{2,\boldsymbol{k}}$ band approaches the $\epsilon^{-}_{1,\boldsymbol{k}}$ band around $(0,\pi)$, the spinon-dopon mixing in this part of momentum space is enhanced, thus leading to the increase of the arc length demonstrated in Fig. 5-5. Naturally, the above interpretation of experimental data implies that in case the high energy dispersion is strongly modified, as when we move from the hole doped to the electron doped case, the low energy properties of the spectral function change accordingly. Indeed, in Sec. 5.4.4 we find that by changing the signs of t' and t'' so that $\epsilon^{\pm}_{2,\boldsymbol{k}}$ fits electron doped materials' data the structure of low energy spectral weight is strongly modified in agreement with experiments. The above picture also suggests that in the absence of t' and t'' the high energy dispersion along $(0,\pi)-(\pi,0)$ is flat and the nodal-antinodal dichotomy is reduced, in accordance with variational Monte Carlo results on the tJ model [171] which yield almost constant spectral weight along $(0,\pi)-(\pi,0)$.

Flat dispersion around $(0,\pi)$ and $(\pi,0)$

In the above we show the MF electron spectral function displays two dispersive features whose momentum and energy dependent spectral intensity evolves with doping in a manner that is consistent with experiments. In the following we discuss the shape of these two spectral features and show how strong correlations also induce a non-trivial renormalization of the quasiparticle dispersion.

Remarkably, all cuprate families exhibit an extreme flattening of the dispersion in an extended region around $(0,\pi)$ [137, 135, 136]. This ubiquituous phenomenon has motivated interpretations involing anomalous scattering mechanisms in this region of momentum space such as the nearly AF Fermi liquid and Van Hove singularity scenarios [180, 181, 182, 183]. As noted in Ref. [157] the coexistence of the observed nodal dispersion large energy scale and the small energy scale of the dispersion close to the antinodes cannot be explained with the bare hopping parameters estimated from band calculations and requires careful fine-tuning in order to be reproduced. In fact, Refs. [175, 184] use effective dispersions with five hopping parameters to capture the different energy scales in the experimental dispersion. In Fig. 5-3(d) we use the parameters from Ref. [175] to compare the general features of the experimental normal state dispersion (solid white line) to that of the "doped carrier" MF theory. We find that the MF dispersion reproduces both the dispersion between $(0,0)$ and the nodal point, as well as the flat dispersion around $(0,\pi)$. The mismatch at large positive energies around (π,π) follows from the fact that, in Ref. [175], the dispersion

around (π, π) was set by hand based on band calculations and without experimental support (recall that ARPES only probes energies below the Fermi level).

Dispersion kink

The kink observed in the momentum distribution curve derived dispersion of several cuprate families in both the underdoped and overdoped regime and below and above T_c has been heavily discussed in the literature [34, 31, 22] and both phonon [133, 134] and magnetic modes [135, 185, 158] were proposed as the underlying cause for the effect. Experiments support that this feature is associated with the aforementioned peak-dip-hump spectral structure and, in particular, in NaCCOC [34], LSCO [31], Bi2201 [134] and Bi2212 [135] the kink was shown to appear at the same energy as the dip. The horizontal white dashed line in Figs. 5-4(b) and 5-4(c) separates the SC peak from the high energy hump and, thus, defines the dip energy. Following the presence of two bands with different dispersions, a kink naturally appears at the dip energy, whose value $\omega \approx \frac{J}{2}$ is in good agreement with the experimental kink energy [133]. Notably, the kink is sharper in Fig. 5-4(b) than in Fig. 5-4(c) and, therefore, the kink is found to smoothen out with increasing hole density, in consistency with experiments [133].

Minimum gap locus topology

Figs. 5-6(a) - 5-6(c) illustrate that the topology of the minimum gap locus changes from hole to electron-like as the doped hole density is increased. This transition occurs around optimal doping, more specifically at $x = 0.17$. This value differs from that found in Ref. [106], namely $x = 0.20$, since in this chapter we take smaller values of t'/t and t''/t and, consequently, the minimum gap locus has a smaller curvature thus crossing $(0, \pi)$ at higher electron density. Such a topology change has been observed in LSCO [136, 186], Bi2201 [187], and in the anti-bonding sheet of Bi2212 [188, 189]. Variational Monte Carlo calculations have also demonstrated a change in the underlying Fermi surface topology around optimal doping [127].

Interestingly, both the minimum gap locus in Fig. 5-6(a) and the maximum spectral weight locus in Fig. 5-6(d) show long straight segments close to the BZ. A similar observation in deeply underdoped LSCO samples [31] led to the proposal that the resulting nesting enhances scattering processes in the antinodal region, thus destroying quasiparticle features in this part of momentum space [31]. In addition, this scattering mechanism has also been suggested to be connected to the appearence of charge ordered states [36, 42, 190]. We remark that, here, the straight segments close to the BZ boundary for low values of x result exclusively from the interaction between spinons and dopons. The nodal-antinodal dichotomy in the present theoretical scenario is not a consequence of such a minimum gap locus structure. However, the peculiar form of the renormalized d-wave band $\epsilon^{-}_{1,\boldsymbol{k}}$ may indeed induce specific ordered structures in real space once fluctuations around the MF saddle point are properly included. This is a problem we plan to address in the future.

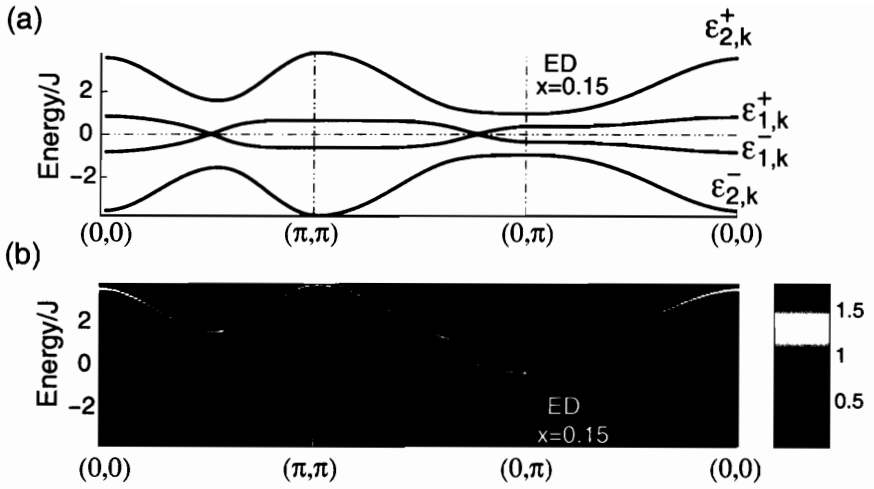

Figure 5-8: Energy dispersion along $(0,0) - (\pi,\pi) - (0,\pi) - (0,0)$ for the electron doped $x = 0.15$ SC state. (a) MF dispersions $\epsilon^{\pm}_{1,\boldsymbol{k}}$ and $\epsilon^{\pm}_{2,\boldsymbol{k}}$. (b) MF electron spectral function (5.11) with Lorentzian broadening given by $\Gamma = J/10$.

d-wave gap renormalization

Finally, we discuss the renormalization of the d-wave gap which, experiments show, normally deviates from the pure d-wave dispersion $\Delta_{\boldsymbol{k}} = \Delta_0 \cos 2\theta_{\boldsymbol{k}}$ [169]. In the present MF approach the spinon d-wave dispersion is flattened close to the nodal points due to the hybridization with dopons. Since the spinon-dopon mixing increases for larger x, the deviation from the pure d-wave form increases with hole density, as depicted in Figs. 5-7(j) - 5-7(l). We fit the gap dispersion along the minimum gap locus to the functional form $\Delta_{\boldsymbol{k}} = \Delta_0[B\cos 2\theta_{\boldsymbol{k}} + (1-B)\cos 6\theta_{\boldsymbol{k}}]$ and find that B equals 0.97, 0.93 and 0.89 for $x = 0.05$, $x = 0.12$ and $x = 0.20$ respectively. Experiments generally find $B \sim 0.9$ [169], in agreement with the MF theory estimate in the $x \approx 0.10 - 0.20$ range. ARPES data also suggests that, around optimal doping, B increases with hole concentration as the system goes from the underdoped to the overdoped regime [169]. This doping dependence differs from that of MF theory, which is intrinsically a low doping approach and, as such, should be firstly compared to phenomenology in the underdoped region of the phase diagram. As explained above, due to the nodal-antinodal dichotomy ARPES experiments cannot resolve the full SC d-wave dispersion in the deeply underdoped regime and, then, cannot address the doping dependence of B for low x. Since other experiments seem to indicate the reduction of arc length [23, 191] and the increase of gap velocity at the nodes [12] with decreasing doping, we naively expect the SC gap dispersion to be less renormalized in the underdoped limit.

5.4.4 Electron doped case

In the previous section we discussed the MF spectral function for the SC state and compared it to ARPES data of hole doped materials, which shows two dispersive

features, one inhereted from the undoped parent compound and another whose spectral intensity increases as the electron concentration is reduced from half-filling. The former dispersion corresponds to the lower Hubbard band and is also observed in electron doped compounds approximately 1.3eV below the Fermi energy [39]. As the electron density becomes larger than $n = 1$ spectral weight is transfered from the lower Hubbard band to the mid-gap region [39]. In addition, ARPES in electron doped samples also sees the low energy electron pockets that appear as the chemical potential shifts to the bottom of the upper Hubbard band. In this chapter we use the $tt't''J$ model representation of the cuprates and, as such, we cannot reproduce the above three spectral features shown by ARPES experiments on electron doped materials. This model sets the correlation gap $U \rightarrow \infty$ and completely disregards the presence of the lower Hubbard band. As depicted in Fig. 5-8 the MF spectral function captures both the mid-gap spectral weight and the upper Hubbard band. The former leads to a flat dispersion below the Fermi level $\omega = 0$ while the latter strongly disperses above this energy, in accordance with cluster perturbation theory results on the Hubbard model [192, 193, 194].

Electron pockets

In the hole doped regime doped carriers strongly frustrate the AF spin background and change the nature of the surrounding spin correlations, as reflected in the absence of hole pockets around $(\frac{\pi}{2}, \frac{\pi}{2})$. AF correlations are more robust in the electron doped case due to the sign change of t' and t'' [60] and, as a result, the chemical potential crosses the bottom of the upper Hubbard band and gives rise to electron pockets. The sign of t' and t'' also implies that such pockets appear around $(0, \pi)$ and $(\pi, 0)$ [39, 48, 167]. Figs. 5-9(a), 5-9(d) and 5-9(g) depict the corresponding MF results for the underdoped AF state which are consistent with the aforementioned phenomenology. The first two figures show the electron momentum distribution function and the integrated spectral weight in an energy window around the Fermi level respectively, both displaying sharp pockets. The third figure depicts the spectral function along the $(0, \pi) - (\pi, 0)$ line which shows the dopon pocket dispersion $\epsilon^{-}_{d,\boldsymbol{k}}$ defined in Equation (4.50).

Nodal spectral weight as the signature of superconducting correlations

In Figs. 5-9(c), 5-9(f) and 5-9(i) we plot MF results regarding the dSC phase at doping level $x = 0.15$. Comparing these to the aforementioned Figs. 5-9(a), 5-9(d) and 5-9(g), which concern the AF phase at $x = 0.05$, we find that in addition to the spectral intensity around $(0, \pi)$ and $(\pi, 0)$ in the SC phase spectral weight develops along the nodal direction as well. Interestingly, experiments show that, even in the AF phase, there is a buildup of spectral weight around $(\frac{\pi}{2}, \frac{\pi}{2})$ inside the Mott-Hubbard gap which in the SC state forms the Dirac nodal dispersion characteristic of d-wave superconductors [39, 165, 166]. Therefore, we associate the spectral intensity along the diagonal direction to the increasing relevance of dSC correlations.

Antiferromagnetism survives up to a large dopant density on the electron doped

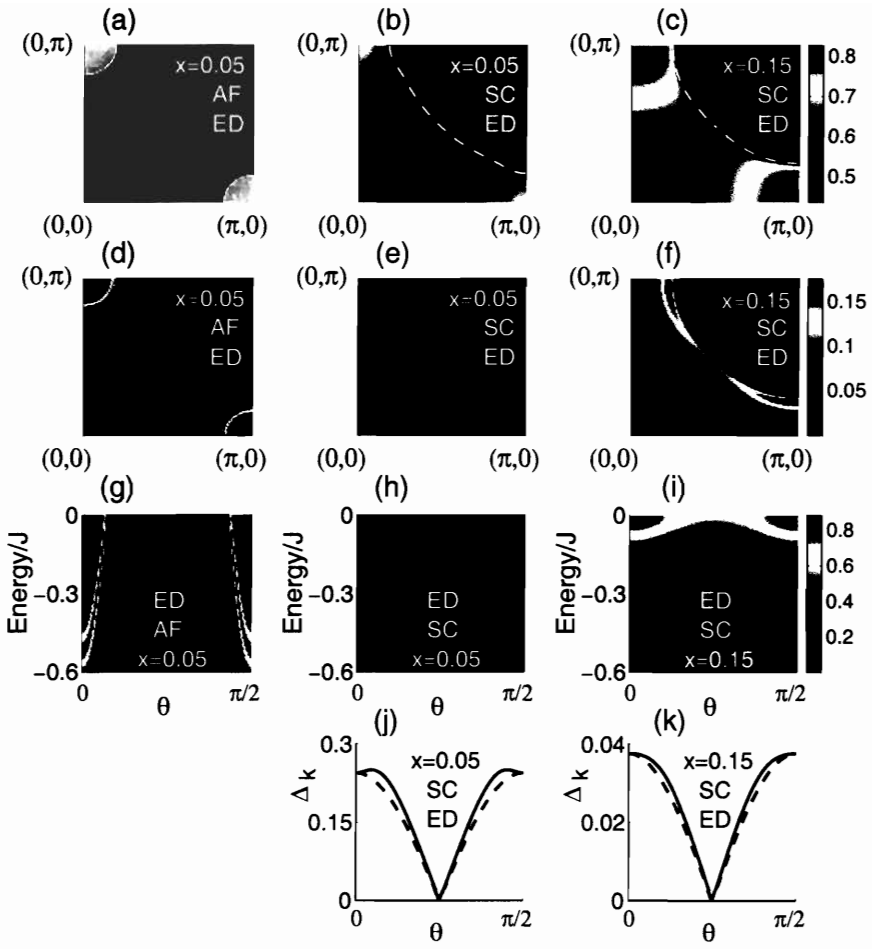

Figure 5-9: MF electron spectral function results for the electron doped $x = 0.05$ AF state [(a),(d) and (g)], the $x = 0.05$ dSC state [(b),(e),(h) and (j)] and the $x = 0.15$ dSC state [(c),(f),(i) and (k)]. (a)-(c) Electron momentum distribution $n_{\boldsymbol{k}} = 1 - Z^{-}_{1,\boldsymbol{k}} - Z^{-}_{2,\boldsymbol{k}}$ (top color scale). The white dashed line in (b) and (c) depicts the minimum gap locus. (d)-(f) Integrated electron spectral weight around the Fermi level (middle color scale). The energy window $[-0.15J, 0.15J]$ is used. (g)-(i) Electron spectral function (5.11) along minimum gap locus (bottom color scale). A Lorentzian broadening with $\Gamma = J/10$ is used in (d)-(i). (j) and (k) $\epsilon^{+}_{1,\boldsymbol{k}}$ dispersion gap (solid line) and pure d-wave dispersion ($\Delta_{\boldsymbol{k}} = \Delta_0 \cos 2\theta_{\boldsymbol{k}}$) with same gap magnitude (dashed line) along minimum gap locus. Note that the pure d-wave dispersion lies below $\epsilon^{+}_{1,\boldsymbol{k}}$ implying $B > 1$ (see main text). The energy scales in (j) and (k) are different. The angular variable θ used to parameterize the points along the minimum gap locus is defined in Fig. 5-6(d).

side and, thus, in order to address the development of dSC correlations in the electron underdoped samples requires one to capture SC correlations in the AF phase. However, in the MF AF phase described in Sec. 4.4 and Appendix 4.8 spinons and dopons do not hibrydize and we do not reproduce the effects of local dSC correlations in presence of long-range AF order. In fact, this paper's goal is to describe the dSC state with strong local AF correlations due to the proximate Mott transition and we leave the problem of describing strong local SC correlations in the AF phase as future work. Even though the latter is more relevant to electron doped materials, we can still use the paramagnetic MF theory described by the MF Hamiltonian H_{tJ}^{MF} in (4.22) to gain insight on the physics of electron doped cuprates. As it is further discussed in Chapter 7 the "doped carrier" MF theory accounts for both short-range AF and SC correlations. The presence of AF long-range order should affect the spinon dispersion, which gets a gap equal to $2|J^*m - n|$, but not the general features of the spectral weight momentum space distribution, which are determined by short-range phenomena. Therefore, we also plot MF results for the paramagnetic SC state with $x = 0.05$ [Figs. 5-9(b), 5-9(e) and 5-9(h)]. We remark that these results cannot be directly compared to experiments since spinons are gapped along the nodal direction in the $x = 0.05$ AF state, and the spectral weight that appears in Figs. 5-9(e) and 5-9(h) close to $(\frac{\pi}{2}, \frac{\pi}{2})$ at the Fermi level should be at higher energy in the AF phase with local dSC correlations.

Keeping in mind the above remark, below we focus on the paramagnetic SC solutions for $x = 0.05$ and $x = 0.15$ to analyze how the transfer of spectral weight from the antinodes to the nodal region underlies the emergence of SC quasiparticles near $(\frac{\pi}{2}, \frac{\pi}{2})$. Figs. 5-9(b) and 5-9(c) depict the corresponding electron momentum distribution function and we see that doped electrons spread throughout the region between the minimum gap locus and $(0, 0)$. This distribution is uneven in momentum space and the regions around $(0, \pi)$ and $(\pi, 0)$ carry most of the spectral intensity. Comparing Figs. 5-9(b) and 5-9(c) to Fig. 5-9(a) supports that the momentum space anisotropy in the first two figures follows from the presence of strong local AF correlations in the doped Mott insulator state without AF long-range order. This anisotropy is also observable in Figs. 5-9(h) and 5-9(i) which show that the majority of spectral weight along the minimum gap locus lies close to the BZ boundary.

Notably, the same local AF correlations are responsible for the hole pocket-like features in Figs. 5-6(a) - 5-6(c) and for the enhancement of quasiparticle properties around the nodes in the hole doped case [Figs. 5-6(d) - 5-6(f) and 5-7(g) - 5-7(i)]. Hence, as a result of the t' and t'' sign change, the direction of the nodal-antinodal dichotomy shifts when we go from the hole doped to the electron doped regime [102]. In the fomer, both AF and SC correlations contribute to the presence of quasiparticles around $(\frac{\pi}{2}, \frac{\pi}{2})$ and lead to low energy spectral weight arcs [Figs. 5-6(d) - 5-6(f)]. In the latter, AF correlations enhance spectral weight close to $(0, \pi)$ and $(\pi, 0)$ while SC correlations favor low energy quasiparticles along the diagonal direction.

This interplay between AF and SC correlations in the electron doped case plays an interesting role in the doping evolution of the spectral intensity around the Fermi level. Specifically, as SC correlations grow in relevance, spectral weight is transfered from the pockets at $(0, \pi)$ and $(\pi, 0)$ to the nodal region [Fig. 5-9(e)]. At higher

values of doping, in the SC phase, the spectrum close to the Fermi energy displays a large, d-wave gapped, "Fermi surface" [5-9(f)]. This behavior is reminiscent of that observed by ARPES [39, 164, 165, 143].

d-wave gap renormalization

In Sec. 5.4.3 we discuss how local AF correlations renormalize the d-wave SC dispersion along the minimum gap locus in the hole doped regime [Figs. 5-7(j) - 5-7(l)]. In particular, we find that the d-wave dispersion is flattened around the diagonal direction, which implies that $B < 1$ if the functional form $\Delta_{\boldsymbol{k}} = \Delta_0[B\cos 2\theta_{\boldsymbol{k}} + (1-B)\cos 6\theta_{\boldsymbol{k}}]$ is used to fit the experimental dispersion. In the electron doped case short-range AF correlations are relevant close to the antinodes instead and, consequently, the d-wave dispersion deviates from the pure d-wave form in this region of momentum space. Recurring to the above functional form to fit the dispersions in Figs. 5-9(j) and 5-9(k) we obtain $B = 1.04$. A value $B > 1$ indeed implies that the d-wave dispersion is flattened or, for large enough B, displays a downturn away from the nodal direction. This fact finds experimental support in ARPES [166] and Raman scattering [168] data, both of which provide evidence for a non-monotonic d-wave SC gap. In particular, the ARPES dispersion suggests $B = 1.43$ [166] which is much larger than the one obtained from Figs. 5-9(j) and 5-9(k). Even though we can fine-tune the MF parameters to closely reproduce the non-monotonic d-wave dispersion at MF level, we believe that better agreement with experiments may be reached for instance by introducing an extended d-wave pairing gap [195].

Another difference between Figs. 5-9(j) and 5-9(k) and Figs. 5-7(j) - 5-7(l) is the gap magnitude, which is smaller in the electron doped case. As discussed in Sec. 4.4, when $t' < 0$ and $t'' > 0$ the dispersion of a hole surrounded by AF correlations is similar to that of spinons and, therefore, the spinon $d_{x^2-y^2}$ dispersion is not frustrated by hole hopping. In the opposite case, when $t' < 0$ and $t'' > 0$, AF short-range correlations induce a gap at $(\frac{\pi}{2}, \frac{\pi}{2})$ instead, thus frustrating the spinon $d_{x^2-y^2}$ dispersion and weakening dSC order. This fact is also evidenced in the hole doped *vs.* electron doped asymmetry of the SC region in the MF phase diagram [Figs. 4-1(a) and 4-1(b)].

5.5 Conclusions

In Chapter 4 we introduce a new MF theory to describe the low doping and low temperature paramagnetic regime of the $tt't''J$ model which captures the crutial dependence of the hole dynamics on the background spin correlations (a characteristic of strongly correlated systems). Therefore, in this chapter we use it to address the single hole dynamics in the dSC state near the Mott insulator transition as observed in the high-T_c cuprate materials.

As discussed in Chapter 4, we use model parameters borrowed from band calculations. The single input from experiments concerns the change with doping of the high energy $\epsilon^{\pm}_{2,\boldsymbol{k}}$ dispersion along $(0,\pi) - (\pi,0)$ in order to reproduce the lowering of the high energy pseudogap energy scale with the change in hole concentration. We

remark that there is no such experimental input on the low energy d-wave dispersion $\epsilon^{\pm}_{1,\boldsymbol{k}}$, whose spectral properties follow from theory alone. Notably, these properties agree with experiments, as we briefly summarize below.

In Sec. 5.4 we show the MF theory obtains spectral peaks, which disperse linearly across the Fermi energy and whose weight vanishes at half-filling, that develop above the insulating valence band (Fig. 5-4) [34, 112, 23, 24]. The corresponding low energy spectral weight forms arcs around the nodal direction whose length enlargens with doping in accordance with experimental data [Fig. 5-5(b)] [34, 23, 112]. This amounts to the nodal-antinodal dichotomy [31], that expects enhanced nodal quasiparticle features as obtained by the current MF theory, which is consistent with variational Monte Carlo results [Fig. 5-5(c)] [171]. Following the two-band nature of the MF approximation, a peak-dip-hump spectral structure is obtained in different momentum space regions [135]. Interestingly, the above calculation captures the doping evolution of the spectral intensity of the peak feature at $(0, \pi)$ [Fig. 5-5(d)] [177, 178]. Along the nodal direction a dispersion kink, which smoothens out with doping, appears at the dip energy $\omega \approx \frac{J}{2}$ [Figs. 5-4(b) and 5-4(c)] in close agreement with experiments [133, 134, 34, 31, 22, 135, 185]. The MF theory also predicts the evolution of the minimum gap locus topology with doping [Figs. 5-6(a) - 5-6(c)] in consistency with ARPES data [136, 186, 187, 188, 189] and variational Monte Carlo computations [127], and reproduces the strong renormalization of the dispersion which is suprisingly flat around $(0, \pi)$ [Fig. 5-3(d)] [137, 135, 136]. In addition, the renormalization of the superconducting gap is also consistent with experiments – it deviates from the pure d-wave form in that it flattens around the nodal direction in the hole doped regime [Figs. 5-7(j) - 5-7(l)] and in the antinodal region for the electron doped case [Figs. 5-9(j) and 5-9(k)] [166, 168, 169]. Finally, in Sec. 5.4.4 we show the differences between hole and electron doped spectra can be rationalized in terms of the fact that AF correlations induce a gap at $(0, \pi)$ in the former case and at $(\frac{\pi}{2}, \frac{\pi}{2})$ in the electron doped regime.

To the above semi-quantitative agreement with experiments and other, more rigorous, theoretical approaches we must add that the "doped carrier" MF theory is also consistent with tunneling experiments (Chapter 6) and with the renormalization of the quasiparticle current measured by the temperature dependence of the penetration depth [196].

The central point of this chapter is to propose a theoretical description of ARPES data of superconducting doped Mott insulators, which deviates in many ways from conventional BCS MF behavior. The "doped carrier" MF approach, which accounts for the role of both staggered moment and d-wave singlet pair correlations, is found to reproduce a broad set of non-trivial experimental observations. Therefore, our results support that short-range AF and dSC correlations coexist throughout a vast range of the high-T_c phase diagram. Interestingly, this chapter illustrates how ARPES data can provide crutial insights to understand the short-range correlations that develop in the cuprate underdoped regime.

5.6 Appendix: Electron operator

5.6.1 Hole doped case

The $tt't''J$ model Hilbert space on site i includes the three physical states $|\uparrow\rangle_i^{phys}$,$|\downarrow\rangle_i^{phys}$ and $|0\rangle_i^{phys}$. In the HD case, the first two states represent a singly occupied site with a spin-up and spin-down electron respectively. The third state refers to an empty site. In the above constrained Hilbert space, which forbids double electron occupancy, the electron annihilation and creation operators are defined by the following relations:

$$
\begin{aligned}
c_{i,\uparrow}\begin{pmatrix} |\uparrow\rangle_i^{phys} \\ |\downarrow\rangle_i^{phys} \\ |0\rangle_i^{phys} \end{pmatrix} &= \begin{pmatrix} |0\rangle_i^{phys} \\ 0 \\ 0 \end{pmatrix} \\
c_{i,\downarrow}\begin{pmatrix} |\uparrow\rangle_i^{phys} \\ |\downarrow\rangle_i^{phys} \\ |0\rangle_i^{phys} \end{pmatrix} &= \begin{pmatrix} 0 \\ |0\rangle_i^{phys} \\ 0 \end{pmatrix} \\
c_{i,\uparrow}^{\dagger}\begin{pmatrix} |\uparrow\rangle_i^{phys} \\ |\downarrow\rangle_i^{phys} \\ |0\rangle_i^{phys} \end{pmatrix} &= \begin{pmatrix} 0 \\ 0 \\ |\uparrow\rangle_i^{phys} \end{pmatrix} \\
c_{i,\downarrow}^{\dagger}\begin{pmatrix} |\uparrow\rangle_i^{phys} \\ |\downarrow\rangle_i^{phys} \\ |0\rangle_i^{phys} \end{pmatrix} &= \begin{pmatrix} 0 \\ 0 \\ |\downarrow\rangle_i^{phys} \end{pmatrix}
\end{aligned}
\tag{5.13}
$$

The mapping between the $tt't''J$ model on-site Hilbert space and the physical states of the enlarged on-site Hilbert space (4.2) reduces to

$$
\begin{aligned}
|\uparrow\rangle_i^{phys} &= f_{i,\uparrow}^{\dagger}|0\rangle_i^{enl} \\
|\downarrow\rangle_i^{phys} &= -f_{i,\downarrow}^{\dagger}|0\rangle_i^{enl} \\
|0\rangle_i^{phys} &= \frac{1}{\sqrt{2}}\left(f_{i,\downarrow}^{\dagger}d_{i,\uparrow}^{\dagger} - f_{i,\uparrow}^{\dagger}d_{i,\downarrow}^{\dagger}\right)|0\rangle_i^{enl}
\end{aligned}
\tag{5.14}
$$

where $|0\rangle_i^{enl}$ is the empty site in the fermionic representation of the enlarged Hilbert space, *i.e.* it is the unphysical state with no spinons and no dopons. All other on-site states obtained upon acting with the operators $f_{i\sigma}^{\dagger}$ and $d_{i,\sigma}^{\dagger}$ on $|0\rangle_i^{enl}$ are unphysical and vanish when acted upon by the physical electron operator.

Hence, using both (5.13) and (5.14), the defining relations for the spin-up electron annihilation operator in the enlarged Hilbert space are

$$
\begin{aligned}
c_{i,\uparrow}f_{i,\uparrow}^{\dagger}|0\rangle_i^{enl} &= \frac{1}{\sqrt{2}}\left(f_{i,\downarrow}^{\dagger}d_{i,\uparrow}^{\dagger} - f_{i,\uparrow}^{\dagger}d_{i,\downarrow}^{\dagger}\right)|0\rangle_i^{enl} \\
c_{i,\uparrow}f_{i,\downarrow}^{\dagger}|0\rangle_i^{enl} &= c_{i,\uparrow}f_{i,\alpha}^{\dagger}d_{i,\beta}^{\dagger}|0\rangle_i^{enl} = 0
\end{aligned}
\tag{5.15}
$$

while for the spin-up electron creation operator we must have

$$
\begin{aligned}
c_{i,\uparrow}^{\dagger}\left[\frac{1}{\sqrt{2}}\left(f_{i,\downarrow}^{\dagger}d_{i,\uparrow}^{\dagger}-f_{i,\uparrow}^{\dagger}d_{i,\downarrow}^{\dagger}\right)|0\rangle_{i}^{enl}\right] &= f_{i,\uparrow}^{\dagger}|0\rangle_{i}^{enl} \\
c_{i,\uparrow}^{\dagger}\left[\frac{1}{\sqrt{2}}\left(f_{i,\downarrow}^{\dagger}d_{i,\uparrow}^{\dagger}+f_{i,\uparrow}^{\dagger}d_{i,\downarrow}^{\dagger}\right)|0\rangle_{i}^{enl}\right] &= 0 \\
c_{i,\uparrow}^{\dagger}f_{i,\alpha}^{\dagger}d_{i,\alpha}^{\dagger}|0\rangle_{i}^{enl} &= 0 \\
c_{i,\uparrow}^{\dagger}f_{i,\alpha}^{\dagger}|0\rangle_{i}^{enl} &= 0
\end{aligned}
\tag{5.16}
$$

The electron operators also vanish if $d_i^{\dagger}d_i = 2$ or $f_i^{\dagger}f_i \neq 1$. The above conditions lead to the following expression for the electron operator in the fermionic representation of the enlarged Hilbert space

$$
c_{i,\sigma} = \widetilde{\mathcal{P}}\frac{1}{\sqrt{2}}\left(d_{i,-\sigma}^{\dagger}f_{i,\sigma}^{\dagger}f_{i,\sigma}f_{i,-\sigma}f_{i,-\sigma}^{\dagger}-d_{i,\sigma}^{\dagger}f_{i,-\sigma}^{\dagger}f_{i,\sigma}\right)\widetilde{\mathcal{P}} \tag{5.17}
$$

The spin-down electron operators naturally follow from the spin-up counterparts by applying the rotation operator.

5.6.2 Electron doped case

In the ED regime the states $|\uparrow\rangle_i^{phys}$,$|\downarrow\rangle_i^{phys}$ and $|0\rangle_i^{phys}$ rather represent a spin-up hole, a spin-down hole and a site with no holes respectively. Therefore, the operator in (5.17) is a hole annihilation operator or, equivalently, an electron creation operator.

Chapter 6

Tunneling spectra of layered strongly correlated d-wave superconductors

I shall always be consistent and never change my ways so long as I am in my senses...

Tiberius Caesar

6.1 Introduction

Tunneling and angle-resolved photoemission spectroscopy (ARPES) are unique experimental techniques in that they probe the single electron microscopic physics of strongly correlated systems like the cuprate d-wave superconductors. Even though both techniques support the presence of well defined Bogoliubov nodal quasiparticles in these materials, away from the nodes deviations from the BCS paradigm are encountered [11, 15, 36, 159, 42, 31, 34, 112, 136, 23]. Simultaneously describing these deviations in ARPES and tunneling experiments is of utmost importance to understand the nature of the underlying strong local correlations.

ARPES experiments of high-T_c superconductors have revealed many non-trivial features, such as the strong band renormalization close to $(0, \pi)$ and $(\pi, 0)$ [137] and the sharp momentum space anisotropy of electronic states, known as the nodal-antinodal dichotomy [31, 34, 112, 136, 23], to just name a few. In this chapter, we use the mean field (MF) theory of doped Mott insulators introduced in Chapter 4, which accounts for many fingerprints of strong correlation physics in ARPES, to discuss the tunneling spectra of such strongly correlated d-wave superconductors. We show that the tunneling spectra of cuprate compounds can be reproduced by this MF theory and, thus, we obtain a consistent theoretical description of ARPES and tunneling spectroscopy.

In addition, we compare the spectra of cuprate superconductors with the weak coupling BCS picture, which generally predicts multiple peaks in the tunneling spectra of quasi-2D superconducting (SC) materials (besides the two SC coherence peaks)

[197, 198]. These extra peaks, caused by the underlying Van Hove (VH) singularities in the quasiparticle density of states (DOS), are not observed by experiments though – this result is robust as it is valid for different materials and doping values [36, 159, 199, 200, 201, 202]. Notably, in the deeply underdoped regime, not even the SC coherence peaks are observed in the tunneling spectra of these materials [36, 159, 42, 160]. Below, we argue the above experimental results stem from the proximity to the Mott insulator transition. Therefore, tunneling spectroscopy is an important experimental tool to establish the strongly correlated nature of cuprate superconductors.

6.2 Tunneling spectra of BCS d-wave superconductors

We consider the tunneling across a normal-metal – insulator – superconductor junction in the case of a 2D superconductor. Under the assumption of specular transmission across a thin planar junction within the elastic channel, the differential tunneling conductance perpendicular to the 2D layers can be essentially equated to the quasiparticle DOS [203, 204] and, at zero temperature, it is given by [205]

$$\frac{dI}{dV} = 4e\pi M^2 N(E_F) \sum_{\boldsymbol{k}} A(V, \boldsymbol{k}) \tag{6.1}$$

where M is the tunneling matrix element, $N(E_F)$ is the normal-metal density of states, V is the bias of the SC sample with respect to the metal and $A(\omega, \boldsymbol{k})$ is the electron spectral function in the SC sample. The sum in (6.1) is over the 2D layer's Brillouin zone.

The BCS electron spectral function is $A(\omega, \boldsymbol{k}) = u_{\boldsymbol{k}}^2 \delta(\omega - E_{\boldsymbol{k}}) + v_{\boldsymbol{k}}^2 \delta(\omega + E_{\boldsymbol{k}})$, where the coherence factors are $u_{\boldsymbol{k}}^2 = \frac{1}{2}(1 + \frac{\varepsilon_{\boldsymbol{k}}}{E_{\boldsymbol{k}}})$ and $v_{\boldsymbol{k}}^2 = \frac{1}{2}(1 - \frac{\varepsilon_{\boldsymbol{k}}}{E_{\boldsymbol{k}}})$ and the SC quasiparticle energy dispersion is $E_{\boldsymbol{k}} = [\varepsilon_{\boldsymbol{k}}^2 + \Delta_{\boldsymbol{k}}^2]^{1/2}$. In the tight-binding approximation to the copper-oxide layer of high-T_c materials, the normal state dispersion is $\varepsilon_{\boldsymbol{k}} = -2t[\cos(k_x) + \cos(k_y)] - 4t' \cos(k_x)\cos(k_y) - 2t''[\cos(2k_x) + \cos(2k_y)] - E_F$ where t, t' and t'' are the 1^{st}, 2^{nd} and 3^{rd} nearest-neighbor (NN) hopping parameters, with $t' \approx -2t''$ [111]. Note that the 1^{st} NN hopping term does not disperse along $(0, \pi) - (\pi, 0)$, whereas for $t' = -2t''$ the 2^{nd} and 3^{rd} NN terms do not disperse along $(0, 0) - (\pi, \pi)$. Hence t controls the nodal direction dispersion, while $t' = -2t''$ control the normal state dispersion between the antinodal points [$(0, \pi)$ and $(\pi, 0)$]. Together with the doping level, the ratios t'/t and t''/t also determine the shape of the Fermi surface.

In the SC state, the minimal gap locus follows the normal state Fermi surface. The minimal gap has a form $|\Delta_{\boldsymbol{k}} \equiv \Delta \cos(2\theta)|$, where θ is defined in Fig. 6-1(a). In the parameter regime relevant to underdoped cuprates, the minimal gap locus has a hole-like topology and we denote its intersection with the $(0, \pi) - (\pi, \pi)$ line by $\boldsymbol{k}_A$. The d-wave gap leads to a singularity in $E_{\boldsymbol{k}}$ which appears as the two SC coherence peaks at $\pm\Delta$ in the dI/dV spectrum. The VH singularity in $\varepsilon_{\boldsymbol{k}}$ at $(0, \pi)$ and $(\pi, 0)$ shows up in the BCS tunneling spectrum at $V = -E_{VH} \equiv -[\varepsilon_{\boldsymbol{k}=(0,\pi)}^2 + \Delta^2]^{1/2}$. This

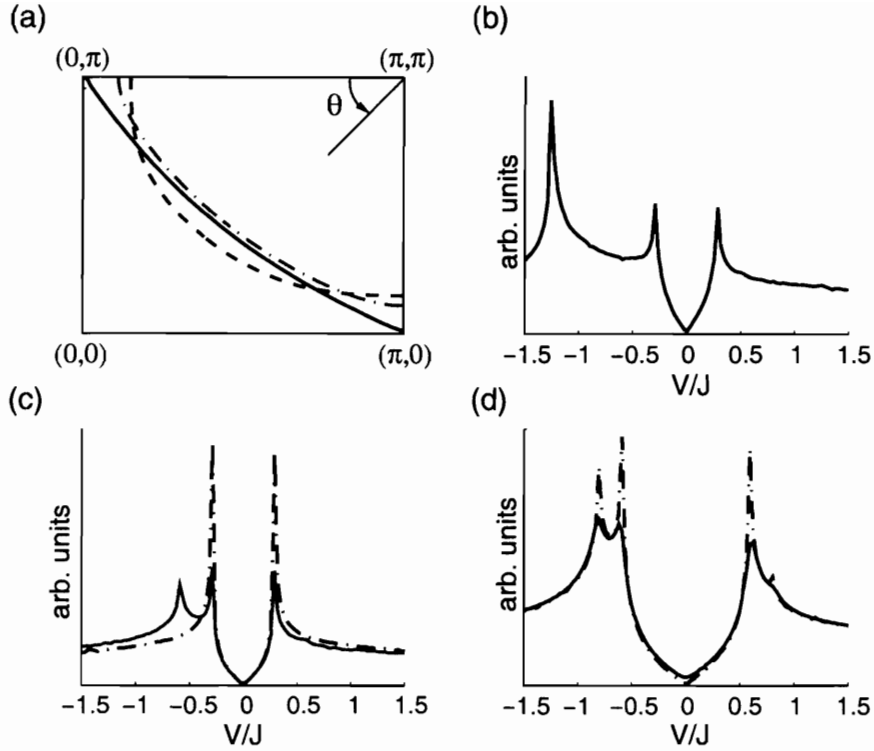

Figure 6-1: (a) Fermi surface of $\varepsilon_{\boldsymbol{k}}$ with $t' = -2t'' = -0.24t, x = 0.20$ (dashed line), $t' = -2t'' = -0.12t$ for $x = 0.20$ (full line) and for $x = 0.10$ (dash-dot line). Tunneling differential conductance for: (b) $t' = -2t'' = -0.24t, \Delta = 45\text{meV}, x = 0.20$; (c) $t' = -2t'' = -0.12t, \Delta = 45\text{meV}$ where $x = 0.20$ for dash line and $x = 0.10$ for full line; (d) $t' = -2t'' = -0.12t, \Delta = 90\text{meV}, x = 0.10$ without broadening (dash line) and with Lorentzian broadening $\Gamma = 4.5\text{meV}$. $t = 450\text{meV}$ throughout and bias is given in units of J where $J = 150\text{meV}$. Plots obtained for a 2000×2000 mesh of the Brillouin zone and energy resolution of 3meV.

VH singularity appears as a separate peak in dI/dV unless $\boldsymbol{k}_A \approx (0,\pi)$ or $E_{VH} - \Delta$ is so small that spectral broadening smears the VH and the SC coherence peaks into a single feature.

To illustrate the above discussion, consider the following parameters of relevance to the cuprate systems: $t = 450\text{meV}$, $t' = -2t'' = -0.24t$, $\Delta = 45\text{meV}$ and electron density $1 - x = 0.80$. Fig. 6-1(b) depicts the corresponding tunneling differential conductance, which shows a VH singularity peak at negative bias. Now consider that t' and t'' are lowered below the respective band calculation values to $t' = -2t'' = -0.12t$, so that the normal state Fermi surface crosses $(0,\pi)$ [Fig. 6-1(a)]. Then, the tunneling spectrum displays only one peak on each side of $V = 0$ [Fig. 6-1(c)] and, in that regard, it is consistent with the experimental spectra close to optimal doping. However, if the electron concentration is increased to $1 - x = 0.90$, the normal state Fermi surface is pushed away from the antinodal point [Fig. 6-1(a)] and an additional peak appears behind the negative bias SC coherence peak [Fig. 6-1(c)]. This double peak structure still survives if, as expected for real materials, the d-wave gap is doubled to $\Delta = 90\text{meV}$ and a Lorentzian broadening $\Gamma = 4.5\text{meV}$ is included [Fig. 6-1(d)].

We see that, except for some special cases, the weak coupling BCS picture almost always produces extra peaks. This behavior contrasts with the experimental observation that no doubling of the peak structure occurs as the hole doping level is decreased [36, 159, 199]. This may imply that: (i) the ratios t'/t and t''/t decrease as the doping is reduced in such a way that k_A remains almost at $(0,\pi)$; (ii) t decreases for larger electron densities, so that $E_{VH} - \Delta$ is low enough to be washed out by spectral broadening. However, ARPES measurements suggest that k_A moves away from $(0,\pi)$ [136] and that no flattening of the nodal dispersion occurs upon lowering the hole concentration [133]. Therefore, within the weak coupling BCS approach, extra hopping parameters must be included to explain the experimental data. To explain the absence of the VH singularity in the dI/dV curve, the energy dispersion along $(0,\pi) - (\pi,0)$ must be renormalized by an order of magnitude to below the gap energy scale $\sim 50\text{meV}$ (that is consistent with ARPES, which shows a very flat dispersion in the antinodal region for various cuprate families [137]). ARPES also constrains the much larger nodal dispersion energy scale as well as the curvature of the Fermi surface, so that several phenomenological parameters are required – Fig. 6-2(a) displays the normal state dispersions obtained from experimental fits involving up to 5 hopping terms [175, 184]. As it is pointed out in Ref. [157], the ubiquity of the discrepancy between the energy scale of the nodal dispersion and that of the extended flat region around $(0,\pi)$ throughout the various cuprate families and doping levels suggests the effect of strong dispersion renormalization due to interactions. Below we argue that such phenomenological dispersions are natural to doped Mott insulators.

6.3 Dispersion renormalization

To discuss the renormalization of the single electron dispersion relation in doped Mott insulators we consider the $tt't''J$ model, whose numerical calculations reproduce many spectral features of the cuprates [46, 48]. Both theory and experiments support that the NN hopping and spin exchange parameters, $t \approx 450$meV and $J \approx 150$meV, are determined by the properties of the CuO_2 planes and are relatively material independent, whereas $t' \approx -2t''$ depend on the surrounding chemical composition and vary for different cuprate families [111, 53].

In the near-half-filling antiferromagnetic (AF) insulator case the electron dispersion is renormalized by the strong local AF correlations. In particular, NN hopping is heavily frustrated by the AF background and, for $t' = t'' = 0$, holes hop coherently within the same sublattice by virtue of spin fluctuations [108]. As a result, the width of the nodal dispersion is reduced by a factor of ~ 10 from the bare value $8t$ down to $2.2J$ [46]. t' and t'' describe intrasublattice hopping processes and, thus, the dispersion width along $(0,\pi) - (\pi,0)$ is only renormalized by a factor $\sim 2-3$ [46]. The material dependence of the dispersion between the antinodal points agrees with that expected from band theory calculations of t' and t'' [53].

Away from half-filling, holes distort the AF spin background and change the surrounding spin configuration in order to coherently hop between NN sites and thus gain extra kinetic energy. Interestingly, exact diagonalization calculations suggest that the resulting local spin correlations strongly renormalize t' and t'' (see Chapter 2). This effect is discussed within the context of certain resonating valence bond models in Chapters 3 and 7 and is consistent with the experimentally observed doping induced flatness of the dispersion in the antinodal region [137].

The "doped carrier" MF approach introduced in Chapter 4 accounts for the interplay between the exchange energy of localized spins and the kinetic energy of delocalized holes. Here, we present only a qualitative description of the MF theory and defer the readers to Chapters 4 and 5 for formal details. This theory describes doped Mott insulators in terms of two different fermions: (i) dopons, which have the same charge $+e$ and spin-1/2 as holes, describe vacancies surrounded by an AF spin configuration; (ii) spinons, which have no electric charge, describe spin-1/2 excitations of the spin background. The MF Hamiltonian thus has four fermionic bands: $\epsilon^-_{1,\boldsymbol{k}} = -\epsilon^+_{1,\boldsymbol{k}}$ and $\epsilon^-_{2,\boldsymbol{k}} = -\epsilon^+_{2,\boldsymbol{k}}$ [Fig. 6-2(b)]. If dopons and spinons do not hybridize, the high energy bands $\epsilon^\pm_{2,\boldsymbol{k}}$ describe the dynamics of holes in an AF background and, at MF level, the spinon $\epsilon^\pm_{1,\boldsymbol{k}}$ bands do not contribute to electron spectral properties. The process of hybridizing dopons and spinons, which describes the change in spin correlations due to hole hopping, couples spin and charge dynamics and transfers electron spectral weight from $\epsilon^\pm_{2,\boldsymbol{k}}$ to the lower energy $\epsilon^\pm_{1,\boldsymbol{k}}$ bands [Fig. 6-2(c)]. This spectral weight transfer is not uniform in momentum space. As a result, the $\epsilon_{1,\boldsymbol{k}}$ band has a finite spectral weight near the node points and almost no spectral weight near the antinodal points for underdoped samples. This is consistent with the nodal-antinodal dichotomy in ARPES data where the well defined quasiparticle is observed only near the nodal points (Chapter 5) After the hybridization, the resulting state is a d-wave SC and the low energy dispersions $\epsilon^\pm_{1,\boldsymbol{k}}$ capture the underlying d-wave pairing

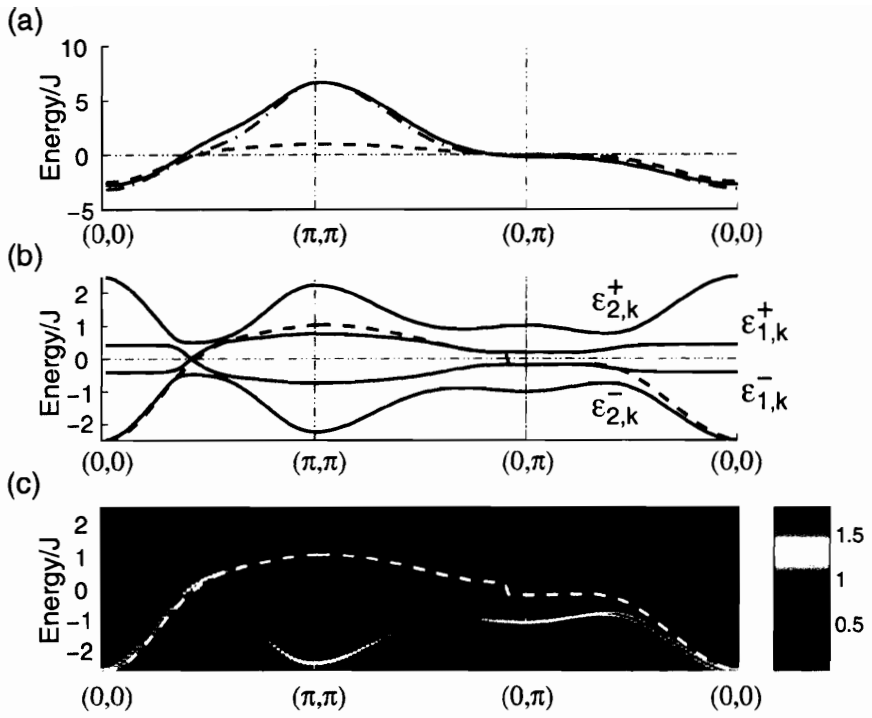

Figure 6-2: Energy dispersions along $(0,0) - (\pi,\pi) - (0,\pi) - (0,0)$. (a) Normal state dispersions using parameters from Ref. [175] (full line), Ref. [184] (dash-dot line) and $\epsilon^N_{\boldsymbol{k}}$ defined in main text (dashed line). (b) MF dispersions $\epsilon^{\pm}_{1,\boldsymbol{k}}$ and $\epsilon^{\pm}_{2,\boldsymbol{k}}$ for $x = 0.18$ and parameters used in Ref. [106]. (c) MF spectral function with Lorentzian broadening $\Gamma = J/5$ where $J = 150$meV. Dashed line in (b) and (c) plots $[(\epsilon^N_{\boldsymbol{k}})^2 + \Delta^2_{\boldsymbol{k}}]^{1/2} \times \mathrm{sgn}(\epsilon^N_{\boldsymbol{k}})$.

spin correlations. It is the pairing energy, and thus the spin correlations, that control both the gap at $\boldsymbol{k}_A$ and the energy $\epsilon^{\pm}_{1,\boldsymbol{k}}$ at $(0,\pi)$. Hence, this MF theory accounts for the strong renormalization of the electron dispersion in the antinodal region by the spin background. To compare the MF dispersion with the experimental fits to ARPES data we derive the underlying normal dispersion $\epsilon^N_{\boldsymbol{k}}$ such that $[(\epsilon^N_{\boldsymbol{k}})^2+\Delta^2_{\boldsymbol{k}}]^{1/2}$ equals $\epsilon^+_{1,\boldsymbol{k}}$ at $\boldsymbol{k}_A$, $(0,\pi)$ and at the nodal point, and $\epsilon^+_{2,\boldsymbol{k}}$ at $(0,0)$ [Figs. 6-2(b) and 6-2(c)]. In Fig. 6-2(a) we plot $\epsilon^N_{\boldsymbol{k}}$ for $x=0.18$ against the normal dispersion fits from Refs. [175, 184] along major symmetry directions. Clearly, below the Fermi level, $\epsilon^N_{\boldsymbol{k}}$ captures the experimental dispersive features, namely the energy scale of the nodal dispersion and the flatness around the antinodal points. ARPES does not probe the dispersion above the Fermi energy and both experimental fits use band calculation results to fix the energy at (π,π) [175], whence the mismatch between $\epsilon^N_{\boldsymbol{k}}$, obtained for the $tt't''J$ model, and these fits above the Fermi level. Interestingly, exact diagonalization calculations for the $tt't''J$ model indicate that the dispersion above the Fermi level is less dispersive than expected from the bare hopping parameters [48].

6.4 Tunneling spectra of strongly correlated d-wave SC

We now consider the tunneling conductance for the above MF theory of doped Mott insulators. The expressions for the spectral function (5.10) and (5.12) are used to obtain the dI/dV curves at $x=0.20$, $x=0.10$ and $x=0.05$ [Figs. 6-3(a)-(c)]. Fig. 6-3(d) further depicts these MF spectra with a frequency dependent broadening given by $\Sigma''(\omega)=-\omega^2/(0.75\text{eV})$ to better compare to experiments. Here we would like to point out that the MF theory produces a sharp electron spectral peak at the $\epsilon^{\pm}_{2,\boldsymbol{k}}$ band. However, we expect such a spectral peak is significantly broadened if one goes beyond the MF approximation. This is because $\epsilon^{\pm}_{2,\boldsymbol{k}}$ are high energy bands which have many decay channels. The introduced broadening $\Sigma''(\omega)=-\omega^2/(0.75\text{eV})$ captures such a effect to some degree[1].

The curves in Fig. 6-3 show the tunneling DOS for three of the four bands, namely $\epsilon^-_{2,\boldsymbol{k}}$, $\epsilon^-_{1,\boldsymbol{k}}$ and $\epsilon^+_{1,\boldsymbol{k}}$. The fourth $\epsilon^+_{2,\boldsymbol{k}}$ band has vanishing spectral weight and does not appear. The tunneling conductance plots are, therefore, highly asymmetric around zero bias. From Fig. 6-3(d) we see that the bias sign asymmetry is enhanced as hole density is reduced. This result, which is consistent with experiments [36, 159, 42, 160], is a hallmark of models with strong local Coulomb repulsion between electrons, which makes it easier to add a hole to the sample than to add an electron [206, 207, 174]. Note that the presence of two negative energy bands leads to a peak-dip-hump in the dI/dV curve as observed in various materials [36, 200, 202].

Figs. 6-3(a)-6-3(c) also depict the doping evolution of the minimum gap locus, which reproduces LSCO data [136]. Upon lowering hole doping from $x=0.20$ to $x=0.10$ the wave vector $\boldsymbol{k}_A$ moves away from $(0,\pi)$, however, unlike the cases depicted in Figs. 6-1(c) and 6-1(d), no extra peak develops next to the SC coherence peak. This

[1] A more extended discussion on the width of the high energy peaks is presented in Sec. 7.3.

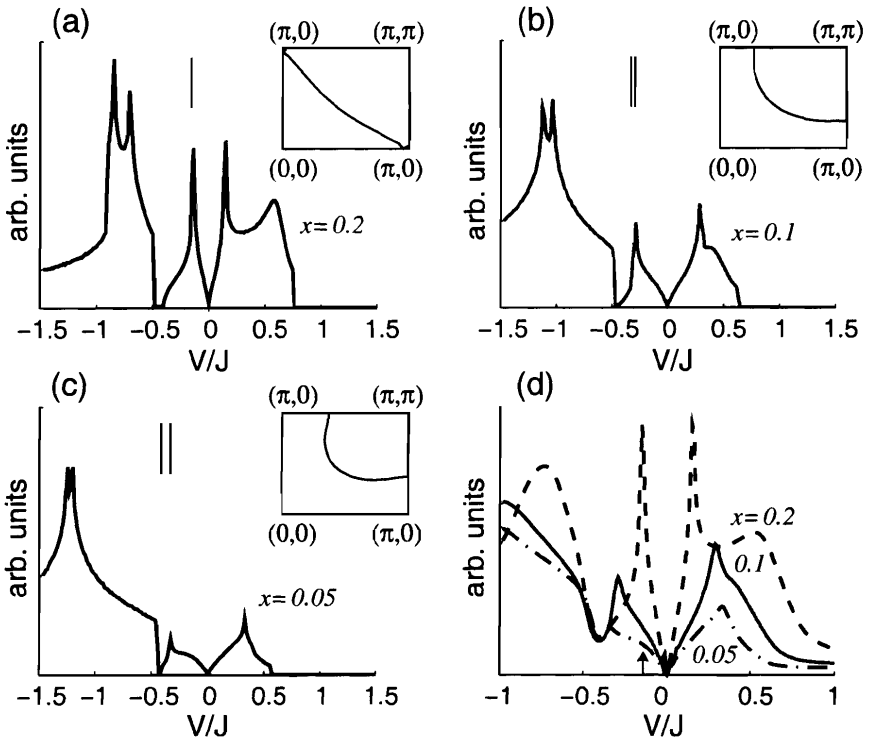

Figure 6-3: MF tunneling conductance for (a) $x = 0.20$, (b) $x = 0.10$ and (c) $x = 0.05$. (d) The same spectra with broadening given by $\Sigma''(\omega) = -\omega^2/(0.75\text{eV})$. Momentum space and energy resolution are the same as in Fig. 6-1. Inset of (a)-(c) plot minimal gap locus of $\epsilon^{\pm}_{1,\boldsymbol{k}}$. Vertical bars in (a)-(c) denote SC gap and VH singularity energies.

follows from the aforementioned flattening of the dispersion in the antinodal region, which keeps the difference between the SC gap and VH singularity energies small. This difference increases for $x = 0.05$, yet, instead of a double peak structure, we observe a strong suppression of the SC coherence peak in the tunneling spectrum of Fig 6-3(c) due to the disappearance of the electron spectral weight in the $\epsilon_{1,\boldsymbol{k}}$ band near the antinodal points. This behavior is in stark contrast with weak coupling BCS predictions.

The strong variation of spectral line shapes with doping depicted in Fig. 6-3(d) reproduces experimental evidence for different types of spectra in SC cuprate materials [36]. The $x = 0.20$ spectrum shows well defined SC coherence peaks mimicking weak coupling BCS d-wave superconductors. In the underdoped $x = 0.10$ and $x = 0.05$ spectra, the SC coherence peaks are pushed to higher energy reflecting the doping dependence of the SC gap, and lose spectral weight, in agreement with experiments [36, 159, 42, 160, 199]. Since the SC coherent peaks lose more spectral weight than states inside the gap, the tunneling curves display a negative curvature in the gap region and develop a "shoulder" in the spectral line shape [indicated by the arrow in Fig. 6-3(d)] as observed in experimental data [36, 159]. In addition, and despite the presence of long-range SC order, SC coherence peaks are hardly resolved in the $x = 0.05$ spectrum. Notably, similar spectra have been observed in deeply underdoped Bi2212 [36, 159] and NaCCOC. [42, 160]

The above properties of underdoped spectra can be rationalized in terms of the nodal-antinodal dichotomy supported by ARPES [31, 34, 112, 136, 23] without invoking coexisting ordered states [36] or phase separation scenarios [208]. This dichotomy is reflected in the depletion of spectral weight in the antinodal region, which is consistent with the destruction of SC coherence tunneling peaks. The spectral weight of nodal states is more resilient and contributes to the relative enhancement of the DOS at sub-gap energies, which develops the aforementioned "shoulder" in the spectral line shape.

6.5 Conclusions

In this chapter, we compute the tunneling differential conductance for the "doped carrier" MF theory of the $tt't''J$ model. Our results reproduce tunneling data from cuprates and provide a consistent theoretical description of both ARPES and tunneling experiments in these layered strongly correlated d-wave SC materials. Since these are single electron probes which resolve information in energy space, the above agreement supports that the "doped carrier" MF theory correctly captures the dynamics of holes in doped Mott insulators.

Chapter 7

Concluding remarks

Reasoning draws a conclusion, but does not make the conclusion certain, unless the mind discovers it by the path of experience.

Roger Bacon

The purpose of this chapter is to provide some concluding remarks to the thesis: we attempt to clarify the simple physical picture that stems from our results and we argue that many aspects of the phenomenology of underdoped cuprates can be understood in terms of the interplay between *local* spin correlations and the doped carrier dynamics. We first comment on the role short-range spin correlations play in determining the hole dynamics (Sec. 7.1) and on how these correlations are captured by the "doped carrier" multi-band description (Sec. 7.2). We then discuss some of the experimental evidence favoring the coexistence of short-range d-wave superconducting (dSC) and antiferromagnetic (AF) correlations (Sec. 7.3) and argue that the doping induced renormalization of t' and t'' follows from the growing relevance of dSC over AF correlations (Sec. 7.4). In Sec. 7.5 we clarify some similarities and differences between the "doped carrier" formulation of the $tt't''J$ model introduced in this thesis and the slave boson approach to the same model. Finally we draw some last comments in Sec. 7.6.

7.1 Role of short-range correlations

In this thesis we are interested in single electron properties of doped Mott insulators with particular emphasis on the superconducting state near the Mott insulator transition as observed in the high-T_c cuprate materials. In this context, angle-resolved photoemission spectroscopy (ARPES) is a most relevant experimental probe which inserts a hole in the system and resolves its dynamics as a function of momentum. Tunneling measurements also provide dynamical information, but without the momentum space resolution content of ARPES data. In the limit of conventional and uncorrelated metals quasiparticles are dressed electrons whose dispersive features are largely determined by an effective external potential landscape that does not depend on the exact position of all other electrons. In strongly correlated systems, however,

the dynamics of a hole is deeply intertwined with its surroundings. Given the large Coulomb gap, near half-filling the hole is encircled by localized spins, in which case the hole dynamics is closely related to nearby spin correlations.

To illustrate how short-range spin correlations affect the hole dynamics and the related hole spectral features we consider two opposite limits, namely that of staggered local moments and and that of resonating singlet bonds. As stated before in this thesis, staggered local moments strongly renormalize inter-sublattice hopping but do not frustrate intra-sublattice hopping. The simple minded argument is that when a vacancy moves to the nearest-neighbor (NN) site it leaves a local moment misplaced in the staggered spin arrangement. Consequently, the electron dispersion in an AF background is symmetric across the $(0,\pi) - (\pi,0)$ line. In addition, the dispersion along this line is controlled by t' and t'' as determined by the corresponding bare hopping processes [46, 48, 109, 110].

Interestingly, in the presence of resonating singlet bonds exactly the opposite *may* apply. These states can be thought of as a quantum superposition of dimer coverings of the lattice. In this case, the motion of a vacancy between two sites requires the rearrangement of the dimers and effectively connects different coverings. Depending on the actual coverings that constitute the spin state, as well as on the relative phases, the vacancy hopping between two sites can be either favored or frustrated. Therefore, the effective renormalization of t, t' and t'' depends on the nature of the underlying spin liquid correlations. As it turns out, for those spin liquid states believed to be of interest to the $tt't''J$ model the effective t' and t'' are strongly reduced down by a factor $\sim x$. This fact is easily appreciated in the slave boson formulation of doped spin liquids. In Expression (3.11) the hopping of spinons and holons is controlled by the fields U_{ij} and V_{ij} which, in the mean-field d-wave ansatz (3.9), vanish beyond NN. Even though, in general, intra-sublattice U_{ij} and V_{ij} can be non-zero, in Chapter 3 it is shown that in the parameter regime of interest to cuprates they are at most proportional to the doping level x. Therefore, coherent hole hopping between 2^{nd} and 3^{rd} NN is frustrated in the spin liquid background and t' and t'' are strongly renormalized. As it follows from (3.11), NN neighbor hopping processes are renormalized down to the spin energy scale J [108], which determines the bandwidth.

From the above we see that different spin correlations induce distinct electron dispersions. In addition, different spin correlations can also underlie different spectral intensities associated with the corresponding dispersions. Removing one electron introduces an additional spin-1/2 in the system which lies around the electrically charged vacancy site [Figs. 7-1(b) and 7-1(e)]. Once the system is allowed to evolve after the electron removal two distinct behaviors can be observed: (i) in the presence of staggered moments the extra spin-1/2 stays close to the vacancy [Fig. 7-1(c)] whereas (ii) the liquid nature of resonating valence bonds screens the doped spin away from the vacancy [Fig. 7-1(f)]. As a result, in the underdoped limit, the former state carries more spectral weight than the latter one.

Notably, the above discussion is closely connected to numerical work in the $tt't''J$ model. In fact, the results reported in Chapter 2 show that one hole states in the 2D $tt't''J$ model are the superposition of two states where: (i) the vacancy is surrounded by a staggered spin pattern and (ii) the vacancy is surrounded by a uniform spin

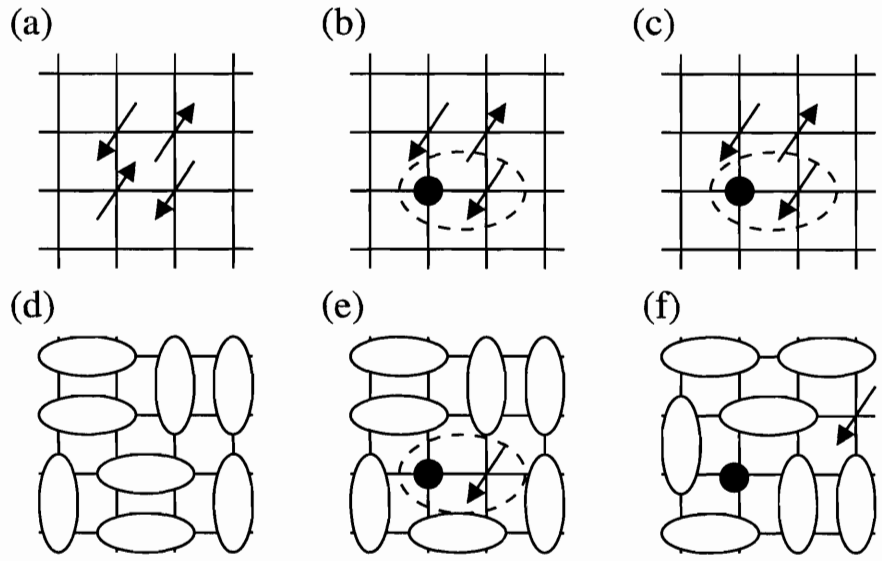

Figure 7-1: Schematic pictures for the introduction and evolution of a hole in two different spin backgrounds. In the case of staggered local moments (a) removing an electron with spin $S_z = +\frac{1}{2}$ leaves a vacancy and a nearby spin $S_z = -\frac{1}{2}$ which, together, carry the same quantum numbers as a hole (b). Due to the rigidity of the staggered moment spin configuration the vacancy and the extra $S_z = -\frac{1}{2}$ spin remain bound to each other. Removing an electron from a resonating singlet bond spin configuration (d) leaves the same local signature of a hole (e). However, the liquid nature of the spin background takes the extra spin $S_z = -\frac{1}{2}$ away from the vacancy (f).

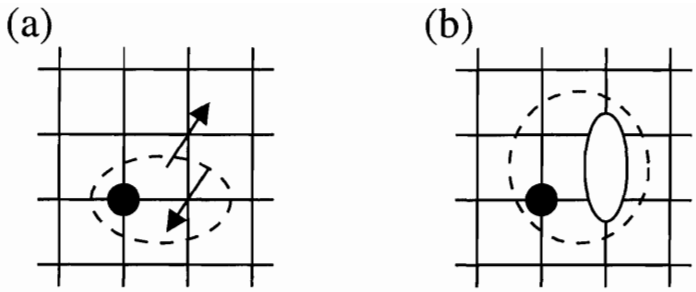

Figure 7-2: Schematic representation of the dopon (a) and the holon (b). The dopon is obtained by removing a lattice spin and corresponds to the vacancy plus the nearby spin introduced by doping. The holon is obtained when the spin in the dopon configuration (a) is absorbed by the spin background and, thus, is the composite object made of a vacancy and its encircling spin singlet configuration.

pattern that screens the hole spin-1/2 away. Numerics also shows that the former has large quasiparticle spectral weight and strongly renormalizes t while the latter has vanishing spectral intensity and strongly renormalizes t' and t''. Therefore, the numerical study suggests that both staggered moment and singlet bond states are relevant to the $tt't''J$ model. These states are also of relevance to the cuprate materials as they are naturally related to the neighboring AF and dSC phases in the underdoped sector of the cuprate phase diagram.

Since ARPES probes the dispersion renormalization and the distribution of spectral weight in energy-momentum space as a function of doping, it is a highly valuable source of information about the evolution of short-range correlations with varying electron density. Based on our mean-field results, below we argue that ARPES data suggests t, t' and t'' are renormalized in consonance with the presence of staggered AF correlations in the undoped compounds and with the growing relevance of singlet bond correlations as materials are doped away from half-filling.

7.2 Two-band description of local energetics

Quantum Monte Carlo simulations on the tJ and Hubbard models [209, 210, 211, 212] show that the electron spectral function has a four band structure. In Refs. [211, 212] the two bands below the Fermi level were interpreted in terms of two different states, namely: (i) holes on top of an otherwise unperturbed spin background and (ii) holes dressed by spin excitations. This interpretation is consistent with the aforementioned numerical work supporting a two-band interpretation of single hole states in the $tt't''J$ model (Chapter 2) and translates into the fact that there exist two relevant spin configurations around the vacancy.

In the "doped carrier" formalism of the $tt't''J$ model derived in Chapter 4 the vacancy can also be screened by two different spin structures. The one-dopon state is just the hole obtained by removing a lattice spin. Pictorially, the hole is the composite object made of a vacancy and a nearby spin [see Fig. 7-2(a)]. Close to half-filling

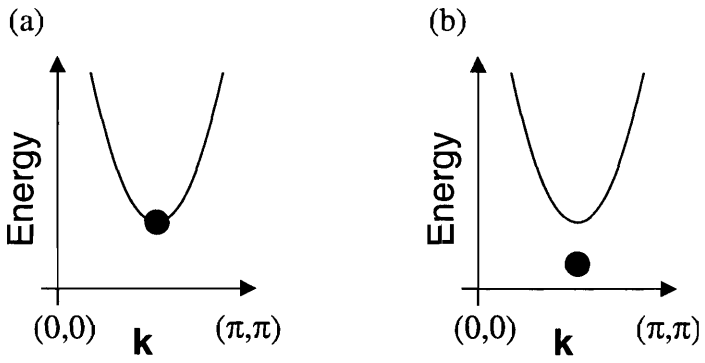

Figure 7-3: Schematic band diagram for a hole introduced into a spin system with AF spin correlations. If the hole does not change the background correlations it occupies the bottom of the coherent band (a). If, instead, the moving hole distorts the surrounding spin configuration and decreases its kinetic energy, it lies below the aforementioned dispersion (b).

local AF correlations are dominant and we take the one-dopon state to correspond to a vacancy encircled by staggered local moments. In addition, the dopon spin can be screened away by the spin background creating a holon, which is the non-local object corresponding to a spinon-dopon pair [Fig. 7-2(b)]. The mixing of spinons and dopons is described by the $\sim d^\dagger f f^\dagger d$ term in (4.13) which can be recast as $\sim b f^\dagger d$. This term drives the decay of the dopon into a spinless spinon-dopon pair and a chargeless spinon. Physically, this process means that the vacancy is encircled by a local spin singlet configuration while the doped carrier spin-1/2 is taken away by the spin background.

The $tt't''J$ model describes vacancies hopping in a spin background. In the low doping limit vacancies are dilute and we can focus on the local problem of a single vacancy surrounded by spins. The hole motion, which is determined by the hopping term, is frustrated by and frustrates the AF spin correlations driven by the Heisenberg term. Hence, in the underdoped regime, the $tt't''J$ model local physics is that of the competition between the hole kinetic energy and the spin exchange energy. The two-band description intrinsic to the "doped carrier" formulation of the $tt't''J$ model, which is intrinsically a one-band model, captures the above competition: (i) the one-*dopon* state preserves the local AF correlations favored by the exchange term but does not hop coherently between NN, thus frustrating the kinetic energy term; (ii) the one-*holon* state, which is the singlet pair of a dopon and a spinon, hops coherently between NN but distorts the spin background and frustrates the exchange energy. The evidence for coherent NN hopping following the spinon-dopon hybridization comes, for instance, from the nodal spectral function in Figs. 5-4(b) and 5-4(c) which shows a linear quasiparticle dispersion across the Fermi point near $(\frac{\pi}{2}, \frac{\pi}{2})$.

The above description provides a simple picture for the fact that, upon doping the insulator parent compound, the chemical potential does not fall on top of the valence band, thus preventing the formation of hole pockets with size x [23, 34, 112, 24]. If

short-range spin correlations are only of the staggered moment type the hole inserted in the system sits on the bottom of a band that disperses like a single hole in an AF background [Fig. 7-3(a)]. However, if the hole distorts the surrounding spins in a manner that decreases its kinetic energy it can appear below the AF band bottom, hence inside the gap [Fig. 7-3(b)]. Therefore, the absence of hole pockets in hole doped cuprates results from the change of spin correlations that enhances NN hopping. Note that the resulting kinetic energy gain stabilizes the formation of spinon-dopon pairs which lead to the dSC phase.

7.3 Interplay between dSC and AF correlations

We thus find that in the dSC phase AF correlations are relegated to high energy while, at low energy, d-wave singlet bond correlations underlie long-range dSC order. Even though at mean-field level the dopon dispersion is sharp, a vacancy surrounded by local Néel spins is not a true coherent state in the spin liquid background. Hence, a less approximate theoretical approach would yield a broadened dopon dispersion.

The claim that both AF and dSC correlations are important to determine the dynamics of holes and, consequently, to fit experiments, means that at least at short time scales both staggered moment and d-wave spin singlet spin configurations exist around the vacancy. In addition, if both short-range correlations leave fingerprints in the electron spectral function, then the above time scales are long enough to affect the vacancy dynamics. Since we find that at $T = 0$ the spinon-dopon mixing order parameter $b_0 \approx \sqrt{x}$, dopons spend most of the time paired to a spinon. The pairing between spinons and dopons is local and, therefore, the typical distance between these two entities can be denoted by na, where a is the lattice constant and n is a number of order unity. The relevance of AF correlations is tied to the time scale that measures how long the dopon and the spinon spend far apart, which is set by $\frac{na}{v_s} \sim \frac{\hbar}{\Gamma}$ where v_s is the characteristic spinon velocity and Γ is the dopon dispersion broadening energy scale. Given that the spinon bandwidth is set by J, we expect $\Gamma \sim J$, which is of the order of the dopon band width.

The above argument is consistent with the remarkably broad hump, with a width of order J, observed by ARPES in the cuprate materials [22, 23, 34, 24, 134, 135, 152, 185]. Previous work has identified the role of phonons and of self-trapping polaron effects in broadening the spectral feature that disperses as a hole in an AF background [213]. Here we propose that the resilience of the role played by local AF correlations in the dSC spin liquid state also implies a broad high energy hump.

Γ is related to the inverse of the distance over which staggered moments might appear as the spin configuration surrounding the vacancy. Despite the broad hump measured by experiments, it is relevant to consider the sharp dopon mean-field dispersion as long as the above distance is large enough to allow for the local physics encoded in our mean-field approximation. Ultimately, the relevance of the two-band approach must be decided upon comparison to experiments. Thus, below, we summarize the evidence for two different spectral dispersions in ARPES data. Then we comment on other non-trivial properties of the electron spectral function which can

be understood as the result of a dopon band at high energy.

ARPES experiments on the cuprates identify two different dispersions. At lower energy a dispersion linear across the Fermi level close to $(\frac{\pi}{2}, \frac{\pi}{2})$ has spectral intensity vanishing with underdoping. These two signatures, namely the linear dispersion and small spectral weight, are consistent with resonating singlet bond spin correlations around the vacancies as discussed in Sec. 7.1. The higher energy dispersion is reminiscent of a hole with strongly frustrated NN hopping and with 2^{nd} and 3^{rd} NN hopping consistent with band calculation expectations. Besides, it carries most of the electron spectral weight. These constitute strong evidence for vacancies surrounded by staggered spin configurations (Sec. 7.1). Even though the high energy dispersion inherited from the undoped limit gets broader and fainter upon doping [24], as expected given the doping induced frustration of AF correlations, there exists experimental support for the presence of two pseudogap energy scales at $(0, \pi)$ all the way into the overdoped regime [22]. Since the high energy pseudogap energy connects to the energy scale at $(0, \pi)$ in the undoped compounds [22, 53], experiments suggest that short-range AF and dSC correlations coexist throughout a vast range of the high-T_c phase diagram.

The "doped carrier" MF theory describes the above two dispersions in terms of dopons and dopons forming singlet pairs with spinons. As discussed in Chapter 5, the dopon dynamics affects spectral properties at low energy in consistency with experimental observations. Specifically, the impact of the dopon dispersion on the electron spectral function is two-fold: (i) it renormalizes different dispersive features, such as the d-wave gap along the minimum gap locus [169] and the nodal dispersion which displays a kink at the same energy as the dip of the peak-dip-hump structure [22, 31, 34, 133, 134, 135, 185]; (ii) it determines the transfer of spectral weight to low energy as well as its momentum space distribution, leading to the formation of low energy spectral intensity arcs around the nodal direction [23, 34, 112] and to the evolution of the peak intensity at $(0, \pi)$ that resembles experiments [177, 178].

The above deviations from plain BCS theory are more striking at low doping density, namely the kink is sharper [Figs. 5-4(b) and 5-4(c)] and the arc length shorter [Fig. 5-5(b)], as observed by experiments [23, 133]. This fact supports that the nodal peak-dip-hump structure, the nodal dispersion "kink" and the spectral weight arcs are fingerprints of AF correlations in the metallic state, which grow as doping is reduced. It also supports the physical relevance of the dopon to understand the hole dynamics in doped Mott insulators.

Further evidence favoring the relevance of a sharp dopon band at mean-field level comes from the comparison between the hole and electron doped regimes. In the "doped carrier" mean-field theory the only distinction between both cases comes from the different dopon dispersion. Specifically, in the hole doped case dopons are present in the nodal region whereas in the electron doped regime dopons appear around $(0, \pi)$ and $(\pi, 0)$. This difference leads to a distinct doping evolution of the spectral weight transfer to low energy: in the case of doped holes nodal arcs are formed [Figs. 5-6(d) - 5-6(f)] while for electron doped parameters low energy spectral weight appears both in the antinodal and nodal regions [Figs. 5-9(d) - 5-9(f)]. This distinction is consistent with experiments [23, 34, 39, 112, 143, 164, 165]. For a more extended discussion on

the differences between the hole and electron doped regimes see Sec. 5.4.4.

Finally, we remark that both AF and dSC correlations are intrinsic to the proximity to the Mott insulating state. As far as our mean-field theory and the comparison to ARPES data are concerned these are *local* correlations. The fact that either AF or dSC (or maybe both) correlations can acquire long-range order is not the cause, and does not invalidate, the local analysis of the competition between hole hopping and staggered local moments encoded in the mean-field theory.

An interesting insight from the "doped carrier" formulation of the $tt't''J$ model is that the physics of spin liquids and staggered spin correlations are not mutually exclusive in doped Mott insulators. Indeed, we find that local AF correlations may affect the phenomenology of doped spin liquid states in consistency with experiments.

7.4 Renormalization of t' and t''

In Sec. 4.3.2 we decouple the hopping term (4.9) to derive the quadratic mean-field Hamiltonian. Since some terms include six fermion operators we must consider the average of quartic fermionic operators. Specifically, in Expression (4.16) we assume that the spin configuration around the vacancy in the one-dopon state is of the Néel type. As a result, the mean-field dopon dispersion (4.17) only includes intra-sublattice hopping processes. The absence of NN neighbor coherent hopping captures the kinetic energy frustration due to AF correlations. As discussed in Sec. 7.2 dopons mix with spinons in order to overcome such a frustration.

The average taken in Equation (4.16) is not self-consistent and, as a result, does not capture the reduction of AF correlations with increasing temperature and doping. Consequently, the above mean-field calculation overestimates the kinetic energy gain due to spinon-dopon hybridization and, thus, the stability of spinon-dopon pairs as well. Neglecting the doping dependence of the spin average (4.16) the dopon band stays approximately at the same energy for different hole densities [Fig. 5-4(a) - 5-4(c)]. Following the discussion in Sec. 7.2, we find that accounting for the aforementioned doping dependence of the spin average (4.16) the energy difference between the chemical potential and the dopon band must decrease with the reduction of AF correlations and, therefore, with increasing doping. Such a pattern is observed in NaCCOC [24].

In the "doped carrier" mean-field theory spinon-dopon pairs are very stable and the mean-field pairing temperature increases very quickly with doping [Fig. 4-1(a)]. As discussed in Sec. 4.4 this mean-field transition temperature is much higher than the Kosterlitz-Thouless temperature for the loss of long-range phase coherence. The two transition temperatures define the Nernst region N in the hole doped phase diagram Fig. 4-1(b). This region is so large that it confines the pseudogap regime without short-range dSC fluctuations [denoted by PG Fig. 4-1(b)] to a tiny section of the phase diagram. However, if the reduction of local AF correlations with temperature is included in the spin average (4.16) the stability of spinon-dopon pairs is additionally reduced with increasing temperature and the mean-field transition temperature is lowered. Hence, we expect the Nernst region in the phase diagram to be smaller than

in Fig. 4-1(b), as it seems to be the case in experiments [117].

In the above we comment on the consequences of reducing the magnitude of $\langle \widetilde{\boldsymbol{S}}_i . \widetilde{\boldsymbol{S}}_j \rangle$ in $4\langle \widetilde{\boldsymbol{S}}_i . \widetilde{\boldsymbol{S}}_j \rangle = (-1)^{j_x+j_y-i_x-i_y}$ due to the decrease of local AF correlations. However, doping the Mott insulator state also develops different spin correlations, namely resonating singlet bond correlations, which strongly renormalize t' and t'' (Sec. 7.1). Hence, a self-consistent calculation of the spin average (4.16) should account for such a renormalization.

In Sec. 4.3.4 we elaborate at length on the renormalization of hopping parameters and, in particular, we mention that in order to fit the decrease of the high energy pseudogap scale with doping t' and t'' must reduce with growing doping density. Therefore, throughout the paper, we use doping dependent effective hopping parameters t_2 and t_3 [see Expressions (4.27) and (4.28)]. Interestingly, in Sec. 5.4.3 we find that the doping dependence of the high energy pseudogap scale underlies, for instance, the increase of the low energy spectral arcs' length with doping.

While the doping dependence in (4.27) and (4.28) is put by hand, with no particular argument favoring one functional dependence over another, here we point out that it captures the change of spin correlations that we miss once we take the spin average (4.16) without requiring self-consistency. More importantly, we provide a physical explanation for the reduction of the high energy pseudogap scale with doping. Specifically, we propose this doping dependence follows the growing importance of local d-wave singlet bond correlations over local staggered moment correlations as we move way from half-filling. In other words, we propose it is a consequence of the fact that the time scale over which staggered moment spin configurations surround the vacancies decreases with doping. To understand this fact recall that the high energy pseudogap appears in underdoped samples due to t' and t'' which are not frustrated by AF correlations. As discussed in Sec. 7.1, d-wave singlet correlations strongly renormalize t' and t'' and, therefore, the growth in importance of these correlations induces the decrease of the high energy pseudogap scale. We further remark that the experimentally observed lowering of this scale offers additional support for spin correlations that strongly renormalize t' and t'', as is the case with resonating singlet bonds.

7.5 Comparison to slave boson approach

In Sec. 4.3 we refer that the "doped carrier" mean-field phase diagram (Fig. 4-1) resembles that of slave boson mean-field theory. In this context, the similarity of both approaches follows from two facts: (i) use of fermionic representation of spins and (ii) analogy between the condensation of holons and of spinon-dopon pairs. However, there also exist differences between both approaches. For instance, in Sec. 5.3.2 we mention some drawbacks of slave boson mean-field theory which are overcome in the the "doped carrier" formalism (see Sec.5.4). Below we clarify the relation between the slave boson approximation and the approach hereby introduced.

In doped Mott insulators even the simplest hole-like object, namely a vacancy plus a neighboring spin, is not an on-site entity. The schematic representation of

such an object, which we name dopon, is depicted in Fig. 7-2(a). In the presence of certain spin correlations the hole spin and the vacancy drift apart. This process can be understood in the following terms: the spin neighboring the vacancy in the one-dopon state forms a singlet with the spin background which screens the extra spin-1/2 away. The resulting vacancy plus the encircling spin singlet configuration [Fig. 7-2(b)] can be thought of as the holon in the slave boson approach, as we further motivate below.

In the $tt't''J$ model formulation presented in Chapter 4 we treat the dopon as an on-site fermion and explain that forces us to enlarge the physical Hilbert space. We also introduce spinons which are electrically neutral spin-1/2 fermions that carry $SU(2)$ gauge charge related to the $\psi_i^\dagger \boldsymbol{\sigma} \psi_i = 0$ projection constraint. Within this formulation, the vacancy surrounded by a spin singlet configuration corresponds to the spinon-dopon singlet pair described by $\hat{B}_{ij}$ in (4.12), which is an electrically charged spinless operator that carries the above $SU(2)$ gauge charge. Hence, it has exactly the same quantum numbers as the holon operator h_i in the slave boson formalism.

The expectation values B_{ij} and $\langle h_i \rangle$ characterize the phases in the "doped carrier" and slave boson formulations of the $tt't''J$ model respectively. For instance, ansatz $\langle h_i^\dagger \rangle = [h_0 \ 0]$ for the holon condensate together with the d-wave ansatz (3.9) for spinons describes dSC or Fermi liquid states when $h_0 \neq 0$. Similarly, ansatz (4.20) for the spinon-dopon pairs B_{ij} describes the same phases in case the d-wave ansatz for spinons is taken. Interestingly, for a given spinon state, the physical symmetries of a phase described by a certain pattern of holon condensation $\langle h_i^\dagger \rangle = [\langle h_{i,1}^\dagger \rangle \langle h_{i,2}^\dagger \rangle]$ are the same as those of a state where spinon-dopon pairing yields

$$B_{ii} = \begin{bmatrix} \langle h_{i,2} \rangle & \langle h_{i,1} \rangle \\ \langle h_{i,1}^\dagger \rangle & -\langle h_{i,2}^\dagger \rangle \end{bmatrix} \tag{7.1}$$

Hence, not only do spinon-dopon pairs carry the same quantum numbers as holons, but also the pairing transition leads to the same phases as holon condensation.

An important difference between the slave boson holon operator h_i and the spinon-dopon pair operator $\hat{B}_{ij}$ is that the former acts on a single site whereas the latter can act on different sites i and j and, thus, is explicitly non-local. Following the on-site character of holons in the slave boson approach, the coherent contribution to the slave boson mean-field spectral function has uniform spectral weight throughout momentum space (see Sec. 5.3.2). In the "doped carrier" formalism, however, spinons and dopons do not mix uniformly in momentum space [Figs. 5-6(d) - 5-6(f)]. Hence, the resulting anisotropic distribution of low energy spectral weight reflects the internal structure of spinon-dopon pairs, which are non-local composite objects.

In Sec. 7.1 we point out that the dynamics of the vacancy depends on the surrounding spin correlations. Hence, any spectral dispersion is not just associated to the vacancy but to the vacancy and a certain encircling spin configuration. In this context, the physical picture of a holon is that of a vacancy and the surrounding spin singlet configuration [Fig. 7-2(b)] and, thus, it is also not a truly on-site entity. The "doped carrier" approach provides the formalism to capture the internal structure of holons, which are singlet pairs of spinons and dopons.

Close to the nodal points the above momentum space anisotropy is not relevant. Physically, that results from the fact that at large distances a local holon is a good approximation to a non-local spinon-dopon pair. In addition, at low energy the physics at long time scales is dominant. Following the discussion in Sec. 7.3, in this limit, spin correlations around the vacancy captured by the high energy $\epsilon^{-}_{2,\boldsymbol{k}}$ dispersion are associated to a short time scale and can be neglected. Therefore, the low energy effective theory in the "doped carrier" formulation of the doped Mott insulator dSC state is the same as the corresponding low energy effective theory in the slave boson formulation. Specifically, both describe nodal Bogoliubov quasiparticles whose spectral weight vanishes linearly in x as $x \rightarrow 0$.

At mean-field level, the slave boson approximation only considers vacancies surrounded by a spin singlet background. Hence, unlike the "doped carrier" approach, it only captures one type of screening of the vacancy by the encircling spins. For that reason, the coherent contribution to the mean-field spectral function in the dSC state only displays one dispersion, namely the d-wave nodal dispersion of spinons, whose spectral intensity vanishes with underdoping [32, 57, 58]. In that respect, the mean-field slave boson approach addresses the quasiparticle properties of the low energy dispersion identified by ARPES in the doped cuprate samples. Of course, if all fluctuations around the mean-field slave boson theory are properly considered, the physics of the $tt't''J$ model is captured at all energy scales. The problem of including the effect of fluctuations is already very complicated even at the level of the low energy effective theory, which describes strongly coupled fermionic, bosonic and gauge fields [32, 57, 58, 64]. Gauge fields mediate a strong attraction between ψ_1 and ψ_2 spinons, h_1 and h_2 holons and between spinons and holons. For a discussion on the consequent role of gauge fluctuations see Ref. [32]. Here we only mention that the attraction between spinons enhances AF correlations [63], while that between spinons and holons favors the increase of quasiparticle features, like the sharpening of the spectral line shape at low energy [65]. We expect the combination of these two effects on nodal quasiparticles to augment the quasiparticle spectral weight and the relevance of AF correlations around the vacancy, in accordance with the picture stemming from the "doped carrier" formulation.

The gauge field appears in the slave boson formulation as a way to implement the projection constraint, which is dealt with exactly in variational Monte Carlo calculations [77, 127, 170, 171, 214]. Refs. [170, 171] thoroughly compare this technique to slave boson mean-field results and, thus, offer insights on the role of gauge fluctuations, which are shown to strongly enhance nodal quasiparticle properties. The "doped carrier" formalism includes hole-like objects, the dopons, and accounts for the effect of the projection operators $\mathcal{P}$ in terms of the interaction between dopons and spins, which can be handled at mean-field level. Therefore, it is not surprising to find that "doped carrier" mean-field results are much closer to those of variational Monte Carlo calculations [Fig. 5-5(c)]. An additional remark is that projected BCS states are standardly used in the aforementioned variational approaches, while it would be interesting to understand what differences would come from using projected "doped carrier" mean-field states.

Experiments on hole doped materials show the emergence of the dSC nodal dis-

persion above the lower Hubbard band [24]. Similarly, data on electron compounds shows the buildup of spectral weight inside the Mott-Hubbard gap which eventually evolves into the dSC dispersion [39]. Then, cuprate phenomenology suggests that along with the lower and upper Hubbard bands, two dimensional doped Mott insulators develop spectral features in the mid-gap region. This is a non-trivial property to obtain at mean-field level. For instance, the Hartree-Fock approach to the one-band Hubbard model [215] only includes the lower and upper Hubbard bands. As mentioned before, at mean-field level, the slave boson approach describes instead the mid-gap dispersion that emerges upon doping. Interestingly, the "doped carrier" mean-field theory captures both the Hubbard and the mid-gap bands. As a consequence, it reproduces the spectral weight transfer features between both bands, such as the underlying momentum space anisotropy. As indicated in Sec. 5.3.2, the slave boson mean-field approach not only does not obtain the above anisotropy, but also misses the related enhancement of quasiparticle properties in the nodal region, as well as sum rules that determine the spectral weight transfer across the Fermi level. Both problems are overcome in the "doped carrier" mean-field approach, as discussed in Sec. 5.4.

7.6 Probing local correlations

In this thesis we propose a new mean-field theory of doped Mott insulators which, to some extent, consists of an effective two fluid model of vacancies that can be encircled either by a staggered moment or a singlet bond spin configuration. This theory thus embodies the compromise between spin exchange energy and charge kinetic energy and, in particular, borrows from Anderson's suggestion [26] that resonating singlet bonds enhance hole hopping without paying too big of an exchange energy price. The RVB picture is one of the candidate scenarios to describe the (ab)normal metallic state above T_c and, particularly so, to explain the reduction in the uniform spin susceptibility at temperatures far above the superconducting critical temperature [19]. More conventional theoretical routes are rather based on diagrammatic arguments. Due to the proximate Néel phase and the strong AF local correlations, one possible path is to explore the role of AF fluctuations [182]. Reconciling this approach with the Knight shift data has its own problems though [63]. The large body of evidence for strong deviations from Fermi liquid theory does not encourage a perturbative approach on top of the electron Fermi sea either. Bolder proposals suggest that the pseudogap represents a new ordered state (despite the absence of any experimental evidence toward the existence of the corresponding transition into that state) or at least a hidden ordered state proximate in parameter space. The attractiveness of an eventual new order also comes from what can be argued to be critical behavior at optimal doping. In this context, the RVB scenario and its formal realization as the slave boson approach are quite unique in that they capture both small-distance physics, as the spin-gap phenomenon, and long-distance power law behavior, the hallmark of criticality. This remarkable achievement is due to the presence of gauge fields, which are inescapable in any effort involving slave particles. Gauge fields

are, to the author's knowledge, the only way to formally capture a crucial aspect of the crossover between truly localized and truly itinerant electrons: in the former case the charge in the system is that of vacancies and equals x; in the latter the Fermi sea encloses a volume equal to $1-x$; the transition between the x and $1-x$ scalings is taken care by gauge fields which effectively transfer charge into the spin degrees of freedom [114]. The very existence of gauge fields, which mediate long-range interactions between charge and spin excitations, unveils how tricky the discussion of long-range properties (like "what phase are we in?") can get. It is also prone to misunderstandings and miscommunications, something that breeds in the high-T_c community (at least from the eyes of a newcomer). The discussion around spin-charge separation is the perfect example: where some people see spin and charge separating at short distances, other people perceive a salesman advertising spin and charge separate at large length scales. In many respects, the physics of the pseudogap regime is that of the coexistence, interplay and compromise between different short-range correlations due to strong interactions. That explains, for instance, the different crossovers observed in the rich and elusive phenomenology of cuprates. Therefore, even if the pseudogap metallic state is adiabatically connected to a Fermi liquid state, it might be more useful to start with some sort of spin and charge separated degrees of freedom when it comes down to make sense out of experiments which apparently lie outside the realm of Landau's theory. That is seemingly the case if one wants to reconcile the small spin density of states coexisting with strong short-ranged AF fluctuations [63].

The above said, the question "what are the local correlations that strive in the pseudogap regime?" still lacks an answer. Strongly correlated systems are renowned for the near degeneracy of different states and, indeed, some order other than superconductivity may drive the system into the normal state. Since lowering temperature brings up superconducting order, the hope to probe the quantum nature of whatever lies there beyond superconductivity is normally restricted to triggering a finite magnetic field and to looking at the core of magnetic vortices. In this thesis we advocate an alternative/complimentary line of attack. Specifically, we remark that signatures of short-ranged correlations in strongly correlated systems can be identified by experiments that probe the hole dynamics, like ARPES and tunneling. Then, if the pseudogap regime is related to the increasing importance of some competing correlations that differ from dSC correlations at short length scales, they should leave identifying traces in ARPES or tunneling experiments performed in the superconducting state. Interestingly, if we account for the role of local staggered moment correlations, which are generically expected close to the Mott transition, on top of the RVB state a large spectrum of non-trivial ARPES and tunneling experimental evidence concerning the superconducting state of cuprates finds theoretical explanation. These results strongly suggest that *if* there exists any order that enfeebles the dSC state in the deeply underdoped regime it must be related to superconductivity at small distances. One possible candidate, but not necessarily so, is the staggered-flux state [216].

Bibliography

[1] J.G. Bednorz and K.A. Müller, Z. Phys. B **64**, 188 (1986).

[2] H. Kamerlingh Onnes, *Comm. Phys. Lab. Univ. Leiden* Nos. 119, 120, 122 (1911).

[3] J. Bardeen, L.N. Cooper, and J.R. Schrieffer, Phys. Rev. **108**, 1175 (1957).

[4] J.R. Schrieffer. *Theory of Superconductivity* (Addison-Wesley, New York, 1964).

[5] C.E. Gough, M.S. Colclough, E.M. Forgan, R.G. Jordan, M. Keene, C.M. Muirhead, A.I.M. Rae, N. Thomas, J.S. Abell, and S. Sutton, Nature **326**, 855 (1987).

[6] P. Chaudhari, J. Mannhart, D. Dimos, C.C. Tsuei, J. Chi, M.M. Oprysko, and M. Scheuermann, Phys. Rev. Lett. **60**, 1653 (1988).

[7] J.C. Wynn, D.A. Bonn, B.W. Gardner, Y.-J. Lin, R. Liang, W.N. Hardy, J.R. Kirtley, and K.A. Moler, Phys. Rev. Lett. **87**, 197002 (2001).

[8] D.A. Bonn, J.C. Wynn, B.W. Gardner, Y.-J. Lin, R. Liang, W.N. Hardy, J.R. Kirtley, and K.A. Moler, Nature **414**, 887 (2001).

[9] A. Hosseini, R. Harris, S. Kamal, P. Dosanjh, J. Preston, R. Liang, W.N. Hardy, and D.A. Bonn, Phys. Rev. B **60**, 1349 (1999).

[10] Y. Zhang, N.P. Ong, P.W. Anderson, D.A. Bonn, R. Liang, and W.N. Hardy, Phys. Rev. Lett. **86**, 890 (2001).

[11] H. Matsui, T. Sato, T. Takahashi, S.-C. Wang, H.-B. Yang, H. Ding, T. Fujii, T. Watanabe, and A. Matsuda, Phys. Rev. Lett. **90**, 217002 (2003).

[12] M. Sutherland D.G. Hawthorn, R.W. Hill, F. Ronning, S. Wakimoto, H. Zhang, C. Proust, E. Boaknin, C. Lupien, L. Taillefer, R. Liang, D.A. Bonn, W.N. Hardy, R. Gagnon, N.E. Hussey, T. Kimura, M. Nohara, and H. Takagi, Phys. Rev. B **67**, 174520 (2003).

[13] C.C. Tsuei and J.R. Kirtley, Rev. Mod. Phys. **72**, 969 (2000).

[14] A.C. Durst and P.A. Lee, Phys. Rev. B **62**, 1270 (2000).

[15] J.E. Hoffman, K. McElroy, D.-H. Lee, K.M. Lang, H. Eisaki, S. Uchida, and J.C. Davis, Science **297**, 1148 (2002).

[16] A. Hosseini, D.M. Broun, D.E. Sheehy, T.P. Davis, M. Franz, W.N. Hardy, R. Liang, and D.A. Bonn, Phys. Rev. Lett. **93**, 107003 (2004).

[17] Y.J. Uemura, G.M. Luke, B.J. Sternlieb, J.H. Brewer, J.F. Carolan, W.N. Hardy, R. Kadono, J.R. Kempton, R.F. Kiefl, S.R. Kreitzman, P. Mulhern, T.M. Riseman, D.Ll. Williams, B.X. Yang, S. Uchida, H. Takagi, J. Gopalakrishnan, A.W. Sleight, M.A. Subramanian, C.L. Chien, M.Z. Cieplak, G. Xiao, V.Y. Lee, B.W. Statt, C.E. Stronach, W.J. Kossler, and X.H. Yu, Phys. Rev. Lett. **62**, 2317 (1989).

[18] B. Batlogg, H.Y. Hwang, H. Takagi, R.J. Cava, H.L. Kao, and J. Kwo, Physica C **235-240**, 130 (1994).

[19] N.J. Curro, T. Imai, C.P. Slichter, and B. Dabrowski, Phys. Rev. B **56**, 877 (1997).

[20] C.C. Homes, T. Timusk, R. Liang, D.A. Bonn, and W.N. Hardy, Phys. Rev. Lett. **71**, 1645 (1993).

[21] T.R. Chien, D.A. Brawner, Z.Z. Wang, and N.P. Ong, Phys. Rev. B **43**, 6242 (1991).

[22] A. Damascelli, Z.-X. Shen, and Z. Hussain, Rev. Mod. Phys. **75**, 473 (2003).

[23] T. Yoshida, X.J. Zhou, T. Sasagawa, W.L. Yang, P.V. Bogdanov, A. Lanzara, Z. Hussain, T. Mizokawa, A. Fujimori, H. Eisaki, Z.-X. Shen, T. Kakeshita, and S. Uchida, Phys. Rev. Lett. **91**, 027001 (2003).

[24] K.M. Shen, F. Ronning, D.H. Lu, W.S. Lee, N.J.C. Ingle, W. Meevasana, F. Baumberger, A. Damascelli, N.P. Armitage, L.L. Miller, Y. Kohsaka, M. Azuma, M. Takano, H. Takagi, and Z.-X. Shen, Phys. Rev. Lett. **93**, 267002 (2004).

[25] J. Orenstein, G.A. Thomas, A.J. Millis, S.L. Cooper, D.H. Rapkine, T. Timusk, L.F. Schneemeyer, and J.V. Waszczak, Phys. Rev. B **42**, 6342 (1990).

[26] P.W. Anderson, Science **235**, 1196 (1987).

[27] X.-G. Wen, Ann. Phys. **316**, 1 (2005).

[28] H. Kleinert and J. Zaanen, Phys. Lett. A **324**, 361 (2004).

[29] E. Manousakis, Rev. Mod. Phys. **63**, 1 (1991).

[30] E. Dagotto, Rev. Mod. Phys. **66**, 763 (1994).

[31] X.J. Zhou, T. Yoshida, D.-H. Lee, W.L. Yang, V. Brouet, F. Zhou, W.X. Ti, J.W. Xiong, Z.X. Zhao, T. Sasagawa, T. Kakeshita, H. Eisaki, S. Uchida, A. Fujimori, Z. Hussain, and Z.-X. Shen, Phys. Rev. Lett. **92**, 187001 (2004).

[32] P.A. Lee, N. Nagaosa, and X.-G. Wen, cond-mat/0410445 (2004).

[33] O. Parcollet, G. Biroli, and G. Kotliar, Phys. Rev. Lett. **92**, 226402 (2004).

[34] F. Ronning, T. Sasagawa, Y. Kohsaka, K.M. Shen, A. Damascelli, C. Kim, T. Yoshida, N.P. Armitage, D.H. Lu, D.L. Feng, L.L. Miller, H. Takagi, and Z.-X. Shen, Phys. Rev. B **67**, 165101 (2003).

[35] A. Kaminski H.M. Fretwell, M.R. Norman, M. Randeria, S. Rosenkranz, U. Chatterjee, J.C. Campuzano, J. Mesot, T. Sato, T. Takahashi, T. Terashima, M. Takano, K. Kadowaki, Z.Z. Li, and H. Raffy, Phys. Rev. B **71**, 014517 (2005).

[36] K. McElroy, D.-H. Lee, J.E. Hoffman, K.M. Lang, J. Lee, E.W. Hudson, H. Eisaki, S. Uchida, and J.C. Davis, Phys. Rev. Lett. **94**, 197005 (2005).

[37] D. van der Marel, Phys. Rev. B **60**, R765 (1999).

[38] S. Ono and Y. Ando, Phys. Rev. B **67**, 104512 (2003).

[39] N.P. Armitage, F. Ronning, D.H. Lu, C. Kim, A. Damascelli, K.M. Shen, D.L. Feng, H. Eisaki, Z.-X. Shen, P.K. Mang, N. Kaneko, M. Greven, Y. Onose, Y. Taguchi, and Y. Tokura, Phys. Rev. Lett. **88**, 257001 (2002).

[40] A. Koitzsch, G. Blumberg, A. Gozar, B.S. Dennis, P. Fournier, and R.L. Greene, Phys. Rev. B **67**, 184522 (2003).

[41] R.W. Hill, C. Proust, L. Taillefer, P. Fournier, and R.L. Greene, Nature **414**, 711 (2001).

[42] T. Hanaguri, C. Lupien, Y. Kohsaka, D.-H. Lee, M. Azuma, M. Takano, H. Takagi, and J.C. Davis, Nature **430**, 1001 (2004).

[43] L.B. Ioffe and A.J. Millis, Phys. Rev. B **58**, 11631 (1998).

[44] T. Tohyama, Y. Shibata, S. Maekawa, Z.-X. Shen, N. Nagaosa, and L.L. Miller, J. Phys. Soc. Jpn. **69**, 9 (2000).

[45] W.-C. Lee, T.K. Lee, C.-M. Ho, and P.W. Leung, Phys. Rev. Lett. **91**, 057001 (2003).

[46] T. Tohyama and S. Maekawa, Supercond. Sci. Technol. **13**, R17 (2000).

[47] G.B. Martins, R. Eder, and E. Dagotto, Phys. Rev. B **60**, R3716 (1999).

[48] T. Tohyama, Phys. Rev. B **70**, 174517 (2004).

[49] G. Martinez and P. Horsch, Phys. Rev. B **44**, 317 (1991).

[50] S. Schmitt-Rink, C.M. Varma, and A.E. Ruckenstein, Phys. Rev. Lett. **60**, 2793 (1988).

[51] A. Ramšak and P. Horsch, Phys. Rev. B **57**, 4308 (1998).

[52] R. Eder and Y. Ohta, Phys. Rev. B **51**, 6041 (1995).

[53] K. Tanaka, T. Yoshida, A. Fujimori, D.H. Lu, Z.-X. Shen, X.-J. Zhou, H. Eisaki, Z. Hussain, S. Uchida, Y. Aiura, K. Ono, T. Sugaya, T. Mizuno, and I. Terasaki, Phys. Rev. B **70**, 092503 (2004).

[54] G.Baskaran, Z. Zou, and P.W. Anderson, Solid State Commun. **63**, 973 (1987).

[55] G. Baskaran and P.W. Anderson, Phys. Rev. B **37**, 580 (1988).

[56] I. Affleck, Z. Zou, T. Hsu, and P.W. Anderson, Phys. Rev. B **38**, 745 (1988).

[57] X.-G. Wen and P.A. Lee, Phys. Rev. Lett. **76**, 503 (1996).

[58] P.A. Lee, N. Nagaosa, T.-K. Ng, and X.-G. Wen, Phys. Rev. B **57**, 6003 (1998).

[59] X.-G. Wen, Phys. Rev. B **65**, 165113 (2002).

[60] T. Tohyama and S. Maekawa, Phys. Rev. B **49**, 3596 (1994).

[61] C. Kim, P.J. White, Z.-X. Shen, T. Tohyama, Y. Shibata, S. Maekawa, B.O. Wells, Y.J. Kim, R.J. Birgeneau, and M.A. Kastner, Phys. Rev. Lett. **80**, 4245 (1998).

[62] P.W. Leung, cond-mat/0508035 (2005).

[63] W. Rantner and X.-G. Wen, Phys. Rev. B **66**, 144501 (2002).

[64] X.-G. Wen and P.A. Lee, Phys. Rev. Lett. **80**, 2193 (1998).

[65] W. Rantner and X.-G. Wen, cond-mat/0105540 (2001).

[66] T. Senthil and M.P.A. Fisher, Phys. Rev. B **62**, 7850 (2000).

[67] N. Read and S. Sachdev, Phys. Rev. Lett. **66**, 1773 (1991).

[68] X.-G. Wen, Phys. Rev. B **44**, 2664 (1991).

[69] T. Senthil and M.P.A. Fisher, Phys. Rev. B **64**, 214511 (2001).

[70] T. Senthil and M.P.A. Fisher, Phys. Rev. Lett. **86**, 292 (2001).

[71] S. Kleefisch, B. Welter, A. Marx, L. Alff, R. Gross, and M. Naito, Phys. Rev. B **63**, 100507 (2001).

[72] A.Biswas, P. Fournier, V.N. Smolyaninova, R.C. Budhani, J.S. Higgins, and R.L. Greene, Phys. Rev. B **64**, 104519 (2001).

[73] L. Alff, Y. Krockenberger, B. Welter, M. Schonecke, R. Gross, D. Manske, and M. Naito, Nature **422**, 698 (2003).

[74] A. Abrikosov, Physics **2**, 5 (1965).

[75] P.A. Lee and N. Nagaosa, Phys. Rev. B **46**, 5621 (1992).

[76] G. Kotliar and J. Liu, Phys. Rev. B **38**, 5142 (1998).

[77] C. Gros, Phys. Rev. B **38**, 931 (1988).

[78] N. Trivedi and D.M. Ceperley, Phys. Rev. B **40**, 2737 (1989).

[79] S.E. Barnes, J. Phys. F **6**, 1375 (1976).

[80] P. Coleman, Phys. Rev. B **29**, 3035 (1984).

[81] T.C. Ribeiro and X.-G. Wen, Phys. Rev. B **68**, 024501 (2003).

[82] D.A. Ivanov, P.A. Lee, and X.-G. Wen, Phys. Rev. Lett. **84**, 3958 (2000).

[83] D.A. Ivanov and T. Senthil, Phys. Rev. B **66**, 115111 (2002).

[84] A. Biswas, P. Fournier, M.M. Qazilbash, V.N. Smolyaninova, H. Balci, and R.L. Greene, Phys. Rev. Lett. **88**, 207004 (2002).

[85] J.A. Skinta, M.S. Kim, T.R. Lemberger, T. Greibe, and M. Naito, Phys. Rev. Lett. **88**, 207005 (2002).

[86] F.C. Zhang, C. Gros, T.M. Rice, and H. Shiba, Supercond. Sci. Technol. **1**, 36 (1988).

[87] W. Rantner and X.-G. Wen, Phys. Rev. Lett. **86**, 3871 (2001).

[88] M. Franz and Z. Tesanovic, Phys. Rev. Lett. **87**, 257003 (2001).

[89] T.C. Ribeiro and X.-G. Wen, *unpublished.*

[90] X.-G. Wen, F. Wilczek, and A. Zee, Phys. Rev. B **39**, 11413 (1989).

[91] P.W. Leung, Phys. Rev. B **62**, R6112 (2000).

[92] K. Tsutsui, D. Poilblanc, and S. Capponi, Phys. Rev. B **65**, 020406 (2002).

[93] S.R. White and D.J. Scalapino, Phys. Rev. B **60**, R753 (1999).

[94] G.B. Martins, J.C. Xavier, L. Arrachea, and E. Dagotto, Phys. Rev. B **64**, 180513(R) (2001).

[95] R.J. Gooding, K.J.E. Vos, and P.W. Leung, Phys. Rev. B **49**, 4119 (1994).

[96] K. Tsutsui, T. Tohyama, and S. Maekawa, Phys. Rev. Lett. **83**, 3705 (1999).

[97] R.J. Gooding, K.J.E. Vos, and P.W. Leung, Phys. Rev. B **50**, 12866 (1994).

[98] Y. Onose, Y. Taguchi, K. Ishizaka, and Y. Tokura, Phys. Rev. Lett. **87**, 217001 (2001).

[99] N.P. Armitage, D.H. Lu, C. Kim, A. Damascelli, K.M. Shen, F. Ronning, D.L. Feng, P. Bogdanov, Z.-X. Shen, Y. Onose, Y. Taguchi, Y. Tokura, P.K. Mang, N. Kaneko, and M. Greven, Phys. Rev. Lett. **87**, 147003 (2001).

[100] P.A. Lee, Phys. Rev. Lett. **63**, 680 (1989).

[101] M.A. Kastner, R.J. Birgeneau, G. Shirane, and Y. Endoh, Rev. Mod. Phys. **70**, 897 (1998).

[102] T.C. Ribeiro, cond-mat/0409002 (2004).

[103] T.C. Ribeiro and X.-G. Wen, *in preparation.*

[104] M.C. Gutzwiller, Phys. Rev. Lett. **10**, 159 (1963).

[105] P.W. Anderson, P.A. Lee, M. Randeria, T.M. Rice, N. Trivedi, and F. C. Zhang, J. Phys. Condens. Matter **16**, R755 (2004).

[106] T.C. Ribeiro and X.-G. Wen, Phys. Rev. Lett. **95**, 057001 (2005).

[107] N.W. Ashcroft and N.D. Mermin. *Solid State Physics* (Saunders College Publishing, 1976).

[108] C.L. Kane, P.A. Lee, and N. Read, Phys. Rev. B **39**, 6880 (1989).

[109] T. Xiang and J.M. Wheatley, Phys. Rev. B **54**, R12653 (1996).

[110] V.I. Belinicher, A.L. Chernyshev, and V.A. Shubin, Phys. Rev. B **54**, 14914 (1996).

[111] E. Pavarini, I. Dasgupta, T. Saha-Dasgupta, O. Jepsen, and O.K. Andersen, Phys. Rev. Lett. **87**, 047003 (2001).

[112] Y. Kohsaka, T. Sasagawa, F. Ronning, T. Yoshida, C. Kim, T. Hanaguri, M. Azuma, M. Takano, Z.-X. Shen, and H. Takagi, J. Phys. Soc. Jpn. **72**, 1018 (2003).

[113] B.O. Wells, Z.-X. Shen, A. Matsuura, D.M. King, M.A. Kastner, M. Greven, and R.J. Birgeneau, Phys. Rev. Lett. **74**, 964 (1995).

[114] L.B. Ioffe and A.I. Larkin, Phys. Rev. B **39**, 8988 (1989).

[115] P. Olsson, Phys. Rev. B **52**, 4526 (1995).

[116] Z.A. Xu, N.P. Ong, Y. Wang, T. Kakeshita, and S. Uchida, Nature **406**, 486 (2000).

[117] N.P. Ong, Y. Wang, S. Ono, Y. Ando, and S. Uchida, Annalen der Physik **13**, 9 (2004).

[118] I. Ussishkin, S.L. Sondhi, and D.A. Huse, Phys. Rev. Lett. **89**, 287001 (2002).

[119] I. Ussishkin and S.L. Sondhi, Int. J. Mod. Phys. B **18**, 3315 (2004).

[120] Y. Wang, L. Li, M.J. Naughton, G.D. Gu, S. Uchida, and N. P. Ong, cond-mat/0503190 (2005).

[121] H. Takagi, T. Ido, S. Ishibashi, M. Uota, S. Uchida, and Y. Tokura, Phys. Rev. B **40**, 2254 (1989).

[122] G.M. Luke, L.P. Le, B.J. Sternlieb, Y.J. Uemura, J.H. Brewer, R. Kadono, R.F. Kiefl, S.R. Kreitzman, T.M. Riseman, C.E. Stronach, M.R. Davis, S. Uchida, H. Takagi, Y. Tokura, Y. Hidaka, T. Murakami, J. Gopalakrishnan, A.W. Sleight, M.A. Subramanian, E.A. Early, J.T. Markert, M.B. Maple, and C.L. Seaman, Phys. Rev. B **42**, 7981 (1990).

[123] M. Fujita, T. Kubo, S. Kuroshima, T. Uefuji, K. Kawashima, K. Yamada, I. Watanabe, and K. Nagamine, Phys. Rev. B **67**, 014514 (2003).

[124] J. Brinckmann and P.A. Lee, Phys. Rev. B **65**, 014502 (2002).

[125] A.W. Sandvik, Phys. Rev. B **56**, 11678 (1997).

[126] H. Balci, C.P. Hill, M.M. Qazilbash, and R.L. Greene, Phys. Rev. B **68**, 054520 (2003).

[127] C.T. Shih, T.K. Lee, R. Eder, C.-Y. Mou, and Y.C. Chen, Phys. Rev. Lett. **92**, 227002 (2004).

[128] P.K. Mang, O.P. Vajk, A. Arvanitaki, J.W. Lynn, and M. Greven, Phys. Rev. Lett. **93**, 027002 (2004).

[129] H. Takagi, S. Uchida, and Y. Tokura, Phys. Rev. Lett. **62**, 1197 (1989).

[130] G. Riou, P. Richard, S. Jandl, M. Poirier, P. Fournier, V. Nekvasil, S.N. Barilo, and L.A. Kurnevich, Phys. Rev. B **69**, 024511 (2004).

[131] P. Richard, G. Riou, I. Hetel, S. Jandl, M. Poirier, and P. Fournier, Phys. Rev. B **70**, 064513 (2004).

[132] T. Timusk and B. Statt, Rep. Prog. Phys. **62**, 61 (1999).

[133] A. Lanzara, P.V. Bogdanov, X.J. Zhou, S.A. Kellar, D.L. Feng, E.D. Lu, T. Yoshida, H. Eisaki, A. Fujimori, K. Kishio, J.-I. Shimoyama, T. Noda, S. Uchida, Z. Hussain, and Z.-X. Shen, Nature **412**, 510 (2001).

[134] A. Lanzara, P.V. Bogdanov, X.J. Zhou, N. Kaneko, H. Eisaki, M. Greven, Z. Hussain, and Z.-X. Shen, cond-mat/0412178 (2004).

[135] A. Kaminski, M. Randeria, J.C. Campuzano, M.R. Norman, H. Fretwell, J. Mesot, T. Sato, T. Takahashi, and K. Kadowaki, Phys. Rev. Lett. **86**, 1070 (2001).

[136] A. Ino, C. Kim, M. Nakamura, T. Yoshida, T. Mizokawa, A. Fujimori, Z.-X. Shen, T. Kakeshita, H. Eisaki, and S. Uchida, Phys. Rev. B **65**, 094504 (2002).

[137] D.M. King, Z.-X. Shen, D.S. Dessau, D.S. Marshall, C.H. Park, W.E. Spicer, J.L. Peng, Z.Y. Li, and R.L. Greene, Phys. Rev. Lett. **73**, 3298 (1994).

[138] L. Krusin-Elbaum, T. Shibauchi, and C.H. Mielke, Phys. Rev. Lett. **92**, 097005 (2004).

[139] L. Krusin-Elbaum, G. Blatter, and T. Shibauchi, Phys. Rev. B **69**, 220506(R) (2004).

[140] Z.-X. Shen, D.S. Dessau, B.O. Wells, D.M. King, W.E. Spicer, A.J. Arko, D. Marshall, L.W. Lombardo, A. Kapitulnik, P. Dickinson, S. Doniach, J. DiCarlo, T. Loeser, and C.H. Park, Phys. Rev. Lett. **70**, 1553 (1993).

[141] A. Ino, C. Kim, M. Nakamura, T. Yoshida, T. Mizokawa, Z.-X. Shen, A. Fujimori, T. Kakeshita, H. Eisaki, and S. Uchida, Phys. Rev. B **62**, 4137 (2000).

[142] F. Ronning, C. Kim, D.L. Feng, D.S. Marshall, A.G. Loeser, L.L. Miller, J.N. Eckstein, I. Bozovic, and Z.-X. Shen, Science **282**, 2067 (1998).

[143] H.S. Jin, D.H. Lu, N.P. Armitage, W.H. Choi, B.J. Kim, S.-J. Oh, S.H. Moon, H. Eisaki, and C. Kim, J. Phys. Chem. Solids **65**, 1403 (2004).

[144] V.J. Emery, Phys. Rev. Lett. **58**, 3759 (1987).

[145] C.M. Varma, S. Schmitt-Rink, and E. Abrahams, Solid State Commun. **62**, 681 (1987).

[146] F.C. Zhang and T.M. Rice, Phys. Rev. B **37**, 3759 (1988).

[147] N.B. Brookes, G. Ghiringhelli, O. Tjernberg, L.H. Tjeng, T. Mizokawa, T.W. Li, and A.A. Menovsky, Phys. Rev. Lett. **87**, 237003 (2001).

[148] G. Ghiringhelli, N.B. Brookes, L.H. Tjeng, T. Mizokawa, O. Tjernberg, P.G. Steeneken, and A. A. Menovsky, Physica B **312-313**, 34 (2002).

[149] M.S. Hybertsen, E.B. Stechel, M. Schluter, and D.R. Jennison, Phys. Rev. B **41**, 11068 (1990).

[150] P.E. Sulewski, P.A. Fleury, K.B. Lyons, S.-W. Cheong, and Z. Fisk, Phys. Rev. B **41**, 225 (1990).

[151] R. Coldea, S.M. Hayden, G. Aeppli, T.G. Perring, C.D. Frost, T.E. Mason, S.-W. Cheong, and Z. Fisk, Phys. Rev. Lett. **86**, 5377 (2001).

[152] J.C. Campuzano, H. Ding, M.R. Norman, H.M. Fretwell, M. Randeria, A. Kaminski, J. Mesot, T. Takeuchi, T. Sato, T. Yokoya, T. Takahashi, T. Mochiku, K. Kadowaki, P. Guptasarma, D.G. Hinks, Z. Konstantinovic, Z.Z. Li, and H. Raffy, Phys. Rev. Lett. **83**, 3709 (1999).

[153] D.S. Marshall, D.S. Dessau, A.G. Loeser, C-H. Park, A.Y. Matsuura, J.N. Eckstein, I. Bozovic, P. Fournier, A. Kapitulnik, W.E. Spicer, and Z.-X. Shen, Phys. Rev. Lett. **76**, 4841 (1996).

[154] P.J. White, Z.-X. Shen, C. Kim, J.M. Harris, A.G. Loeser, P. Fournier, and A. Kapitulnik, Phys. Rev. B **54**, R15669 (1996).

[155] A. G. Loeser, Z.-X. Shen, D.S. Dessau, D.S. Marshall, C.H. Park, P. Fournier, and A. Kapitulnik, Science **273**, 325 (1996).

[156] H. Ding, T. Yokoya, J. C. Campuzano, T. Takahashi, M. Randeria, M. R. Norman, T. Mochiku, K. Kadowaki, and J. Giapintzakis, Nature **382**, 51 (1996).

[157] M. Randeria and J.C. Campuzano, cond-mat/9709107 (1997).

[158] M. Eschrig and M.R. Norman, Phys. Rev. Lett. **85**, 3261 (2000).

[159] H. Pan, J.P. O'Neal, R.L. Badzey, C. Chamon, H. Ding, J.R. Engelbrecht, Z. Wang, H. Eisaki, S. Uchida, A.K. Gupta, K.-W. Ng, E.W. Hudson, K.M. Lang, and J.C. Davis, Nature **413**, 282 (2001).

[160] Y. Kohsaka, K. Iwaya, S. Satow, T. Hanaguri, M. Azuma, M. Takano, and H. Takagi, Phys. Rev. Lett. **93**, 097004 (2004).

[161] Y. Gallais, A. Sacuto, T.P. Devereaux, and D. Colson, Phys. Rev. B **71**, 012506 (2005).

[162] N. Gedik, J. Orenstein, R. Liang, D.A. Bonn, and W.N. Hardy, Science **300**, 1410 (2003).

[163] C. Panagopoulos, T. Xiang, W. Anukool, J.R. Cooper, Y.S. Wang, and C.W. Chu, Phys. Rev. B **67**, 220502(R) (2003).

[164] T. Claesson, M. Månsson, C. Dallera, F. Venturini, C. De Nadaï, N.B. Brookes, and O. Tjernberg, Phys. Rev. Lett. **93**, 136402 (2004).

[165] H. Matsui, K. Terashima, T. Sato, T. Takahashi, S.-C. Wang, H.-B. Yang, H. Ding, T. Uefuji, and K. Yamada, Phys. Rev. Lett. **94**, 047005 (2005).

[166] H. Matsui, K. Terashima, T. Sato, T. Takahashi, M. Fujita, and K. Yamada, Phys. Rev. Lett. **95**, 017003 (2005).

[167] T. Tohyama and S. Maekawa, Phys. Rev. B **64**, 212505 (2001).

[168] G. Blumberg, A. Koitzsch, A. Gozar, B.S. Dennis, C.A. Kendziora, P. Fournier, and R. L. Greene, Phys. Rev. Lett. **88**, 107002 (2002).

[169] J. Mesot, M.R. Norman, H. Ding, M. Randeria, J.C. Campuzano, A. Paramekanti, H.M. Fretwell, A. Kaminski, T. Takeuchi, T. Yokoya, T. Sato, T. Takahashi, T. Mochiku, and K. Kadowaki, Phys. Rev. Lett. **83**, 840 (1999).

[170] A. Paramekanti, M. Randeria, and N. Trivedi, Phys. Rev. B **70**, 054504 (2004).

[171] C.P. Nave, D. Ivanov, and P.A. Lee, *unpublished.*

[172] L.B. Ioffe and A.J. Millis, J. Phys. Chem. Solids **63**, 2259 (2002).

[173] D.E. Sheehy, T.P. Davis, and M. Franz, Phys. Rev. B **70**, 054510 (2004).

[174] M. Randeria, R. Sensarma, N. Trivedi, and F.-C. Zhang, cond-mat/0412096 (2004).

[175] M.R. Norman, M. Randeria, H. Ding, and J.C. Campuzano, Phys. Rev. B **52**, 615 (1995).

[176] H. Ding, M.R. Norman, T. Yokoya, T. Takeuchi, M. Randeria, J.C. Campuzano, T. Takahashi, T. Mochiku, and K. Kadowaki, Phys. Rev. Lett. **78**, 2628 (1997).

[177] R.H. He, D.L. Feng, H. Eisaki, J.-I. Shimoyama, K. Kishio, and G.D. Gu, Phys. Rev. B **69**, 220502(R) (2004).

[178] D.L. Feng, D.H. Lu, K.M. Shen, C. Kim, H. Eisaki, A. Damascelli, R. Yoshizaki, J.-I. Shimoyama, K. Kishio, G.D. Gu, S. Oh, A. Andrus, J. O'Donnell, J.N. Eckstein, and Z.-X. Shen, Science **289**, 277 (2000).

[179] H. Ding, J.R. Engelbrecht, Z. Wang, J.C. Campuzano, S.-C. Wang, H.-B. Yang, R. Rogan, T. Takahashi, K. Kadowaki, and D.G. Hinks, Phys. Rev. Lett. **87**, 227001 (2001).

[180] A. Carrington, A.P. Mackenzie, C.T. Lin, and J.R. Cooper, Phys. Rev. Lett. **69**, 2855 (1992).

[181] P.C. Pattnaik, C.L. Kane, D.M. Newns, and C.C. Tsuei, Phys. Rev. B **45**, 5714 (1992).

[182] P. Monthoux and D. Pines, Phys. Rev. B **49**, 4261 (1994).

[183] R. Hlubina and T.M. Rice, Phys. Rev. B **51**, 9253 (1995).

[184] M.R. Norman, Phys. Rev. B **61**, 14751 (2000).

[185] M.R. Norman, H. Ding, J.C. Campuzano, T. Takeuchi, M. Randeria, T. Yokoya, T. Takahashi, T. Mochiku, and K. Kadowaki, Phys. Rev. Lett. **79**, 3506 (1997).

[186] A. Fujimori, A. Ino, T. Mizokawa, C. Kim, Z.-X. Shen, T. Sasagawa, T. Kimura, K. Kishio, M. Takaba, K. Tamasaku, H. Eisaki, and S. Uchidau, J. Phys. Chem. Solids **59**, 1892 (1998).

[187] T. Kondo, T. Takeuchi, T. Yokoya, S. Tsuda, S. Shin, and U. Mizutani, J. Electron Spectr. Relat. Phenom. **137-140**, 663 (2004).

[188] P.V. Bogdanov, A. Lanzara, X.J. Zhou, S.A. Kellar, D.L. Feng, E.D. Lu, H. Eisaki, J.-I. Shimoyama, K. Kishio, Z. Hussain, and Z.-X. Shen, Phys. Rev. B **64**, 180505(R) (2001).

[189] A. Kaminski, S. Rosenkranz, H.M. Fretwell, M.R. Norman, M. Randeria, J.C. Campuzano, J.-M. Park, Z.Z. Li, and H. Raffy, cond-mat/0507106 (2005).

[190] H.C. Fu, J.C. Davis, and D.-H. Lee, cond-mat/0403001 (2004).

[191] T. Matsuzaki, N. Momono, M. Oda, and M. Ido, J. Phys. Soc. Jpn. **73**, 2232 (2004).

[192] D. Sénéchal and A.M.S. Tremblay, Phys. Rev. Lett. **92**, 126401 (2004).

[193] D. Sénéchal, P.L. Lavertu, M.A. Marois, and A.M.S. Tremblay, cond-mat/0410162 (2004).

[194] C. Dahnken, M. Potthoff, E. Arrigoni, and W. Hanke, cond-mat/0504618 (2005).

[195] T. Watanabe, T. Miyata, H. Yokoyama, Y. Tanaka, and J.-I. Inoue, J. Phys. Soc. Jpn. **74**, 1942 (2005).

[196] T.C. Ribeiro and X.-G. Wen, *unpublished.*

[197] W.-M. Que and G. Kirczenow, Phys. Rev. B **38**, 4601 (1988).

[198] A.J. Fedro and D.D. Koelling, Phys. Rev. B **47**, 14342 (1993).

[199] M. Oda, K. Hoya, R. Kubota, C. Manabe, N. Momono, T. Nakano, and M. Ido, Physica C **281**, 135 (1997).

[200] M. Oda, N. Momono, and M. Ido, Supercond. Sci. Technol. **13**, R139 (2000).

[201] M. Kugler, Ø. Fischer, Ch. Renner, S. Ono, and Y. Ando, Phys. Rev. Lett. **86**, 4911 (2001).

[202] M. Iavarone, M. Salluzzo, R. Di Capua, M.G. Maglione, R. Vaglio, G. Karapetrov, W.K. Kwok, and G.W. Crabtree, Phys. Rev. B **65**, 214506 (2002).

[203] D.J. BenDaniel and C.B. Duke, Phys. Rev. **160**, 679 (1967).

[204] J.Y.T. Wei, C.C. Tsuei, P.J.M. van Bentum, Q. Xiong, C.W. Chu, and M.K. Wu, Phys. Rev. B **57**, 3650 (1998).

[205] G.D. Mahan. *Many-Particle Physics* (Plenum, New York, 1990).

[206] W. Rantner and X.-G. Wen, Phys. Rev. Lett. **85**, 3692 (2000).

[207] P.W. Anderson and N.P. Ong, cond-mat/0405518 (2004).

[208] C. Howald, P. Fournier, and A. Kapitulnik, Phys. Rev. B **64**, 100504 (2001).

[209] A. Moreo, S. Haas, A.W. Sandvik, and E. Dagotto, Phys. Rev. B **51**, 12045 (1995).

[210] R. Preuss, W. Hanke, and W. von der Linden, Phys. Rev. Lett. **75**, 1344 (1995).

[211] A. Dorneich, M.G. Zacher, C. Gröber, and R. Eder, Phys. Rev. B **61**, 12816 (2000).

[212] C. Gröber, R. Eder, and W. Hanke, Phys. Rev. B **62**, 4336 (2000).

[213] A.S. Mishchenko and N. Nagaosa, Phys. Rev. Lett. **93**, 036402 (2004).

[214] S. Sorella, G.B. Martins, F. Becca, C. Gazza, L. Capriotti, A. Parola, and E. Dagotto, Phys. Rev. Lett. **88**, 117002 (2002).

[215] T. Moriya. *Spin Fluctuations in Electron Magnetism* (Springer, Berlin, 1985).

[216] P.A. Lee and X.-G. Wen, Phys. Rev. B **63**, 224517 (2001).